

# **A Study of Multipacting in Rectangular Waveguide Geometries**

*A thesis submitted to Lancaster University for the degree of Doctor of Philosophy  
in the Faculty of Applied Sciences*

***Philippe Goudket***



*Microwave Engineering Group, Lancaster University*

*ASTeC, CCLRC Daresbury Laboratory*

*Work supported by the Diamond Light Source Ltd.*

*21/9/2004*



## ***Declaration***

I declare that no portion of the work referred to in this thesis has been submitted to any other university or institute of learning in support of an application for another degree or qualification. The work, apart from collaborative efforts that have been clearly identified, is my own.

Philippe Gouket

## **Abstract**

Electron multipacting is a resonant process by which electrons build-up under the influence of a radio-frequency (RF) field. This process can occur in evacuated RF equipment such as the input coupler of accelerator cavities.

The superconducting RF cavities designed by Cornell University, that are used in a number of synchrotron light sources including the DIAMOND Light Source, have had a history of vacuum breakdown in the CESR ring at Cornell with frequencies that would be inappropriate for a reliable synchrotron facility. This work aims to understand and correct the problem and ensure smooth operation of the cavities.

The cause of the vacuum breakdown hindering the cavities' operation at Cornell was identified as being multipactor in the rectangular input coupler waveguide. Prior studies carried out by R.L. Geng at Cornell University identified a number of solutions which he proposed to verify experimentally. Two series of experiments were carried out at Cornell University on short waveguide sections.

The first session allowed us to observe, measure and attempt to suppress multipactor using techniques such as a longitudinal static magnetic bias field and a groove cut along the waveguide centreline. While the first technique was found to be quite effective, since a relatively weak 10G field was found to be sufficient to achieve complete multipactor suppression, the groove did not allow such total suppression of the multipactor though it did mitigate its effects.

The second experimental session was designed to complement the first. The waveguide allowed the testing of other methods such as multiple grooves, a ridge in place of the groove, or surface coatings. The ridge proved to be as effective as a groove with regards to multipactor suppression, while multiple grooves proved to increase rather than reduce the total multipacting current. The waveguide could also be heated or cooled to study the effect of baking the surface as well as that of condensed gases. Surface coatings were tested and found to have the expected effect of lowering the multipactor current, but the surface areas covered as well as the vacuum quality achieved were insufficient to conclusively validate the use of coatings as a means of achieving multipactor-free operation of the coupler.

Both series of experiments provided extensive measurements of electron currents at various locations on the waveguide and at a range of RF power levels; these were compared to simulations of multipactor developed using the MAGIC PIC code. The code results and the simulations were found to agree closely when using a secondary electron model including backscattered low energy electrons. The code was able to predict the effectiveness of a ridge, as well as agreeing with experimental observations. Instead of sharply defined multipactor bands as predicted by simple multipactor models, the multipactor current (above a certain power level) does not disappear completely even though it may show peaks and troughs for various values of the RF power.

In conclusion, the magnetic bias is the only proven method to ensure multipactor-free operation of the CESR-type cavities. A ridge or a groove cut along the centreline of the waveguide could be a simple, passive way of limiting and retarding the effects of multipactor in the input coupler, while coatings should certainly be considered, though more research is needed to fully validate the concept.

1	Introduction.....	1
1.1	Brief introduction to particle accelerator technology.....	1
1.2	Requirements for DIAMOND.....	3
1.3	The CESR superconducting RF cavities.....	4
1.3.1	Introduction to RF cavities.....	4
1.3.2	Description of the CESR cavity and waveguide.....	7
1.3.3	Description of the breakdown observed in the CESR cavities.....	8
1.4	Research objectives.....	10
2	Multipactor.....	11
2.1	Brief history of multipactor.....	11
2.2	Introduction to multipactor.....	12
2.3	Secondary electron emission.....	12
2.3.1	General properties.....	12
2.3.2	Reducing the secondary electron yield.....	19
2.4	Mechanism of multipactor.....	20
2.5	Methods of multipactor suppression.....	22
2.5.1	Suppression of multipactor through geometrical changes.....	22
2.5.2	Suppression of multipactor by preventing electron multiplication.....	24
3	Multipactor simulations.....	27
3.1	Methods of simulation.....	27
3.2	Analytical description.....	27
3.3	Numerical methods.....	28
3.4	Multipactor code development.....	29
3.5	The MAGIC code.....	30
3.5.1	Simulation of a rectangular waveguide geometry.....	31
3.5.2	Simulation of a coaxial waveguide.....	38
3.5.3	Results from the MAGIC code.....	40
4	Experimental method.....	42
4.1	Experiment description.....	42
4.1.1	RF waveguides.....	42
4.1.2	Grooved waveguide (Waveguide 2).....	44
4.1.3	Waveguide 3.....	45
4.2	Processing area set-up.....	55
4.3	Diagnostics.....	58
5	Experimental observations of multipactor.....	66
5.1	Experiment set-up and issues.....	66

5.1.1	Introduction .....	66
5.1.2	Waveguide 1 and 2 .....	66
5.1.3	Waveguide 3 .....	70
5.1.4	Accuracy of the measurements .....	71
5.2	General observations .....	71
5.2.1	Starting conditions of multipactor .....	71
5.2.2	Identification of multipactor .....	77
5.2.3	Location of electron multipactor .....	77
5.2.4	Surface conditioning .....	79
5.2.5	Multipacting electron energies .....	82
5.3	Comparison with simulations .....	89
5.3.1	Multipactor bands .....	89
5.3.2	Location of electron multipactor .....	91
6	Multipactor suppression .....	95
6.1	Modifications to the electron trajectories .....	95
6.1.1	Static longitudinal magnetic fields .....	95
6.1.2	Grooves .....	103
6.2	Modifications to the electron yield .....	115
6.2.1	Coatings .....	115
6.2.2	Conditioning .....	123
7	Multipactor in other components .....	125
7.1	Waveguide E-plane bend .....	125
7.2	Other components .....	127
7.2.1	Input coupler .....	127
7.2.2	RF Window .....	128
7.3	Conclusion .....	128
8	Conclusion .....	129
8.1	Multipactor simulations .....	129
8.2	Multipactor suppression methods .....	129
8.3	Further experiments and developments .....	131
	Appendix .....	133

## ***Acknowledgements***

I would like to express my heartfelt thanks to everyone who contributed, provided help or support during the course of this work. In no particular order, they are:

- The people at Cornell University, Ithaca, NY. Peter Quigley, Phil Barnes, Rick Roy for their help in setting up the experiments. Yulin Li for his help in building and coating a sample plate with a TiZrV getter layer. I would particularly like to thank John Reilly for his help in setting up and conducting the experiments, as well as helping me during my stay in Ithaca. I would also like to thank members of the Superconducting RF Group from the Laboratory for Nuclear Studies. Sergey Belomestnykh for his welcome and for making the WG3 series of experiments possible. Valery Shemelin for his help and explanations concerning analytical descriptions of multipacting. Hasan Padamsee for his welcome, enthusiasm and for communicating to me the drive to seek more answers. I would most particularly like to thank Rongli Geng for welcoming me into his field of study, for helping me to understand multipactor. I am grateful for his invitation to participate in the first series of experiments and for his help in designing the second. Thanks, Rongli, for your continued support.
- Jean-Michel Laurent, from the CERN Vacuum Group, for his help and for sharing the results of his research on a multipacting experiment.
- Jerzy Lorkiewicz, from DESY, for volunteering to apply a titanium nitride coating on a sample plate.
- Lars Ludeking from MRC for his help in using MAGIC to a fuller potential.
- The Diamond Light Source Company, for funding this research. Morten Jensen from E2V Technologies, latterly of the Diamond Light Souce Company, for his help in learning about MAFIA and for his help with the coupler geometry. I would also like to thank E2V Tecnologies for the help and interesting discussions they encouraged.
- Michael Pekeler and the ACCEL Corporation, for their help in providing information on the CESR cavity and coupler. I would also like to thank Michael for allowing me to participate in window testing at Cornell, which taught me much about the basics of practical SRF.

I would like to thank Oleg Malyshev from the ASTeC Vacuum Group at Daresbury Laboratory for his help in understanding vacuum-related problems and low energy electron/surface behaviour. I would also like to express my gratitude to the people at Daresbury Laboratory who helped turn my scribbles on a notepad into the WG3 experiment. I would like to thank the workshop for their excellent work on the waveguide construction. I would like to acknowledge the efforts of the Vacuum Support Group for their help in cleaning and leak-checking the waveguide. I would like to thank Ian Burrows and John Flaherty for the engineering design of the waveguide, turning my rather sketchy ideas into a practical experiment. Bob Bate, who helped me throughout the design period and directed me towards the people who could get things done. Emma Wooldridge for giving me a few tips on using Microwave Studio. Hywel Owen, for proof-reading the numerous drafts repeatedly. I would finally like to thank Mike Dykes, who provided valuable support, guidance and made this project work. Thanks, Mike.

I would like to thank Amos Dexter from Lancaster University for his help and enthusiasm in understanding the analytical and numerical descriptions of multipactor. I would like to thank Rebecca Seviour for her collaboration and for sharing the results of her research on multipactor. Finally, I would like to express my most heartfelt gratitude to Richard Carter, who throughout the project, provided insight, support and guidance. Thanks, Richard for making this research possible.

### ***List of abbreviations***

AU	Arbitrary Units
EEA	Electron Energy Analyser
MP	Multipactor
NC	Normal conducting
NEG	Non-Evaporable Getter
PMT	Photo-multiplier Tube
RF	Radio Frequency
SC	Superconducting
SEY	Secondary Electron Yield
SW	Standing Wave (mode)
TW	Travelling Wave (mode)
WG1/2	Waveguides 1 (standard) and 2 (slotted)
WG3	Waveguide 3

# 1 Introduction

## 1.1 *Brief introduction to particle accelerator technology*

Particle accelerators have been used for high-energy physics research since the early 1930s and also more recently for the production of synchrotron light. Modern particle accelerators use radio-frequency (RF) cavities to provide energy to the particle beam, which is guided through the machine (which may be a ring or a linear machine) to the interaction region (if the machine is a particle collider) or through bending magnets and insertion devices (if the machine is a light source). Particles in accelerators must travel in vacuum to avoid collisions with gas particles. Modern accelerators require vacuum pressures below  $10^{-7}$ mbar to  $10^{-11}$ mbar for highly sensitive machines that require high beam quality.

Particle colliders collide particles such as leptons or hadrons, as well as higher mass ions. A particular type of collider of interest to us is the B-factory, which is essentially a high-brightness lepton collider providing many collisions at centre-of-mass energies of 9-12GeV. This leads to the production (among other things) of b quarks that are of interest to high energy particle physicists. An example of a B-factory is CESR-B, for which the CESR cavities were designed (described in more detail in section 1.3.2).

Light sources take advantage of the electromagnetic radiation emitted by charged particles when they are accelerated [1]. This emission, called synchrotron light, was first observed accidentally in 1947 in the General Electric 70MeV Synchrotron. Modern light sources use insertion devices such as wigglers and undulators to subject the electron beam to transverse magnetic fields that lead to the emission of large amounts of light that can then be used in other fields of science.

RF cavities can be used to accelerate charged particles by applying an electric field in the direction of travel. Early accelerators used static electric fields but generating static potentials in excess of several tens of mega-volts becomes very challenging and expensive due to potential DC discharges. In order to avoid these problems, Ising suggested in 1924 to use alternating RF fields to accelerate particles. By having the particles pass through the field at a phase at which it would impart energy onto the particles, and shielding the particles from the field at times when the phase of the RF

field would instead reduce their energies, there is no theoretical limit to the energy levels particles can gain (practical considerations such as the maximum length as a linear accelerator or the maximum radius of a circular accelerator however impose restrictions). Having an alternating field however imposes that the particle beam cannot be continuous but separated into bunches that can pass through the accelerating structures at the right phases for acceleration.

RF, or radio-frequency, is a term used in the accelerator community to refer to electromagnetic waves of frequencies between approximately tens of MHz to tens of GHz. High power RF (or powers greater than tens of kilowatts) is generally generated by vacuum tubes such as klystrons or IOTs (Inductive Output Tubes). These tubes act as amplifiers of a low power signal (provided by a solid state device) by modulating electron beams and extracting their energy to produce RF. It can then be channelled to its intended use (generally a RF cavity) through waveguides (which are sections of conducting material used to guide and contain the electromagnetic wave with minimal losses. One of the most commonly used types of waveguide is rectangular waveguide, with a ratio of 2:1 in width:height. For a 500MHz RF wave one can use a WR1800 waveguide, that has an 18" by 9" cross-section. The mode used to propagate the wave down the waveguide is then the  $TE_{10}$  mode (shown in Figure 1).

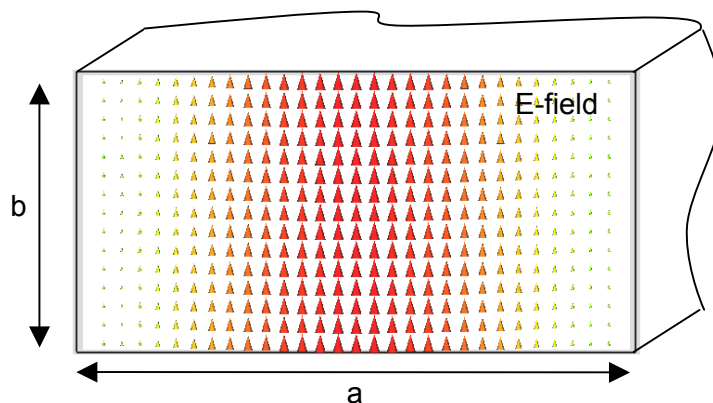


*Figure 1: View of a rectangular waveguide showing the electric field direction and strength of the  $TE_{10}$  mode through a transverse cross-section*

Modern accelerators use RF cavities to provide acceleration to the particles. Cavities are described in more detail in Section 1.3.1.

## **1.2 Requirements for DIAMOND**

The new UK synchrotron light source DIAMOND will be fitted with three superconducting cavities, which will be of the same type as those used at Cornell University. These cavities will also be used in the Canadian Light Source (CLS) and the Synchrotron Radiation Research Facility (SRRC) in Taiwan. As light sources require much greater mean time between beam failure than the collider applications the cavities were designed for, the target will be to ensure that the cavities do not impede continuous running (at most one RF trip per month). As the Cornell cavities were responsible, in 2002, for a trip every two days on average, there clearly was much scope for improvement.

Cornell University, in Ithaca, NY, operates CESR (Cornell Electron-positron Storage Ring). It is a 6GeV electron positron collider facility with parasitic synchrotron radiation beam lines (CHESS - Cornell High Energy Synchrotron Source). The ring was commissioned in 1979 with normal conducting accelerating cavities, which have since been replaced by 4 superconducting cavities. These cavities operate at a frequency of 500MHz, and are designed to handle power levels of up to 500kW each. In practice, however, these cavities have been hindered by vacuum bursts in the waveguide of the input coupler, particularly at higher operating power levels [2]. Studies and simulations carried out at Cornell laid the blame on multipacting, which was thought to occur in the cavity input coupler waveguide.

## 1.3 The CESR superconducting RF cavities

### 1.3.1 Introduction to RF cavities

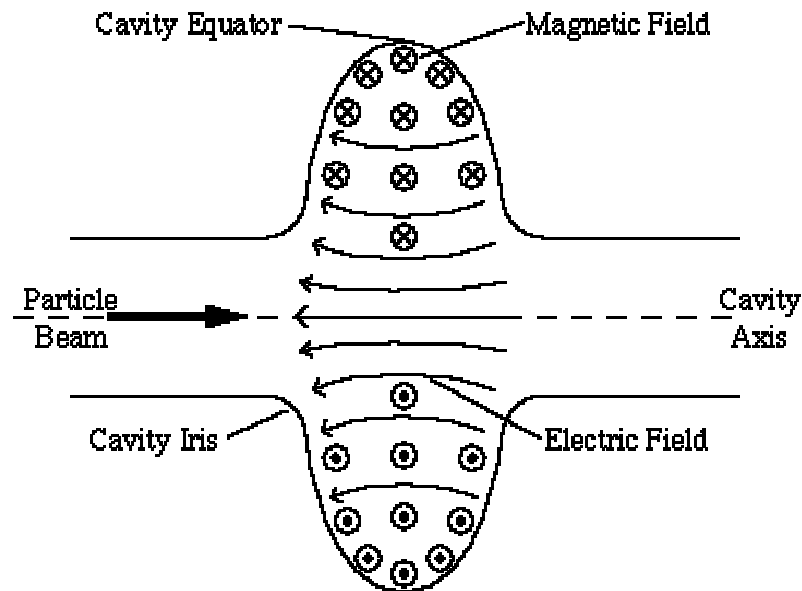


Figure 2: General layout of an RF cavity (from [3])

The properties of cavity resonators in particle accelerator applications are well described in reference books such as 'RF Superconductivity in Accelerators' [3].

Cavities are used to accelerate the charged particles of which the beam is comprised by hosting resonating radio-frequency (RF) fields. Cavities used in accelerator applications are designed to be used at a single RF frequency, and to host minimal higher order modes. High-order modes are modes at higher frequencies than the cavity's fundamental frequency, that can also resonate within the cavity.

The cavity is powered by a RF source, most commonly a klystron for high power RF. The RF is brought from the klystron to the cavity through waveguides, which are typically rectangular or coaxial. The RF is then fed to the cavity through a coupler, which may be of several possible designs. A cavity can quickly be characterised by its quality factor  $Q_0$ , which is linked to the rate of power loss or dissipation in the cavity;

$$Q_0 = \frac{\nu_0 U}{P_c} = \frac{G}{R_s}$$

where  $U$  is the energy stored in the cavity,  $\nu_0$  the cavity resonant frequency,  $P_c$  the dissipated power,  $G (= \frac{R_a}{Q_0})$ , often referred to as 'R/Q') the size- and material-independent geometry factor and  $R_s$  the surface resistance. Another important characteristic of a cavity is the shunt impedance  $R_a$ :

$$R_a = \frac{V_c^2}{P_c}$$

where  $V_c$  is the accelerating voltage and  $P_c$  is the power dissipated into the cavity walls.  $R_a$  is frequency dependent and should be as high as possible for an efficient transfer of power into the cavity in the cavity's fundamental operating mode. Shunt impedance can be linked to the efficiency of power transfer from the klystron to the cavity [3]. Geometrical considerations make cavities with small beam tubes and re-entrant geometries (as for the first cavity depicted in Figure 3) more efficient, but also allow such cavities to trap undesirable high-order modes (parasitic modes of higher frequency than the fundamental), which may resonate with the beam and cause instabilities. Thus, a high  $Q_0$  is greatly desirable to allow for less optimal geometries and still have excellent cavity performance. High quality factors (in the order of  $10^9 - 10^{11}$ ) are achievable by using superconducting (SC) technology, where ohmic losses are reduced to a fraction of the losses of a copper cavity (typical quality factors for normal conducting cavities are in the order of  $10^4 - 10^5$ ). Even though a superconductor's RF resistivity is not zero as is its DC resistivity, it remains much lower than that of a normal conducting (NC) material.

The gain due to reduced resistivity is however to be balanced with the need for a cryogenic system, but despite the low Carnot efficiency (fundamental thermodynamic limit of a refrigerator system, equal to 0.014 for refrigeration from room temperature to 4.2K), coupled to the low refrigerator efficiency ( $\sim 0.2$ ) of such a system, a superconducting cavity still is, for an application like a high current light source, more power efficient than a normal conducting cavity (by a factor of 200 approximately) [3].

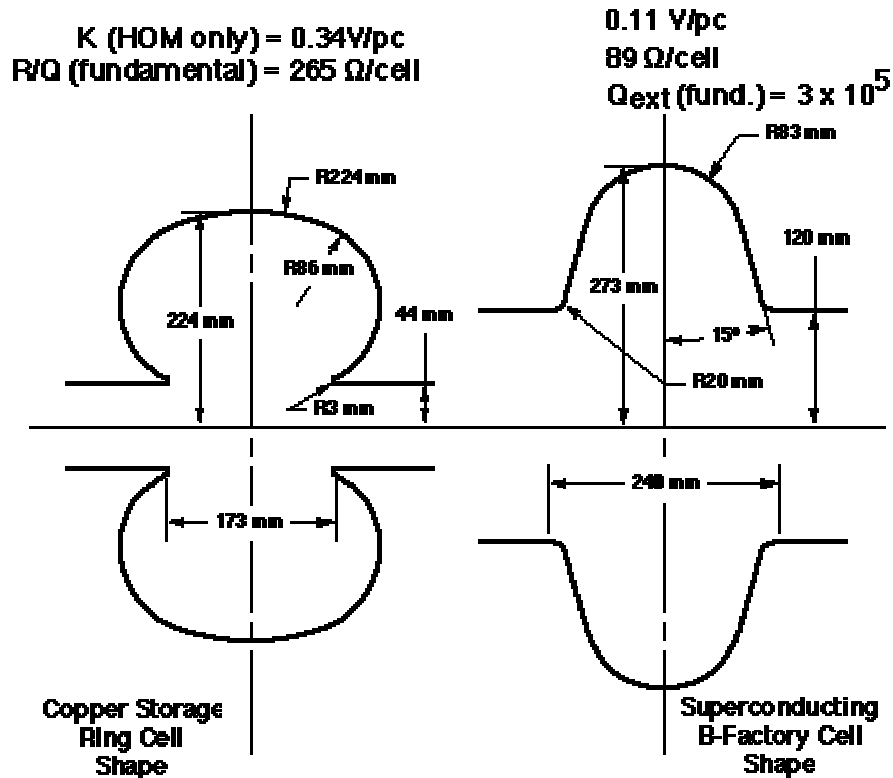


Figure 3: Comparison of typical re-entrant, normal conducting and elliptical, superconducting cavity layouts for high current applications (from [3])

An advantage of a high quality factor  $Q_0$  is that the cavity geometry does not need to be optimal to achieve good performances, therefore the cavity can avoid narrow beam tubes and re-entrant nose cones that increase the geometry factor but also both trap higher order modes in the cavity (decreasing beam quality) and enhance field emission of electrons off the surfaces (due to sharp edges creating higher local electric fields) (see Figure 3 for an illustration).

In an effort to reduce energy consumption and have a beam quality that is not impaired by trapped higher order modes, the Cornell cavities are designed with a fluted beam-tube to further improve the higher order mode extraction [3 (section 16.5)]. These modes can then be dissipated by ferrite tiles placed at either end of the cavity beam tubes.

After a review of the various systems developed worldwide, the cavities of the type used and designed at Cornell University and manufactured by ACCEL were chosen for the DIAMOND project. These cavities are used in the CESR electron-positron collider ring, which also has a synchrotron radiation facility (CHESS). The cavities have also been chosen by other planned light sources such as SRRC (Taiwan) and the CLS (Saskatchewan).

### 1.3.2 Description of the CESR cavity and waveguide

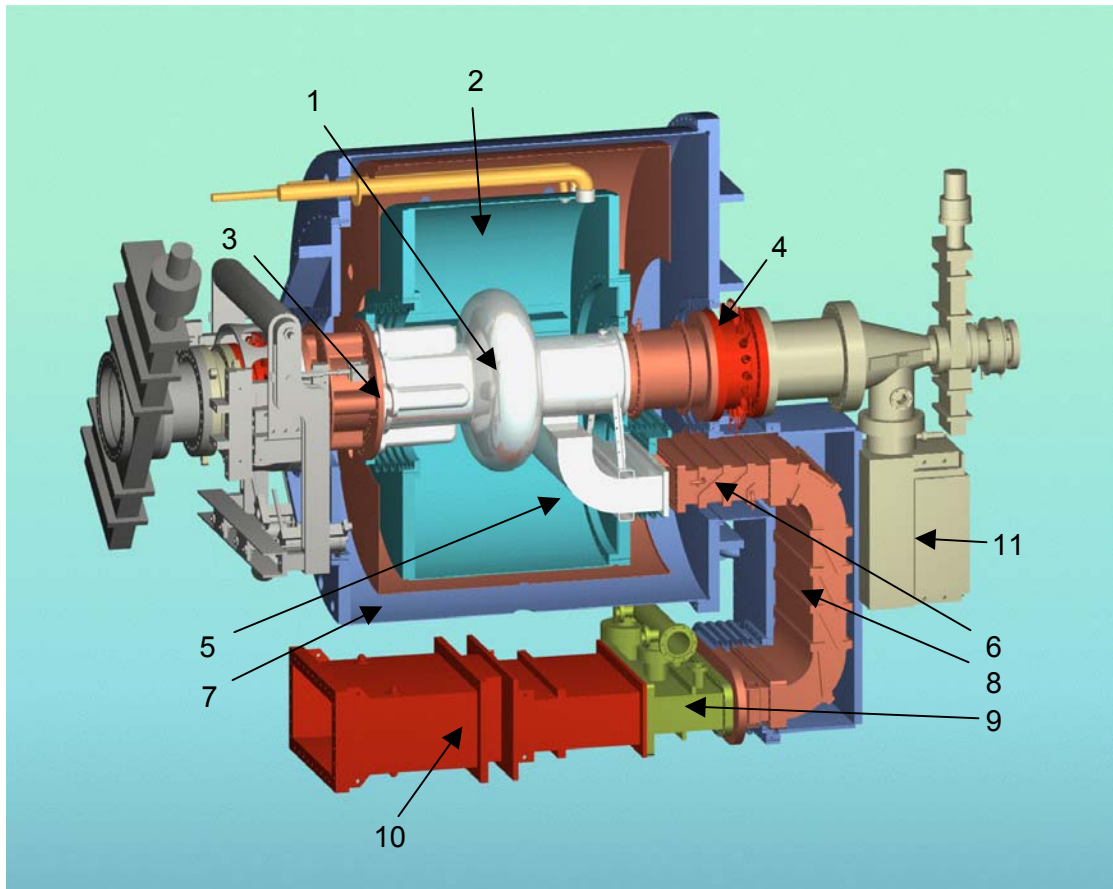


Figure 4: Schematic of the CESR cryomodule

The cavity (1), as shown in Figure 4, has an elliptical cross-section along the r-z plane, mainly to avoid electron multipacting in the cavity cell, which is a problem in cylindrical cavities [3]. It is made of niobium, a metal that has superconducting properties below 9.2K. The cavity is contained in a cryostat (2) to keep it under the superconducting critical temperature at all times. The large beam tube and the extra fluting (3) allow any higher order modes to escape and be significantly absorbed by ferrite loads (4) on either side of the cavity. The aperture coupler is connected to a bend (5), which is also made of niobium. It leads to a heat exchanger section (HEX) (6) whose function is to ensure good insulation between the liquid helium cryostat and the liquid nitrogen (LN<sub>2</sub>) shield (7). The waveguide is a copper half-height waveguide (4" height by 17" width) and goes through a double E-plane bend (8) to a vacuum pumping section (two 50L/s pumps) (9) and from there to the window (10), which is in CESR's case a window manufactured by Thomson (now Thales) designed to withstand up to 1MW but only tested up to 500kW of power [4].

From there on the waveguide is air-filled full-height WR1800 type (9" by 18"), and does not present any particular problems. An ion pump (11) is close to the double-E bend and may leak stray magnetic fields into the waveguide, affecting its multipacting characteristics.

The first four cavities were built with a series of small copper ridges on the outermost inside wall of the double-E bend, designed to reduce the load on the cryostat due to heat transfer from the warm sections of the waveguide (pump and window). However, there was suspicion that the ridges were aggravating the breakdown problem, and they have been removed from all cavities from the 5<sup>th</sup> onwards. The 5<sup>th</sup> cavity has just been put into the ring at Cornell in replacement of the least reliable cavity. The performance of this cavity seems to differ little from that of the others in any respect.

### **1.3.3 Description of the breakdown observed in the CESR cavities**

The operation of the cavities at Cornell is sometimes hampered by vacuum bursts. When such a vacuum spike is detected at the pumping sections, interlocks set for the protection of the cavities shut the klystrons to down and dump the beam as a result [5]. Generally, the CESR ring is powered by four cavities, each working at approximately at 270kW at full beam power. On average, the machine suffers one or two trips per day, most particularly when peak current is reached. This frequency of trips is unacceptable for a dedicated synchrotron radiation source, and conservative estimates were made for the first Diamond specifications. Three cavities will be inserted to give 600kW of power, or 200kW/cavity, which is believed to be well below the onset of tripping. However, provision must be made for an eventual upgrade of Diamond, the objective being to allow a raise of the power provided per cavity to the highest possible level up to the window limit of 500kW. To achieve this, the reliability issue must be tackled and solved.

The great majority of the vacuum trips are detected [6] at the pumping section below the cryostat, (9) in Figure 4. Photo-multipliers viewing the ceramic window rarely show activity at such trips, so it is assumed that the trips occur at other locations in the waveguide, such as the pumping section, double-E bend, heat exchanger or niobium waveguide. It is also possible that the problem comes from other parts of the window area such as a pair of matching posts on the vacuum side. Vacuum peaks are however the only indicators of the trips.

The different cavities all have a different reliability records, depending mostly on the problems encountered during construction and the resultant surface contamination (due to particles or undesirable chemical reactions). Several cavities suffered various problems during assembly, occasionally requiring re-treatment or baking. It appears that the history of the cavity is one of the main factors to be taken into account, as illustrated by a recent cavity test [7] (the cavity was destined for SRRC) where the cavity suffered no major mishap during construction and out-performed all of the others. The waveguide is perhaps not such a critical area of the system as the cavity, but exercising the same degree of care during construction cannot be harmful.

The surface contamination problem alluded to in the previous paragraph is compounded by the fact that the waveguide is cooled by liquid helium (up to the HEX) and then liquid nitrogen along its length. This has the effect of enhancing the adsorption (cryosorption) of gases on the surface, possibly modifying its characteristics (as far as its secondary electron yield is concerned) and increasing the amount of gas that can be desorbed if there is localised heating. The gas species present in the waveguide have been measured at Cornell [8]. The main residual gases were found to be H<sub>2</sub>, H<sub>2</sub>O, CO and N<sub>2</sub>, condensing at different locations on the input waveguide.

The main suspect for the process by which heating on the walls may occur is a phenomenon known as multipactor. In succinct terms, this effect starts if electrons caught in a RF field fulfil certain resonant conditions and if the amplification due to the secondary electron yield at the walls is greater than the any losses incurred through collisions or other effects. The result is a rapidly increasing stream of electrons that draw ever more power from the RF and heat the walls. This phenomenon is almost unavoidable from a given power level as the possibilities for resonant conditions to be met, added to the high secondary electron yields of many accelerator materials, generally ensure that there will be favourable conditions. However, multipacting can be brought under control and is rarely damaging. Its main effect is to draw power from the RF, reducing the efficiency of the system. In the case of the CESR waveguide, the fact that the walls are covered with cryosorbed gases aggravate the problem since heating can release gases and lead to the formation of ionised gas, which could induce a low pressure gaseous discharge. It is also known that the breakdown problems can be alleviated by warming-up the cavities (allowing cryosorbed gases to evaporate) then cooling the cavities down again. This temporary fix gives several weeks of relatively trouble-free operation before gas once again condenses to problematic levels.

An aggravating factor was discovered quite recently (May 2003), in that the niobium coupler area (marked (5) on Figure 4) of a cavity that had failed during a test was found to have suffered from compression due to a pressure difference between the inner vacuum and the outer vacuum (used to insulate the cold areas from outside). The observed cave-in was quite considerable. It is likely that it occurs in a slightly less severe form in the operational cavities as a mismatch was observed between the calculated and measured  $Q_{external}$  of a number of cavities (such a deformation would introduce an impedance mismatch). Such a deformation would affect the multipacting behaviour of the coupler by lowering the threshold power for multipactor in that region.

Another possible suspect for the trips is field emission, though it is unlikely to happen in the waveguide as fields are generally lower than the threshold. It may occur if any high-order mode is excited by the beam and resonates in various areas of the waveguide. One possible area of field emission was discovered by simulating the higher order mode fields on the vacuum side of the window for frequencies corresponding to different harmonics of the beam. One of those resonant fields displays very high field concentrations around the matching posts and could conceivably induce field emission or breakdown due to the proximity of the wall.

#### **1.4 Research objectives**

The main object of the research is to ensure that solutions be found so that the DIAMOND cavities could perform at high power levels. It is therefore important to identify and understand the mechanisms behind the phenomena that occur in the waveguide. Once identified, it becomes possible to look for methods that would weaken or suppress the phenomena causing the vacuum breakdown in the input coupler waveguide. In order to achieve this, a program of research combining numerical simulations with experimental observations was implemented.

## 2 Multipactor

### 2.1 *Brief history of multipactor*

Multipactor was first recognised and named by P.T. Farnsworth in 1934 [9]. He saw it mainly as a means to amplify signals. He designed and constructed vacuum tubes that he named Multipactors, and demonstrated them in 1936. He also intended to use the tubes in television sets to amplify the then feeble photo-current, but his design was soon superseded by Zworykin's Iconoscope that gave better inherent sensitivity.

E. W. B. Gill and A. von Engel identified multipactor again in 1948 [10]. Their purpose was to study low-pressure gas discharges, when they encountered and recognised the multipacting phenomenon and mechanism. They wrote an analytical description fitting the measured data.

A.J Hatch and H.B. Williams expanded in 1958 [11] on the work accomplished by Gill and von Engel. They examined the behaviour of higher orders of multipactor and compared theory to experimental results to provide a scaling law that defines multipacting zones as a function of gap, frequency and applied electric field.

W.J. Gallagher [12] expanded in 1979 the theoretical description of the phenomenon to study its effect in RF cavities, where multipacting began to be a limiting factor.

J. Rodney M. Vaughan [13] wrote in 1988 a comprehensive review of the phenomenon, including descriptions of its manifestations and means of detection as well its analytical treatment.

Recently, much more attention has been paid to the phenomenon, from the point of view of both accelerator and vacuum tube development but also satellite based applications [14]. In all of these cases, multipactor is a parasitic effect that prevents the system from operating at its full potential, by draining part of the RF power and possibly causing damage or vacuum bursts. The means to study multipactor have changed as well, and greater reliance is placed on simulation than was previously the case, when often the only way to detect and study multipactor was to make a prototype. Whereas in the past the complexity of the multipacting electron trajectories was too great for computers to solve, improvements in computer technology meant that these could now be calculated,

in both 2D and 3D cases [15]. Another reason for the renewed interest is that the power level in cavities and couplers is increasing to a point where multipactor can truly become problematic and is frequently encountered by RF structures worldwide.

## **2.2 *Introduction to multipactor***

Multipactor is a resonant multiplication of secondary electrons. It can occur when an electron, caught in an RF field, impacts with a solid at sufficient energies to release more than one secondary electron, at a phase where the RF field can accelerate these secondary electrons. If their trajectory is such that they impact with the wall at an energy that allows further multiplication and phase that allows the new electrons to escape the wall and impact elsewhere in similar conditions, the phenomenon can build up into a multipactor discharge. A more complete description of the phenomenon is given in section 2.4.

## **2.3 *Secondary electron emission***

### **2.3.1 *General properties***

Good general reviews of secondary electron yield properties can be found in [16,17].

A surface struck by incoming primary electrons (or any energetic particle) may release a number of electrons depending on the primary electron energy. The electron yield is dependent, among other things, on the type of material, the surface conditions and the primary electron energy and angle of incidence.

Secondary electrons are typically created from the excitation of conduction electrons in metallic systems or ionisation processes in dielectrics. In addition to these true secondaries, electrons returned can be primary electrons returned through elastic or inelastic backscattering on the surface. In the second case, an inelastically backscattered electron may also release secondary electrons as it loses energy in the surface.

Electrons returned from a surface can have energies ranging from near zero to the energy of the primary particle, as seen in Figure 5. At typical primary electron energies, such as 1keV, the returned electrons can be divided into two groups, the 'true' secondaries and reflected (backscattered) electrons. The former can generally, somewhat arbitrarily, be said to have energies below 50eV, the later more (assuming that

the primary particle had a sufficient energy). In addition, there are small peaks near the elastically backscattered electron peak that correspond to Auger electrons. For the purpose of our study, these may be discounted as they generally do not contribute significantly to the number of returned electrons.

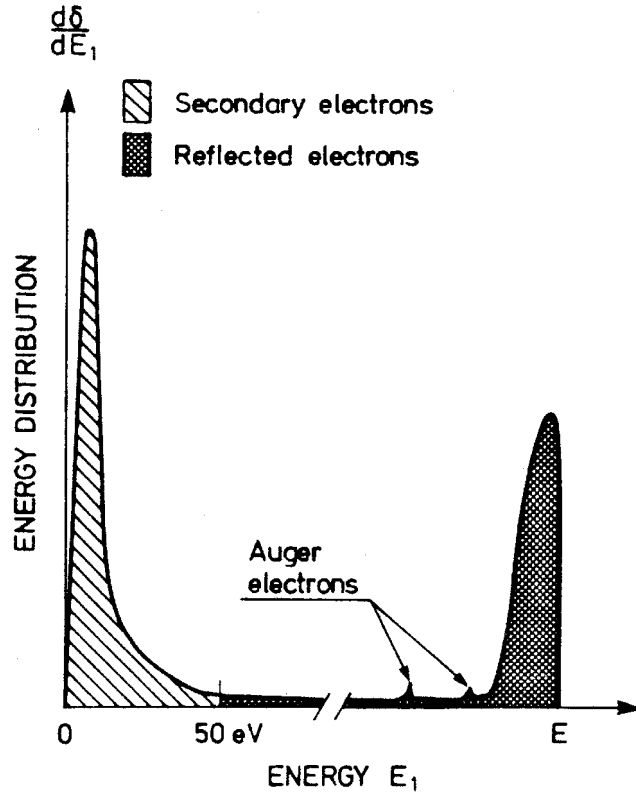


Figure 5: Schematic energy spectrum for secondary electrons (from Schou[16])

The total yield  $\xi$  of returned electrons per primary may be expressed as

$$\xi = \delta + \eta$$

$\eta$  and  $\delta$  being the contribution to the total electron yield of backscattered and true secondary electrons respectively. As the fraction  $\eta$  of backscattered electrons does not directly contribute to any amplification (the same electron as was incoming is backscattered off the surface, so the number of electrons in the vacuum remains constant), we will concentrate on the true secondary electrons whose yield is  $\delta$ . The main instance for which we will consider the backscattered fraction of the electrons is for very low energy electrons (less than approximately 10eV) where they greatly outnumber the true secondary electrons. At such energies, a significant proportion of electrons are reflected upon impacting with a surface [18, 19, 20]. The relative proportion of reflected vs. true secondary electrons can be seen in Figure 6. Figure 7 shows the contribution of backscattered primary electrons to the secondary electron yield of a copper surface,

highlighting the importance of taking backscattered primary electrons into account at low primary electron energies. It is estimated that 50% of electrons are backscattered on copper and stainless steel surfaces at very low incident electron energies [19]. This value is the one used in the MAGIC code detailed in section 3.5.1. The main reason for keeping track of these electrons is that most models underestimate the number of low energy electrons returned by a surface.

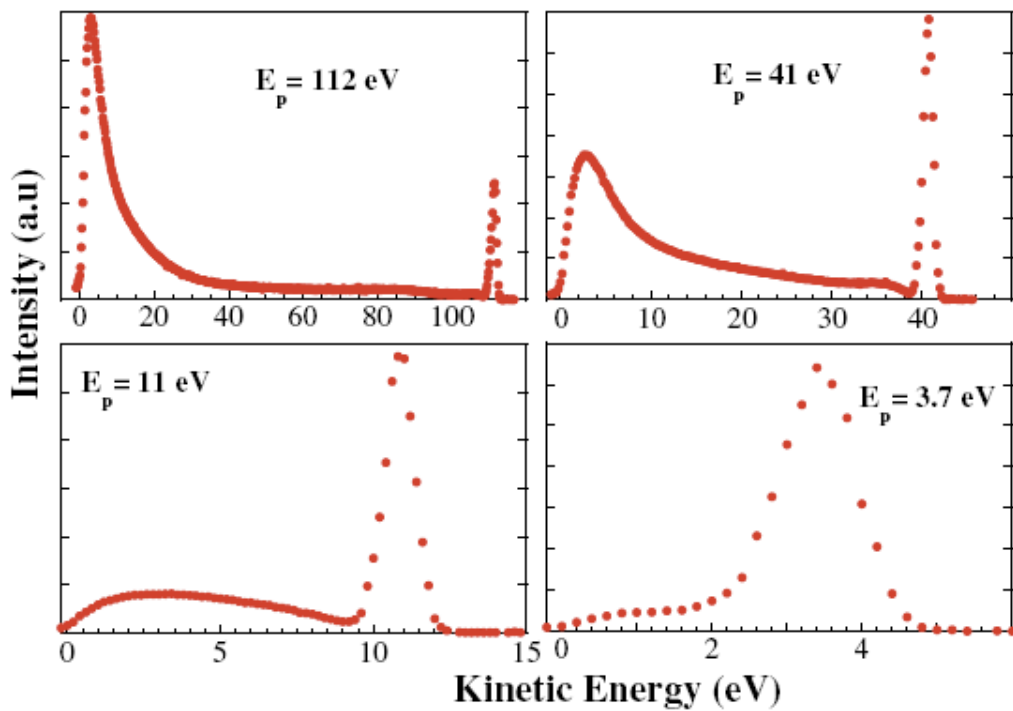


Figure 6: Measurement of the electron energy distribution curves from a scrubbed Cu surface at 10K at various primary electron energies (from [19])

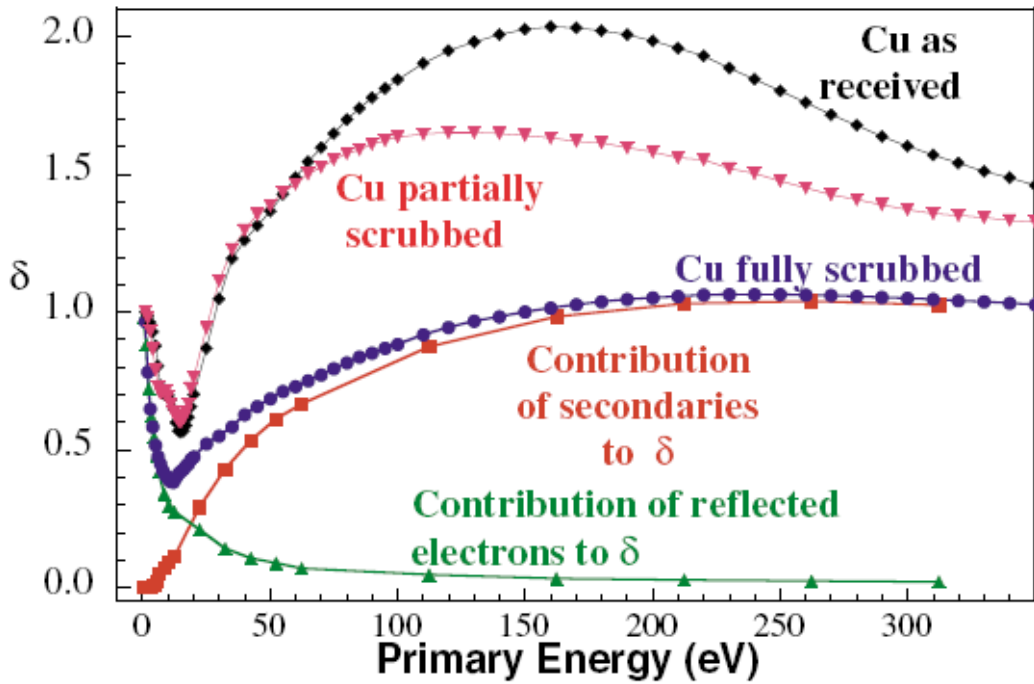


Figure 7: Contribution of true secondary and backscattered primary electrons to the electron yield of a scrubbed Cu surface (10K) (from [19])

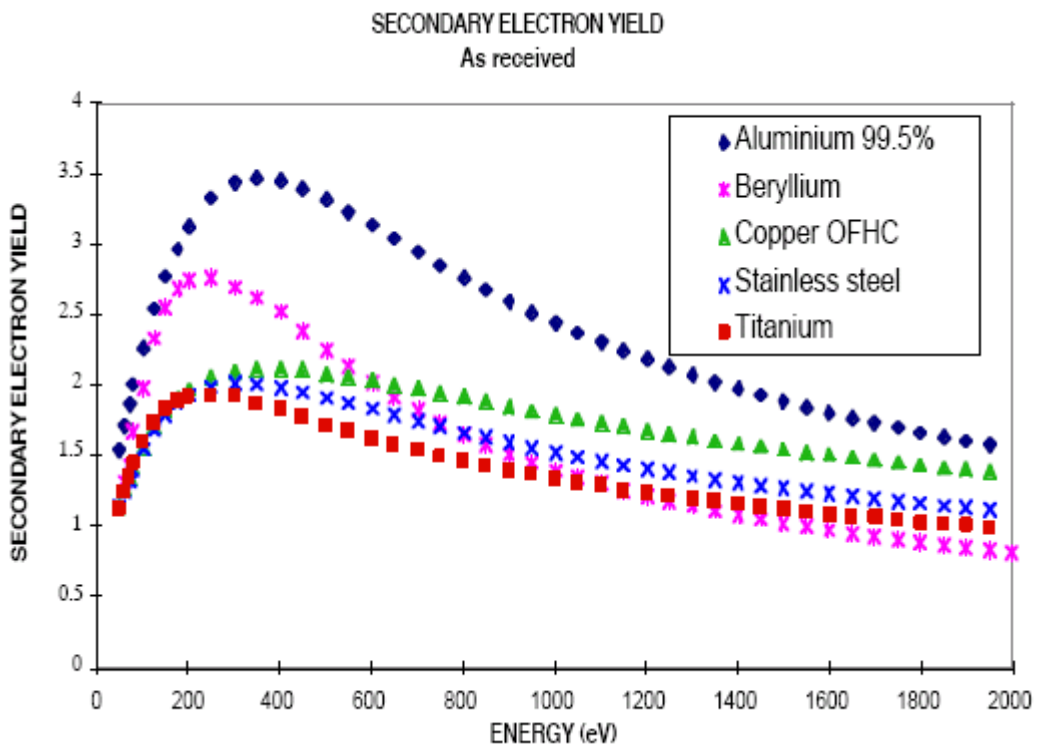


Figure 8: Secondary electron yield of typical metals in function of primary electron energy [25]

The process of secondary electron emission can be split into three stages:

- primary ionisation by the bombarding particle during penetration as well as secondary ionisation by energetic secondary electrons;
- migration of a portion of the secondary electrons to the surface;
- escape of these electrons through the potential barrier at the surface.

The dependence of  $\delta$  on primary electron energies is complex, and although many models have been used to attempt to calculate the yield (a good example is [21, 22]), values measured from actual samples are often more useful when dealing with real systems. Indeed, in addition to the contribution from the intrinsic properties of the material, the yield is greatly influenced by condition of the surface (topography, presence and nature of contaminants). Generally speaking, experimental observations lead to the following conclusions:

- The electrons migrate from a thin escape zone on the surface (in the order of .5 to 5 nm for metals, larger for insulators). This is illustrated in Figure 9 (albeit for a 40keV electron beam, which is more energetic than the electrons that we will typically be concerned with when studying multipactor)

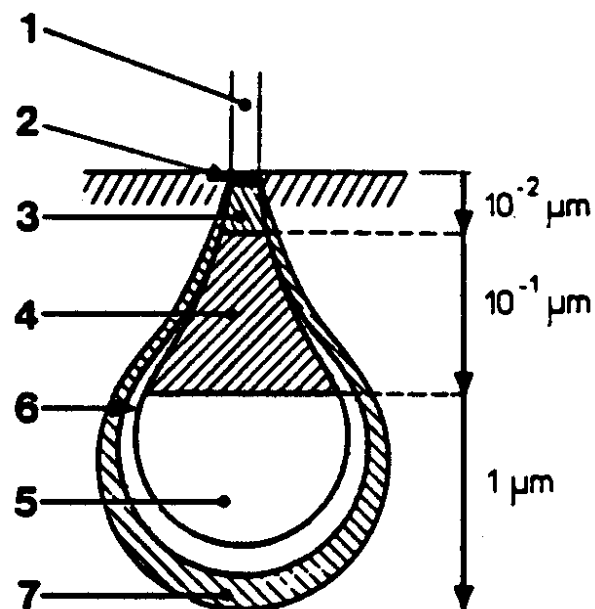


Figure 9: Interaction regions for an electron beam impacting a solid. The penetration depths shown are for a 40keV beam. (1) Primary electron beam; (2) Auger electron region; (3) secondary electron region; (4) backscattered electron region; (5) characteristic X-ray region; (6) background X-ray region; (7) fluorescence X-ray region (from [23]).

- The angular distribution of secondary electrons from poly-crystalline surfaces is well represented by a cosine function [17]. Mono-crystalline surfaces may show anisotropy. An illustration of a cosine distribution is shown on Figure 10.

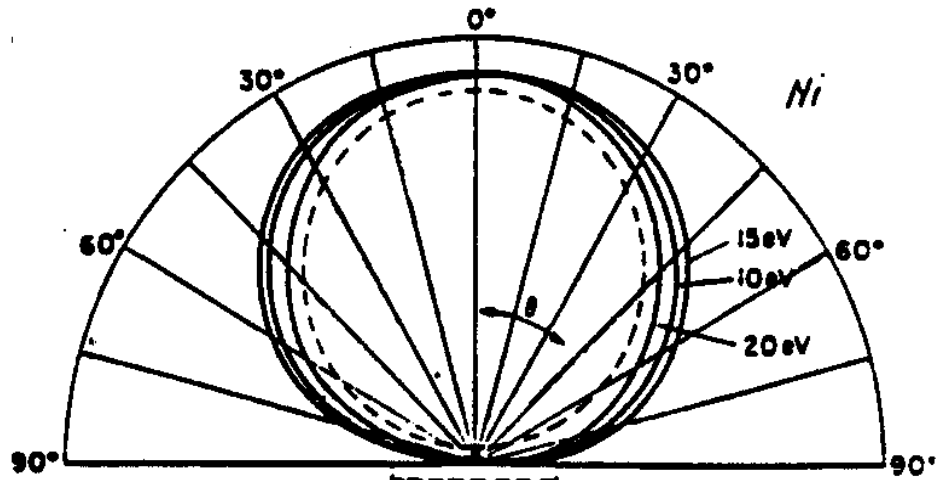


Figure 10: Azimuthal distribution of true secondary electrons (from [23])

- The shape of the energy distribution of the re-emitted electrons is generally considered to be insensitive to the energy or angle incidence of the primary electrons.
- The maximal value  $\delta_{max}$  of the yield is generally at primary electron energies at or below 1keV. For copper, it is around 220eV, for stainless steel it has been measured around 300eV [19]. See also Figure 17 for another measurement of secondary electron yields for common accelerator materials.
- The yield  $\delta(\theta)$  increases with the angle of incidence of the electrons (as they have less thickness of material to escape from at similar primary energies). A simplified schematic illustration of that is shown in Figure 11. An illustration of the effect is shown on Figure 12.

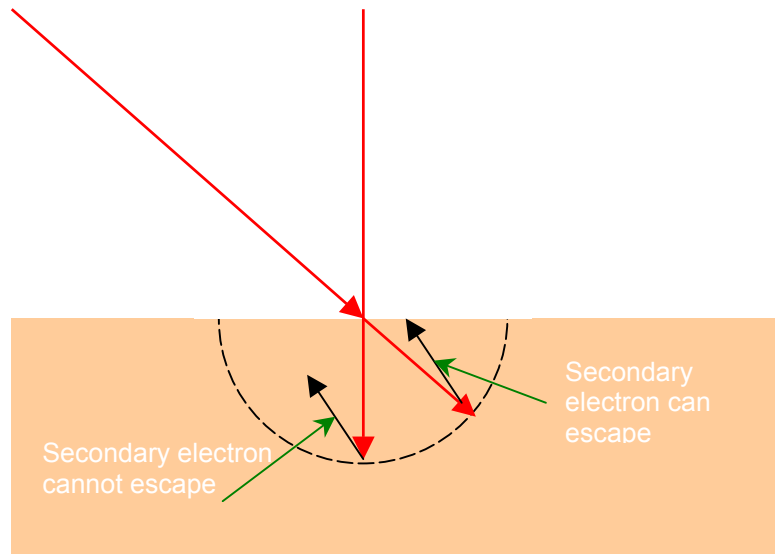


Figure 11: Effect of the incident electron angle on secondary electron yield

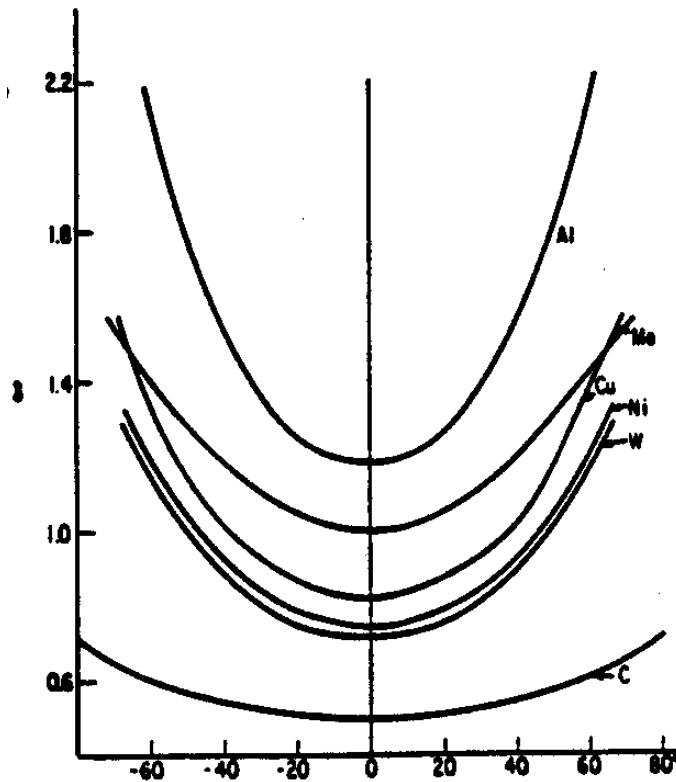


Figure 12: Variation of the secondary emission yield with the incidence angle of a primary electron for typical metals (from [23])

- The yield is generally larger for insulators than for metals (by a factor of ten for some dielectrics).
- For metals and alloys, the yield is substantially independent of temperature [24].

### 2.3.2 Reducing the secondary electron yield

The electron yield of materials in an accelerator environment is very different from that of the ideal sample one might study in a lab. The material is usually covered by a thin (a few tens of nm [25]) surface layer of contaminants. In the case of metals, for instance, one will find that they are covered with an oxide layer after being exposed to air. For most metals used in accelerators, this means that the electron yield is considerably increased (i.e. for an Al alloy 6061, the 'pure' sample was measured at  $\delta_{\max} = 1$ , whereas with contaminants, a value of  $\delta_{\max} = 3$  was measured [25]).

The easiest method to get rid of the surface contaminants is usually simply to run power through the system (this operation is commonly called processing). In the case of a waveguide, for instance, this will not only heat up the wall through resistive heating, but also allow multipactor to form (if the conditions are such that it can happen) and the electrons hitting the wall will help clean the surface. An example of the effect of processing can be seen in Figure 13 where the reduction in the secondary electron yield was measured for various amounts of bombarding electrons on the surface. It is of course essential that the system be sufficiently interlocked so that no damage can occur to any of the structures from excessive heat deposition into the material.

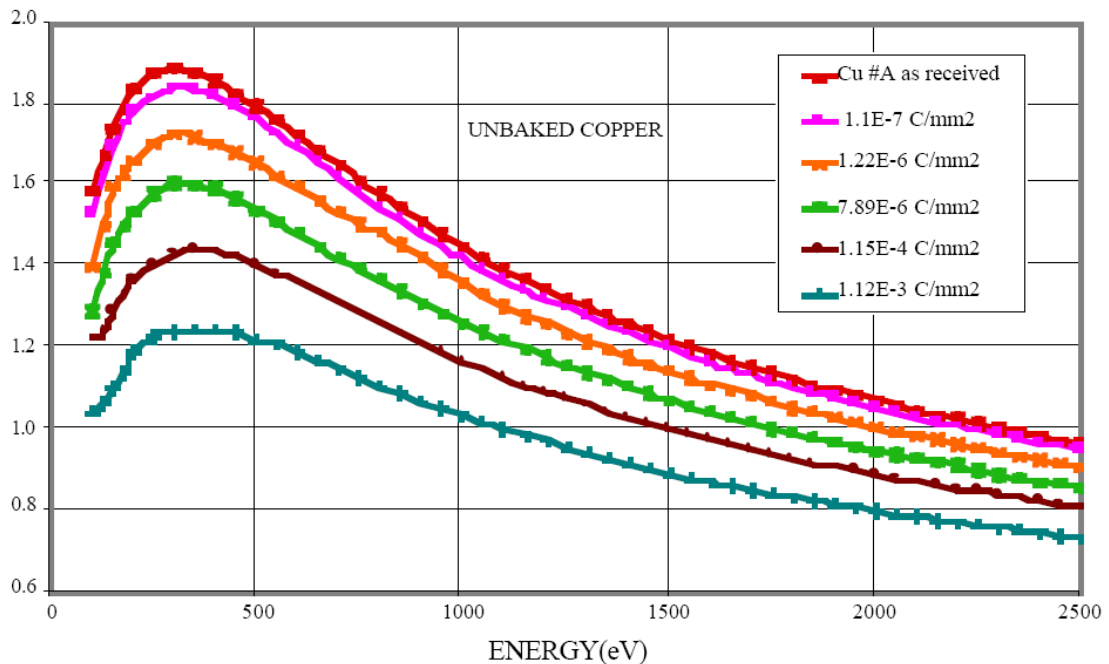


Figure 13: Variation of the secondary electron yield of copper with the accumulated electron dose (from [25])

## **2.4 Mechanism of multipactor**

In the first approximation, such as for a simple two plate system (see Figure 14), the multipactor effect can be described as a resonant phenomenon which occurs when the electron travel time for wall to wall trajectories is a multiple of half the RF period, in conditions where the secondary electron emission yield of the walls allows the electrons to multiply at each cycle and eventually build up into an avalanche.

When the trajectory is such that the electrons return to their initial position, it can be called one point multipactor. Should the trajectory of the electrons loop between two impact points, it becomes two point multipactor and so on. The order of the multipactor is defined as the number of RF periods taken for the electron to transit from its creation to its impact with a wall (in the case of two point multipactor, the electron takes  $2n-1$  half periods to reach the other wall, where  $n$  is the order). An illustration of this can be found in Figure 14.

Multipactor also occurs in more complex systems than a two-plate geometry, such as waveguides, accelerator cavities, or even space-borne antennae on satellites. It then becomes more complex to describe, but the underlying mechanism remains the same.

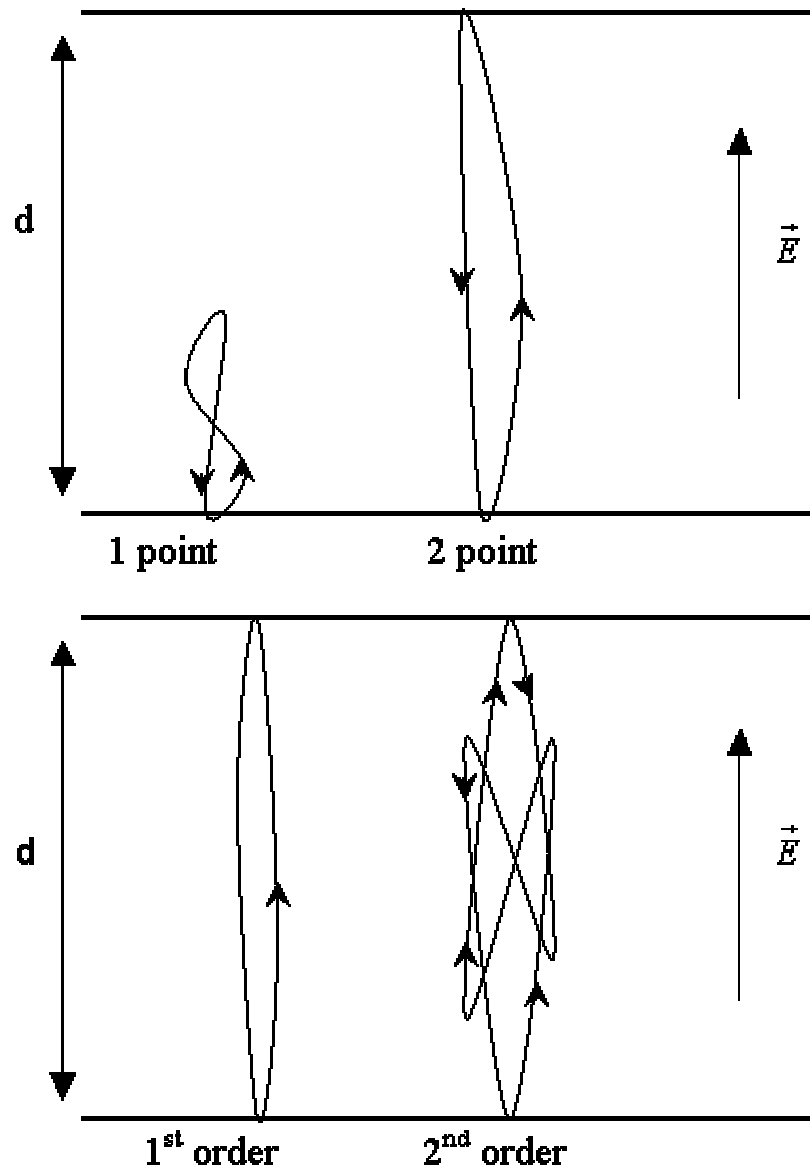


Figure 14: Illustration of simple types of multipactor in a simple two surface geometry

The number of electrons emitted from the surface after an electron impact depends on the secondary electron emission coefficient of the surface and of the angle of impact as described in Section 2.3.1. Secondary emission properties of materials have been well studied for most typical accelerator materials, both theoretically and in practical operating conditions [25] (see also Figure 17). For most materials, the secondary emission is maximised at electron energy values between 100eV-1keV. Multipactor is therefore a relatively low energy phenomenon.

More generally, any condition allowing electrons to multiply can be a form of electron multipactor. The condition for multipactor does not require a yield greater than unity for

every impact, as long as the product of the yields over all impacts is greater than unity; the overall effect is a multiplication of the electrons. This is particularly relevant in cases involving low energy electrons that may drift for some time before being caught by multipacting conditions.

The field giving energy to the electrons is generally an electromagnetic field that is the primary function of the system (such as in RF waveguides or cavities, or satellite communication systems). It may also be a by-product of the primary functions of the system. This occurs, for instance, in the case of electron clouds, where the electromagnetic fields are created by the space charge of particle bunches in an accelerator drift tube. These can cause electrons in the drift tube to impact with the drift tube walls.

Multipactor occurring on dielectrics [26, 27, 28] also has to take into account the positive charge build-up in the dielectric due to the freed secondary electrons. Multipactor on dielectrics does not necessarily require synchronism with the RF, as the attraction by the positive charge can be sufficient to create a self-sustaining cascade. This type of multipactor can happen on RF windows, which are frequently made of materials with a very high secondary emission coefficient.

## ***2.5 Methods of multipactor suppression***

Multipactor can be undesirable in a great many circumstances. Unfortunately, it is quite difficult to achieve suppression in real-world situations where the complexities generated by geometry and materials tend to work to your disadvantage. Suppression can be achieved by preventing one of the two basic mechanisms of multipactor, namely the phase and the multiplication requirements.

### **2.5.1 Suppression of multipactor through geometrical changes**

In theory, the easiest way to suppress multipactor is to prevent multipacting trajectories from existing. This can be easily done in very simple cases such as a two plate geometry, but becomes much more difficult to achieve in realistic geometries given the great number of possible multipacting trajectories. In a two-plate geometry, there are well-defined multipacting bands for which electrons in transit impact on a wall at phases such that their energy is sufficient to release multiple secondary electrons, and that the

secondary electrons can escape the surface. A representation of this is the diagram commonly referred to as a Hatch diagram, an example of which is shown in Figure 15. It shows the existence zones for multipacting bands for various gap field strengths as a function of frequency multiplied by gap distance. These zones have been calculated by using an analytical description of multipactor [11].

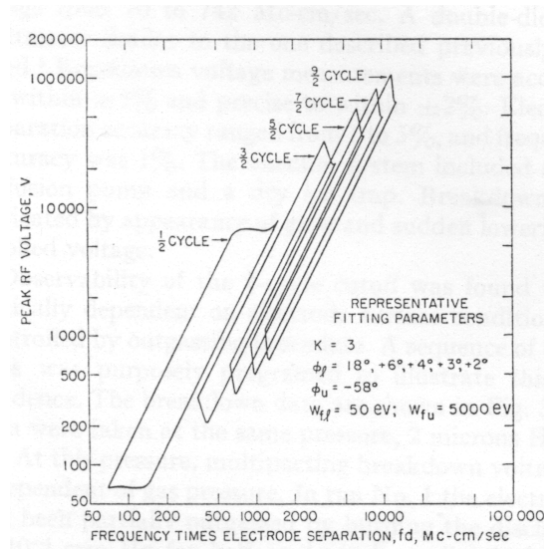


Figure 15: Diagram from [11] showing areas corresponding to 1<sup>st</sup>, 2<sup>nd</sup> and 3<sup>rd</sup> to 5<sup>th</sup> order multipactor as a function of V over frequency and gap distance for a two-plate system

The following graph shows the results from a simple numerical model of electron multipacting in a rectangular waveguide, taking geometrical considerations into account. It shows that there are many power levels for which multipactor should not be able to exist.

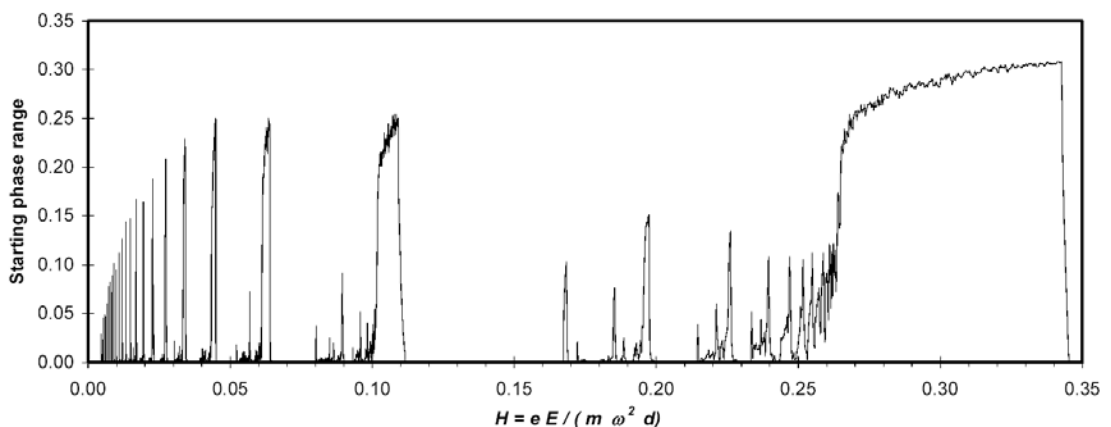


Figure 16: Multipacting bands expressed in terms of the phase range allowing electron return plotted against a function of the electric field (from [31])

By choosing a gap width or a frequency such that electron multiplication cannot happen, it is possible to prevent multipactor from occurring in the system. As geometries become more complex, however, the number of resonant modes greatly increases and the likelihood that no multipactor enhancing conditions exist is very slim. What previously happened was that if multipactor was thought to be problematic for a given system, it was often possible to shift its location by trial and error to somewhere less damaging by applying simple changes to the geometry. Should a more complete suppression be required, it becomes necessary to fully understand the modes by which multipactor occurs. Once these have been understood, it may be possible to force the electrons to adopt trajectories that do not lead to multiplication. An example of such a study is that carried out on coaxial waveguides for the Tesla design study [35, 39]. In that case, the trajectories can be altered by applying a static electric field between the inner and outer conductors of the coaxial waveguide.

### **2.5.2 Suppression of multipactor by preventing electron multiplication**

Multipactor relies on the multiplication of electrons as much as the trajectories and impact phases. Should no mechanism exist for electron multiplication, the phenomenon cannot build up to multipactor. Unfortunately, most materials have maximum values of their secondary electron yield that are greater than unity. To further complicate the process, impurities or condensed gases on the surface also generally have electron yields greater than unity.

Figure 17 shows the electron yields measured for materials typically used in accelerator systems. The measurements were made for 'as received' samples of the materials, meaning that the surfaces were clean but not baked or otherwise treated. It shows that most metals have similar properties, apart from aluminium that has a higher yield than the others. This is due to the oxide layer that can easily grow on the surface of aluminium; pure aluminium has a much lower yield ( $\delta \sim 1$ ) that can be reached when the oxide layer and other contaminants has been stripped from the surface [25]. The peak yield of all of the metals measured above is in the vicinity of 400-500eV.

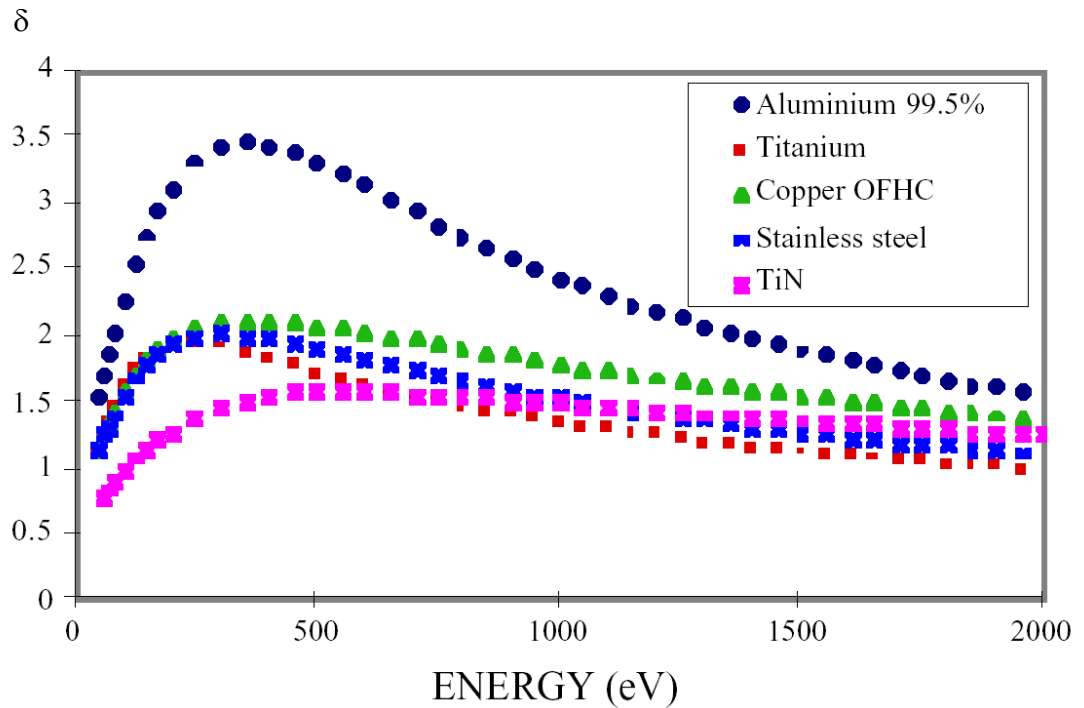


Figure 17: Typical secondary electron emission curves for various materials [25].

RF windows are made from dielectrics such as alumina, which has a very high secondary electron yield. This has led in the past to many window failures due to electron multiplication near the surface, some of which may have been started by multipactor. To combat the problem, coatings such as titanium nitride [29] or copper black have often been applied to window surfaces to reduce the yield. The difficulty is that while the window material is chosen for its transparency to RF, the window coatings are not. This leads to heating on the window surface by RF absorption, or reflection of the incident RF wave if the coating is conducting (such as a Ti coating), either of which may lead to window failure. The thickness of the coating on the window is therefore crucial and a compromise is generally sought between anti-multipactor protection and window performance.

Coatings on a waveguide would not be constrained to such stringent compromises since the waveguide does not suffer from the same cooling difficulties (even stainless steel has much better thermal conductivity than alumina). Waveguides are generally made of metals such as stainless steel, aluminium or copper; niobium is often used in superconducting sections. Any attempt to reduce the secondary electron yield of the surface with coatings would not run into the same problems as for windows. The limit on the coating thickness is likely to be the RF losses caused by the less than perfectly

conducting properties of most coatings (DC resistivity of  $1.3 \cdot 10^6 \Omega \cdot m$  for bulk room temperature TiN [30] compared to  $15.8 \cdot 10^{-9} \Omega \cdot m$  for copper). The issue would then be one of RF transfer efficiency. Difficulties would however arise in the cold and super-conducting sections of the waveguide where the heat generated by RF losses might affect the cooling efficiency and possibly the super-conducting properties of the substrate metal.

Another common yet undesirable source of high secondary electron yield is the presence condensed gases on the waveguide walls. These tend to form in any vacuum system, particularly in colder sections of the system. As most condensed and adsorbed gases present a high secondary electron yield, it is essential to minimise the adsorption of gases in areas exposed to RF, particularly if multipactor can form at that location. Thankfully, RF and multipactor both help strip the surfaces of gases and therefore improve the condition of the surface. This will be dealt with in more detail in section 5.2.4.

## 3 Multipactor simulations

### 3.1 *Methods of simulation*

Multipactor is a complex phenomenon, particularly in cases where the field distribution is itself complex. Nonetheless, it is possible to analyse it using numerical methods and by making certain assumptions. The objective of multipactor simulation codes is ultimately to be able to predict areas where multipactor can happen. Unfortunately, this is still very difficult to do and most codes are actually used after the fact, to study a multipactor problem that has been detected by experience, as in the case of the Cornell waveguides.

Several approaches can be attempted when describing multipactor numerically. The analytical approach is based on the mathematical derivation of the equation of motion in the electromagnetic fields. This method is mostly useable in the very simple cases where the fields and boundary conditions can be described in analytic terms. The method also does not take into account every possible electron trajectory (e.g. it does not take asymmetric trajectories into account [31]). For more complex problems, it is necessary to resort to numerical calculations. Numerical methods can include the tracking of single particles across a wide phase-space through a numerical integration of the equations of motion, or particle in cell simulations that have the advantage of being able to take other effects such as space charge into account.

### 3.2 *Analytical description*

The analytical description of multipactor is quite simple in the first approach. It starts with the equation of motion applied to the Lorentz force, which is all that affects the electron in the vacuum waveguide, where  $q$  is the electron charge and  $\vec{v}$  the electron velocity.  $\vec{E}$  and  $\vec{B}$  are the electric field and magnetic induction field respectively.

$$\vec{F} = q(\vec{E} + \vec{v} \times \vec{B})$$

The integration of the equation of motion can lead to a formulation of multipactor behaviour in a rectangular waveguide, such as the formulation devised by V. Shemelin [32, 33] that is reproduced in section B of the appendix. The formulation can lead to the delimitation of existence zones for multipactor build-up using conditions on the impacting electron energies such that the secondary electron yield is greater than 1. Figure 18

shows the power levels for which multipactor build-up leads to a yield greater than unity, using an analytical model applied to a rectangular waveguide, with the underlying assumption that multipactor occurs only in the centre-plane of the waveguide (highest E-field region).

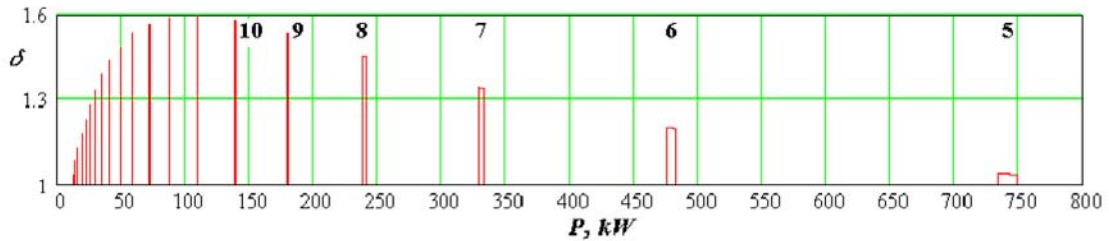


Figure 18: Existence zones of multipactor in a CESR-type coupler (17"x4") allowing for normal components only of initial electron velocities (from [32])

The advantages of an analytical description of the phenomenon are that once the formulation is complete, calculation time is much shorter than for a similar numerical simulation. The downside is however that the description can only be done for very simple systems such as a rectangular waveguide, due to the simplifications inherent in the process. Once refinements need to be added, the analytical description quickly becomes very difficult to solve.

### 3.3 Numerical methods

Numerical methods follow a general approach that can be summarised [15] in three steps that can be applied to a wide range of 2D and 3D structures. The first step is the definition of the geometry of the system and of the RF fields within it. The second step, surface properties are defined and a large number of particles are introduced into the system. Particle trajectories are calculated for a number of initial conditions. The third step consists of identifying the resonant behaviour that may exist.

The description of the RF fields and geometry may come from an existing EM field solver like MAFIA or Superfish, or use their own field solver like some multipacting simulation packages. The crucial point as far as multipactor simulations are concerned is the quality of the RF fields in proximity to the surfaces. This is due to the sensitivity of multipactor to the electron phase. Since actively multipacting electrons tend to impact with the surface in a decelerating phase of the field, the accuracy of the simulated field near the surfaces is of paramount importance. If the surface fields provided by the field solver are not

smooth enough, a correction (i.e. by interpolation) is necessary to ensure more accurate results. Studies of the electron motion near a surface with mesh 'steps' induced by the finite difference grid show a 50-100% error in momentum for non-conformal surfaces [34].

Electrons are then introduced into the system and tracked over a number of RF periods. Their motion is then tracked by integration algorithms such as the Runge-Kutta method until they hit a wall. Many initial conditions can be considered, including variations of initial position, kinetic energy and direction. Field strength and starting phases can also be scanned. Particle histories, including impact times, locations, phases and energies are recorded. Some codes track all re-emitted electrons despite the fact that the surface conditions might be such that no emission is possible, and eliminate the unsustainable resonances at a later stage (counter function as described by P. Ylae Oijala [35]).

Surface properties relevant to the code include secondary electron emission, re-emission and scattering. Standard secondary electron yield tables exist but tend to only reflect the ideal properties of the surface. In reality, cleanliness and chemical treatments change these properties significantly.

The final step is the identification of resonant conditions. A possible method is to check if particle data falls within areas of phase space that fall within multipactor conditions. Most programs however use the concept of counter and distance functions developed at the University of Helsinki [35]. These functions are a statistical means to determine the survival of particles and the recurrence of initial conditions at re-emission. These functions are defined independently of material properties and secondary electron yield data. A modification, the enhanced counter function, allows the incorporation of material properties into the calculation. More detail on this method can be found in P. Ylae-Oijala's thesis [35].

A good review paper on multipactor simulation methods was presented by R.L. Geng at PAC2003 [36].

### **3.4 *Multipactor code development***

The development of a quite simple code was begun based on the Xing code developed by R.L. Geng at Cornell [37]. The code uses analytical formulations for the fields and an enhanced counter function mechanism. The electron trajectories are calculated via a 4<sup>th</sup>

order Runge-Kutta algorithm. The code will allow sweeps in starting position of the electron (along the longitudinal and transverse directions), the initial phase, electric field intensity and could incorporate many other possible scans. The difficulty lies in calculation time, as it can very quickly take unrealistic amounts of time to perform some of the more complicated simulations or of the more comprehensive sweeps of the parameters.

The code is however not yet reliable enough and has not yet been able to match the results obtained from Xing. It is however possible that further work on this code is not desirable as the experiments have shown the limits of the method. This is discussed in the following section.

### **3.5 The *MAGIC* code**

The *MAGIC* simulation code was developed by the Mission Research Corporation based in Virginia. It is a PIC (particle in cell) code, more specifically a finite-difference, time-domain code for simulating plasma physics processes (processes that involve interactions between space charge and electromagnetic fields). It has two components, a 2½D component for 2D calculations of 3D processes (for instance a cylindrical cavity) and a fully 3D component that allows calculations of more complex or non-symmetrical geometries.

*MAGIC* suffers from the limitations inherent to finite difference codes, in that the mesh depends on the division of each coordinate into segments. In a rectangular geometry, each mesh cell will be a rectangle of finite dimensions  $dx$ ,  $dy$  and  $dz$ . The limitation comes from the definition of objects that are not conformal with the mesh, meaning that some or all of the faces defining its geometry are not perpendicular to one of the axes. For such objects, the fields in the vicinity of the surface cannot be calculated accurately by the code.

Commands are entered through an input command file, which is then compiled and run by the program. The help files and examples provided were sufficient to allow basic understanding of the possibilities and to program the simulations of interest. A training course given by *MAGIC* developer L. Ludeking helped me in understanding some of the more advanced features.

MAGIC allows the tracking of particles affected by electro-magnetic fields. The particles used by the code are macro-particles representing a number of electrons (in our case). The charge of those macro-particles is therefore much larger than the charge of an individual electron, but this simplification ensures that high charge phenomena can be studied with realistic memory and processing times. The drawback is that the simplification introduces an error into the process and if too few macro-particles are present in the system, unrealistic results may be produced.

### 3.5.1 Simulation of a rectangular waveguide geometry

#### 3.5.1.1 General method

Using the 3D code, the geometry itself is quite simple to define. It consists of a parallelepipedic void (defined in a Cartesian coordinate system), bounded on the sides with perfectly conducting walls (defined by a slightly larger parallelepiped set around the void) and on either end with ports. One of the ports is set as an input port, for which a  $TE_{10}$  RF mode is defined. The other port is defined as an output port (no incoming RF wave). If a standing wave case is to be studied, the easiest solution is to replace the downstream port with a perfectly conducting plate.

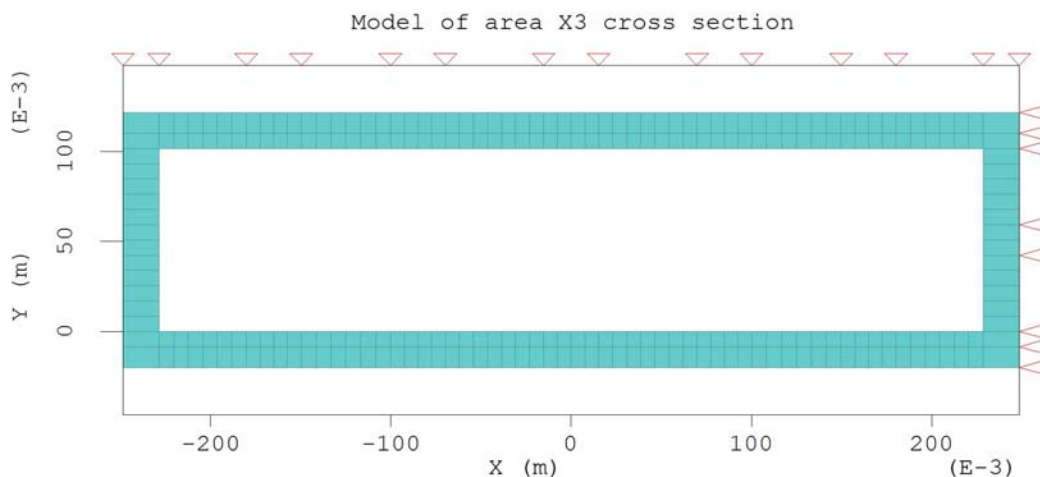


Figure 19: Cross section of the simulated waveguide looking down the RF propagation axis

The study of grooves or other surface modifications can be achieved by adding relevant geometry definitions (a groove would be a parallelepipedic void cut into the side of the wall, as shown in Figure 20). The difficulty resides in the size of those geometrical details compared to the mesh size. The simulation is generally quick to run, assuming modest mesh requirements, but when modelling geometrical details with a sufficient mesh density, simulation times can quickly become prohibitive. MAGIC simulations are

therefore best used to verify the multipactor behaviour of specific geometries, rather than scanning through a great number of them.

Typically, the mesh across a groove (or other small detail) would need to encompass several mesh points (minimum of four). The mesh across the rest of the waveguide should not require such a mesh density, and it is possible to have a variety of mesh densities across the volume. A study of the effects of the mesh density can be found in the appendix.

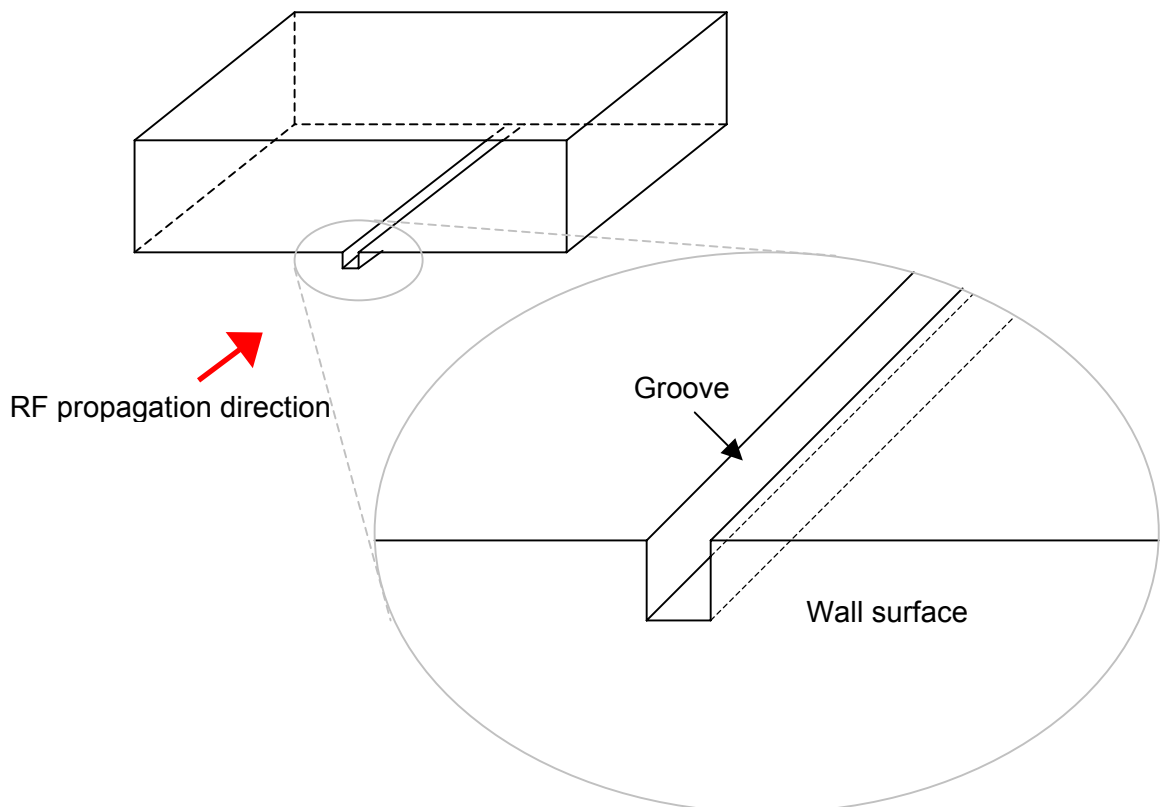


Figure 20: Schematic of a grooved waveguide as can be modelled in MAGIC

Secondary electrons are included in the code and are implemented in a flexible manner. It is possible to define custom functions for the secondary electron yield and emission energies to suit the case studied.

The formula initially used in the simulations for the secondary electron yield is:

$$\delta(E_{\text{impact}}, \theta, t) = 0.5 \quad \text{for } E_{\text{impact}} < 5\text{eV} \quad (1)$$

$$\delta(E_{\text{impact}}, \theta, t) = (2.72)^2 \delta_{\text{max}} \frac{E_{\text{impact}}}{E_{\text{peak}} \cos(\theta)} e^{-2\sqrt{\frac{E_{\text{impact}}}{E_{\text{peak}}}}} \quad \text{for } E_{\text{impact}} > 5\text{eV} \quad (2)$$

Where  $E_{\text{impact}}$  is the impact energy,  $\theta$  the impact angle,  $E_{\text{peak}}$  and  $\delta_{\text{peak}}$  the energy and value of the secondary electron yield distribution at its peak. The first part of the equation is an attempt to model the very high reflection ratios of low energy electrons, as observed for instance by the LHC vacuum group at CERN [18]. Shows a yield curve such as was typically used during simulations. For the secondary emission energy, a gaussian distribution (good as a first approximation) was used centred on 3eV.

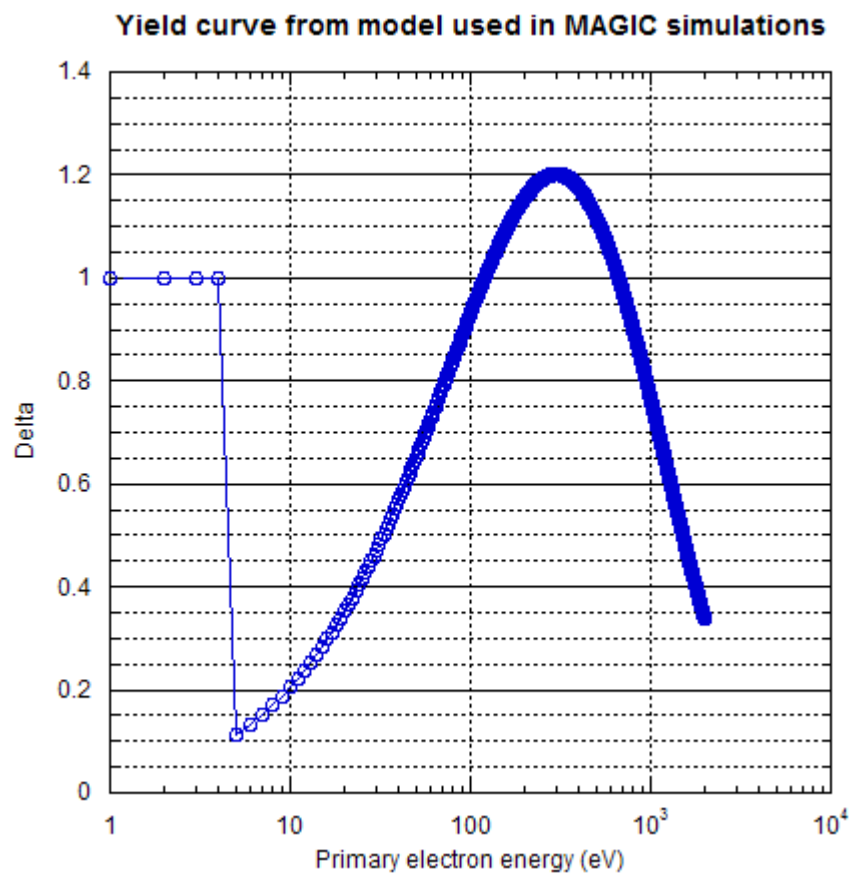


Figure 21: Yield curve used for MAGIC simulations with  $E_{\text{peak}}=300\text{eV}$ ,  $\delta_{\text{peak}}=1.2$ ,  $\delta_{\text{low energy}}=1$  and  $E_{\text{step}}=5\text{eV}$

An alternative parametrisation of the secondary electron yield is given in [38]. It incorporates a correction allowing for the reflection of low energy electrons. The basic formula used was the following:

$$\delta_s = \delta_{\max} \frac{s \left( \frac{E_p}{E_{\max}} \right)}{s - 1 + \left( \frac{E_p}{E_{\max}} \right)^s} \quad (3)$$

where  $\delta_{\max}$  is the SEY at the peak energy,  $E_{\max}$  is the energy at which  $\delta = \delta_{\max}$  and  $s$  a fitting parameter. The fraction of reflected electrons is given by

$$\ln(f) = A_0 + A_1 \ln(E_p + E_0) + A_2 (\ln(E_p + E_0))^2 + A_3 (\ln(E_p + E_0))^3 \quad (4)$$

which allows us to write the total yield as

$$\delta_{\text{total}} = \delta_s \frac{1}{1 - f} \quad (5)$$

The fitting parameters for copper and a low energy fit for the reflected electrons are given in [38], and are reproduced below.

<u>Parameter</u>	<u>Value</u>
$\delta_{\max}$	2.03
$E_{\max}$	262
$s$	1.39
$A_0$	20.70
$A_1$	-7.076
$A_2$	0.4835
$A_3$	0
$E_0$	56.91

Applying either of these models for the secondary electron behaviour shows a simulated behaviour that appears to be close to what was measured in the experiments carried out at Cornell, as will be detailed later. Most simulations were run with the first, simpler model of the secondary electron yield, as it gave more control over the yield parameters.

Primary electrons were seeded in a somewhat artificial manner by emitting electrons from a wall (EMISSION BEAM), typically for a duration of one RF period. This allows seed electrons to be emitted at every value of the RF phase, and should suffice to cover all possible cases. The initial electrons are emitted with the same energy as the centre of the secondary electron energy distribution.

Measurable output can be, for instance, field values at specific points in the geometry, charge in a volume or charge or power deposited on a surface at different times. Quite useful output, though unquantifiable, are the various plots, such as the phase space plot of particles that allow tracking of the various macro-particles. Among the information provided by these measurements are the sustainability of the multipactor discharge (dependent on the rate of increase of the secondary electron current or accumulated secondary electron charge), or the order of multipactor and impact points of the multipacting electrons as can be measured from the phase space plots.

The code allows a good visualisation of the development and progression of the initial stages of a multipactor discharge. The videos that can be produced can, for instance, illustrate why during the experiments the probes on the sidewalls picked up so many electrons where few were expected according to the results of particle tracking codes that select only the electrons that will lead to further multipactor. The secondary electrons being produced at random emission angles, means that they will have variations in tangential initial velocities and will tend to drift apart. Even when the emission velocities are limited to a single value (no distribution), the drift caused by the emission angles is sufficient to scatter the initially well-packed bunch that is emitted from the wall. This ensures that electrons hit the opposite wall with a big spread in RF phases, possibly explaining why the experiments failed to measure well-defined bands but rather a continuous power region where multipactor existed. This spread is never taken into account by most codes, yet it is believed that it is quite important in its effect, particularly for higher order modes of multipactor such as the present case.

Another factor that becomes apparent is the importance of taking the reflection of low energy electrons into account. Before adding this modification to the code, using realistic values of secondary electron yields, the electron current failed to build up for a power level where multipacting was experimentally observed. After modifying the yield to the formula given above, the electron current grows, as would be expected from a multipactor avalanche. I believe that this is due to not losing as many electrons in the reverse RF field phases, as low energy electrons would tend to bounce off the surface until the field reverses. It was verified, by measuring the simulated electron charge in a small volume in the centre of the waveguide that the observed increase in electron current was not limited to the vicinity of the walls and was therefore a real increase in the overall multipacting current.

Saturation has been observed in a long simulation run where the space charge built up to such a level that the charge of sheets of electrons became greater than the electric field, causing the sheets to repel each other and causing the electrons to exhibit one point multipacting behaviour on the waveguide broad walls. Such a simulation is however unlikely to represent what would happen in reality, as well before the current levels exhibited in the simulation (kilo Amperes of current), the gas released by the surface would lead to a low pressure gas discharge. Attempting to model this would be a logical next step of the simulation process, as the MAGIC code incorporates the possibility of studying neutral gas ionisation. The difficulty resides in the great number of particles necessary to create a physically correct model.

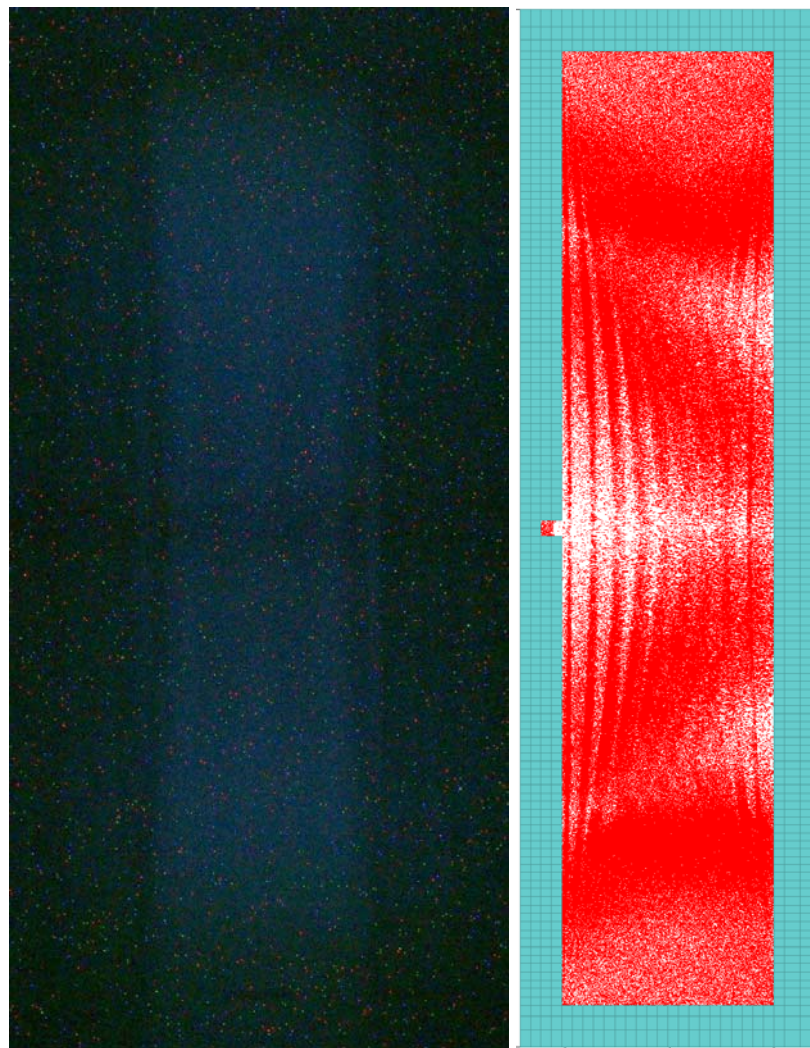


*Figure 22: Photograph of breakdown in a slotted waveguide (left) and simulation of a slotted waveguide using MAGIC (right). The picture from the simulation shows the position of the macro-particles (electrons) 200ns after the start of the simulation.*

An example of a simulation is shown in Figure 22 with a picture of a multipactor-induced gaseous discharge taken during the experiments seen in the same conditions as a MAGIC simulation. It can be expected that the areas showing the brightest glow are the areas having the highest density of energetic electrons; the resemblance between the two cases gives confidence that the results from the code are realistic. What is also apparent is the darker area between the broad walls of the waveguide, corresponding to the area where electrons are captured by the groove. The vertical bands visible on the simulation are not visible on the photograph because of the long exposure time (~3s).

### **3.5.1.2 Effect of the low energy electron component on the multipactor build-up**

A parameter scan on the height and width of the refracted low energy electron component was conducted using a simple rectangular geometry. Varying the fraction of backscattered electrons from 0 to 1 was found to have no effect on the total accumulated electron current accumulated on the walls of the waveguide in a given time ( $\delta_{max}$  set to 1.2 and 1.9), unless the ratio was set to 1. This signifies that given conditions favourable to multipactor, multipactor will develop whatever the fraction of low energy electrons. The fact that the total current only increases when the low energy backscatter fraction is set to 1 means that it only affects electrons who are pushed by the RF against a wall repeatedly ( $x^n = 0$  for  $0 \leq x < 1$ ). This would explain a widening of the multipacting bands by increasing the phase range from which multipacting electrons can be emitted.

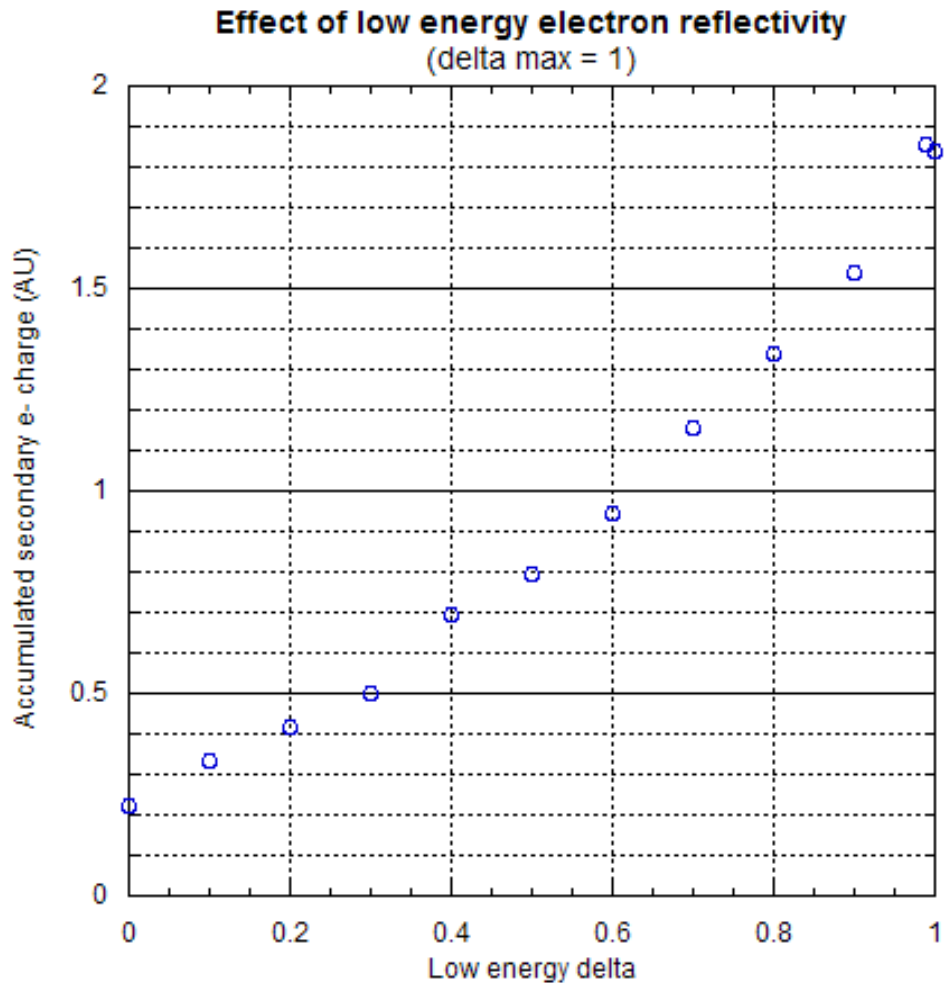


Figure 23: Accumulated secondary electron charge on waveguide walls with  $\delta_{max} = 1$  and varying values of  $\delta_{low\ energy}$  (low energy band from 0 to 5eV).

Figure 23 nevertheless shows that once the maximum yield of the surfaces becomes low enough ( $\delta_{max} = 1$  in the figure shown above), the electron charge accumulated on the waveguide walls changes with different backscattering ratios. This suggests that when multipactor nears saturation, the low energy electron backscattering may take a more important role than during the initial multipactor build-up.

### 3.5.2 Simulation of a coaxial waveguide

To further validate the MAGIC multipactor simulation, it was applied to a geometry studied in depth both numerically and experimentally. The coaxial geometry used as an example is a 50Ω coaxial line with an outer diameter of 40mm at a frequency of 1.3GHz. Pasi Ylä-Oijala has previously carried out simulations on such a line [35, 39], using the code MultiPac.

Figure 24 shows results from the Multipac code, given as the relative counter function (a measure of the stability of electron trajectories) as a function of the forward power in the coaxial waveguide. Also marked on the graph are the orders of the multipactor bands predicted by the code.

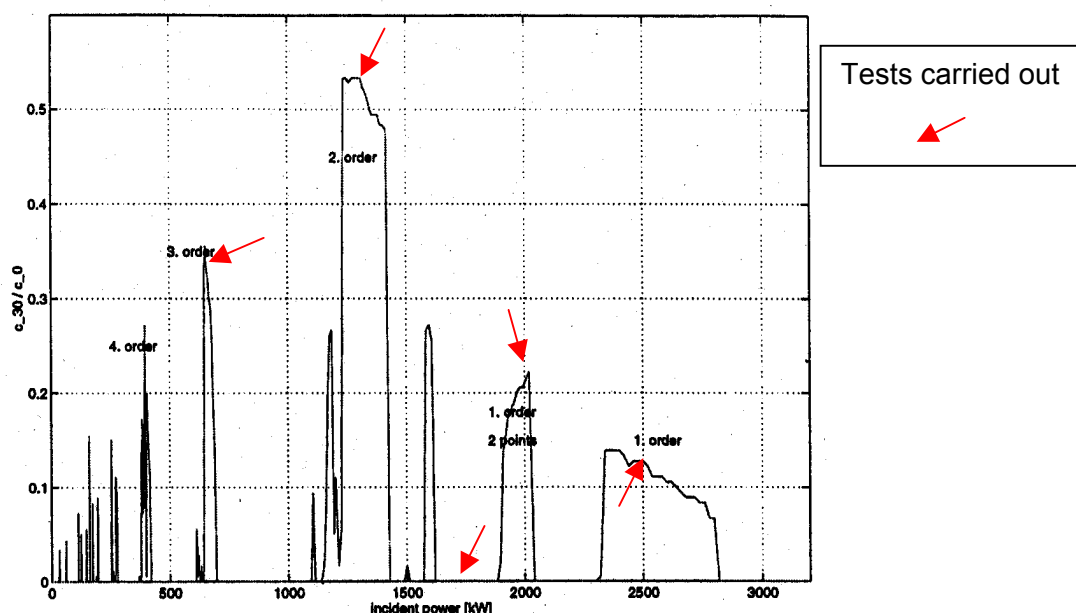
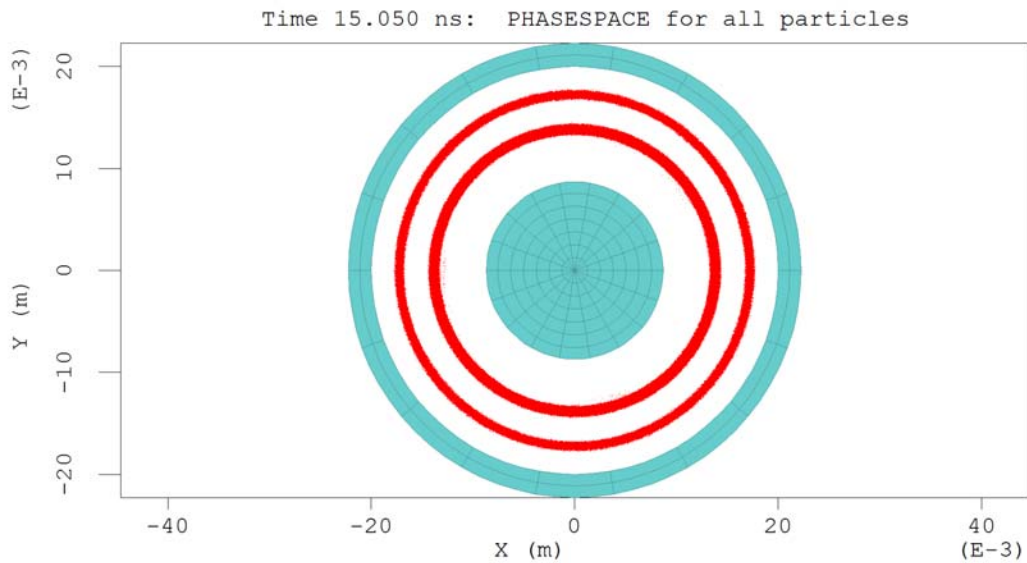


Figure 24: Results from MultiPac (from [39]) and markers showing simulations carried out in MAGIC. MultiPac simulation shows the relative counter function after 30 impacts. The simulated waveguide is a 1.3MHz, 50Ω coaxial line of 40mm outer diameter.

The MAGIC code was set-up in such a way that electrons were emitted from both inner and outer conductors. As was observed previously by P. Ylä-Oijala, both sets of electrons converged towards similar trajectories (generally one point multipacting on the outer conductor). Several cases mentioned in the TESLA Report were modelled using MAGIC, including cases with a DC bias voltage. In every case, the results were consistent with the MultiPac results (multipactor build-up was measurable in the form of accumulated charge on the waveguide walls, and the order of multipactor was determined from the visual aspect of the simulations). The presence (and absence) of multipactor was verified for RF powers of 1300kW (2<sup>nd</sup> order, 1 point multipactor on the outer wall), 2MW (1<sup>st</sup> order, 2 point multipactor), 2.5MW (1<sup>st</sup> order, 1 point multipactor on the outer wall) and 1.75MW (no multipactor build-up). P. Ylä-Oijala's results are shown in Figure 24.



*Figure 25: Status of the simulation with a power of 1.3MW 15ns after its beginning, showing both groups of electrons.*

Also verified were cases with a DC bias between the inner and outer wall. Once again, the results were consistent with the MultiPac results. A bias of 1kV was found to be insufficient to halt the multipactor, while 5kV achieved suppression for a power level of 1.3MW.

The code was also used to simulate the effect of a longitudinal magnetic bias in coaxial waveguide geometries. The results were encouraging and for a forward RF power of 1.3MW in the geometry given above, a field of at least 115G was necessary to achieve suppression.

### **3.5.3 Results from the MAGIC code**

The MAGIC code can produce a number of usable outputs. Most of them are only significant qualitatively, as the simulation cannot model completely realistic multipactor, particularly in the latter stages of a multipactor discharge where the influence of desorbed gases becomes significant.

The graphs showing secondary electron current or accumulated secondary electron charge on the waveguide walls, as a function of time, can provide an indication of the sustainability and build-up rate of multipactor in given conditions.

The phasespace plots can allow the determination of the order and number of impact points of multipactor; this was notably used to check MAGIC's trustworthiness as discussed in the previous section.

Placing measurement areas other than the entire waveguide can help locate the areas where the most multipactor current builds up. This is done in Figure 72 (page 92) to measure electron current off areas corresponding to the real-life electron probes that were used experimentally (discussed in further sections).

The code does not allow the simulation of a steady state of multipactor, as no counter-acting effect (most notably electron-stimulated desorption) can be implemented in the code, at least without significantly affecting the simulation time (typically 2-3 hours for a rectangular waveguide geometry with a good mesh density, more (8-10h) if small details need to be meshed appropriately (such as grooves or ridges on the waveguide surface)).

It is for that reason that it is very difficult to extract quantitative information out of the code, as most measurements from an experimental system rely on attaining a steady state of multipactor. As such, the best that can be expected is to measure onset points of multipactor if comparison with a real system can be used (this is done in the case of the study of the onset power of multipactor summarised in Figure 57 (page 75)).

## 4 Experimental method

Three visits to Cornell University in July 2001, January to March 2002 and October-November 2003 have led to many interesting observations and insights. The second and third visits, in particular, gave some very instructive first hand experience of the multipactor phenomenon. The motivation for the experiments that took place during those visits was both to experimentally verify the results from earlier multipactor simulations carried out with the Xing code and to confirm the effectiveness of multipactor cures that were derived from the results of the code and CESR operational experience.

### 4.1 Experiment description

#### 4.1.1 RF waveguides

##### 4.1.1.1 Multipacting Waveguide 1

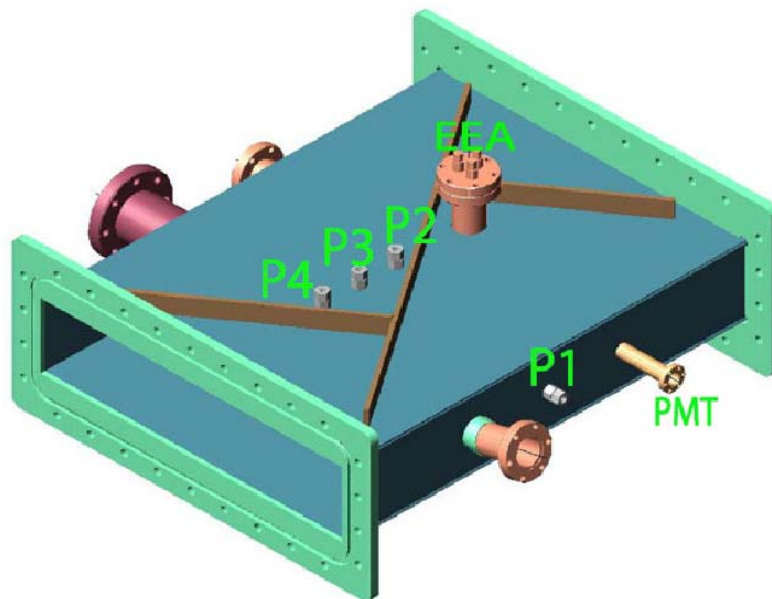
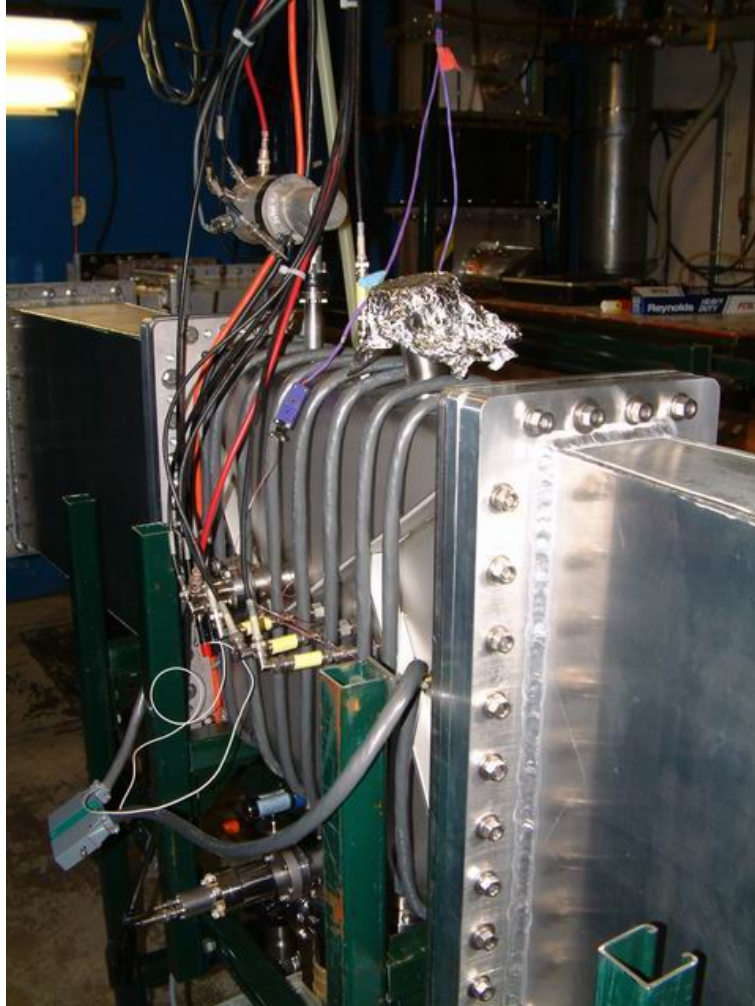


Figure 26: Multipacting waveguide

The first waveguide was a two-foot long stainless steel section of half height waveguide (18 inches by 4 inches, or 0.433m by 0.102m section), designed by Rongli Geng from Cornell University. The waveguide was fitted with a view port, an electron pickup port (P1) and a photomultiplier (PMT) port on a sidewall. The middle of a broad wall had three

extra electron pick-up probes (P2, P3, P4) as well as an energy analyser (EEA). The opposite sidewall was fitted with two ports for pumping, one of which led to a turbo pump, the other to a cold cathode gauge and an external pump out box. More detail on the diagnostics is available in Section 4.3.



*Figure 27: Experimental waveguide section (WG1)*

Vacuum insulation was insured by two 10mill (0.254 millimetre) Mylar films placed at either end of the waveguide, held between the flanges. These films allowed a vacuum quality of up to  $5 \cdot 10^{-6}$  torr with a 50L/s turbo-pump maintaining the vacuum. The Mylar films are also nearly transparent to RF power (attenuation factor  $\alpha_d = 0.014\text{m}^{-1}$ ). Kapton films (3 mill) had previously been used in the CESR cryostat at power levels of up to 260kW to maintain a dry nitrogen barrier before the windows. One question was whether the windows could take both the heat and the pressure.

The waveguide suffered from several defects, some of which were only noticed quite late. The bracing being insufficient, the waveguide warped during vacuum leak tests and was deformed whenever it was put under vacuum. This has the effect of bringing the broad walls together, changing the multipacting and field conditions inside the guide from the theoretical case. The inflection was measured to be of .375" in the centre of the guide (3.625" waveguide gap), a not inconsiderable change over the theoretical 4" interior dimension.

The second defect became apparent when it was noticed that welding had warped the half-inch thick flanges, opening a small gap in the flange walls when connected to the tapers (described in Section 4.2) for the experiment. The effects of this gap were more important than originally imagined and led to a week's delay in the project. The flanges were later re-faced and the O-ring grooves re-cut by the machine shop in order to close the gap and prevent RF leakage (more detail is given in Section 5.1.2.2).

#### 4.1.2 Grooved waveguide (Waveguide 2)

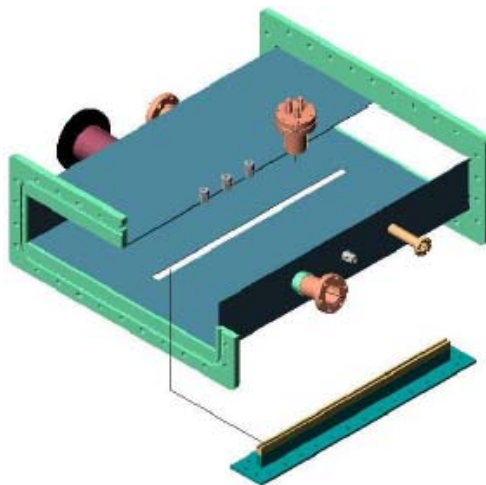


Figure 28: Grooved waveguide section (WG2)

The second waveguide was also designed by Rongli Geng. It was identical to the first except for a slot (described in more detail in Section 6.1.2) cut along the centre line of one broad wall. This allowed the fitting of different inserts to study the effect of groove profiles. The waveguide suffered from the same defects as the previous one, in that the insufficient bracing led to an even more marked deformation (the groove weakening the wall on either side of the centre line). The welding had also warped the flanges as in the

first waveguide. Corrective action was taken in the light of the experiences with the first waveguide, both in re-cutting the flange ends and adding additional bracing to the waveguide broad walls, but the deflection remained quite important despite the additional bracing.

The grooved section allowed bars of various metals to be inserted into the waveguide at variable depths. A Viton o-ring laid around the flange insured the vacuum seal. The bars tested were either copper or aluminium, and were themselves flat (to act like a normal un-slotted waveguide) or grooved.

### **4.1.3 Waveguide 3**

#### **4.1.3.1 Waveguide design**

##### *4.1.3.1.1 Design requirements*

The first series of experiments were designed to replicate the conditions in the CESR coupler as closely as possible, but unfortunately failed in certain respects.

- One major issue was that the waveguide walls were insufficiently braced to withstand vacuum pressure, leading to bowing which modified the height of the waveguide from the planned 4" to a measured 3.63" height in the worst case. This was suspected to have introduced a spread of multipacting conditions leading to the observed widening of the multipacting bands. Observing those bands in a waveguide whose dimensions were well controlled might have altered our conclusions after the first series of experiments. A structurally solid waveguide would also provide a reliable benchmark for simulations.
- A method of multipactor reduction is to alter the secondary electron yield of the surfaces. This can be achieved by applying a coating of a material with a low secondary electron yield, or by modifying the geometry in such a way that the secondary electrons are trapped. In order to study different kinds of coatings and surface treatments, it is helpful to be able to easily change the multipacting surfaces. Surfaces that could be tested include simple stainless steel or copper surfaces that are used in many couplers, as well as TiN or non-evaporable getter (NEG) coated surfaces.

- An aspect of the CESR coupler that was not covered by the previous experiments was that they did not allow for any cooling of the waveguide, whereas in the real coupler, the temperature goes from 4K at the Nb coupler and E-plane bend, to room temperature near the RF window. A study of the effect of condensed gases on the surface would help establish the effectiveness of using coatings or other similar methods of secondary electron yield reduction in a cryogenically cooled environment.
- A possible extension of the groove concept is to try several narrow, relatively shallow grooves along the centre of the waveguide centre-line. This should allow the suppression of multipacting electrons on a greater width than a single groove could provide.

Given these requirements, the waveguide design called for a solidly built waveguide allowing the possibility of changing a significant area of the surface on at least one broad wall of the waveguide. Additionally, it should incorporate the possibility of cooling the waveguide on at least one wall. Cooling down to LHe temperatures would be ideal, but would unfortunately involve significant additional difficulties and expense. It is therefore much more practical to envisage a design cooled by LN<sub>2</sub>. This would allow fewer species of gas to condense on the surfaces (as seen in Figure 29), but would still be able to replicate the behaviour of the double E-bend region of the CESR input coupler. This new waveguide was dubbed WG3.

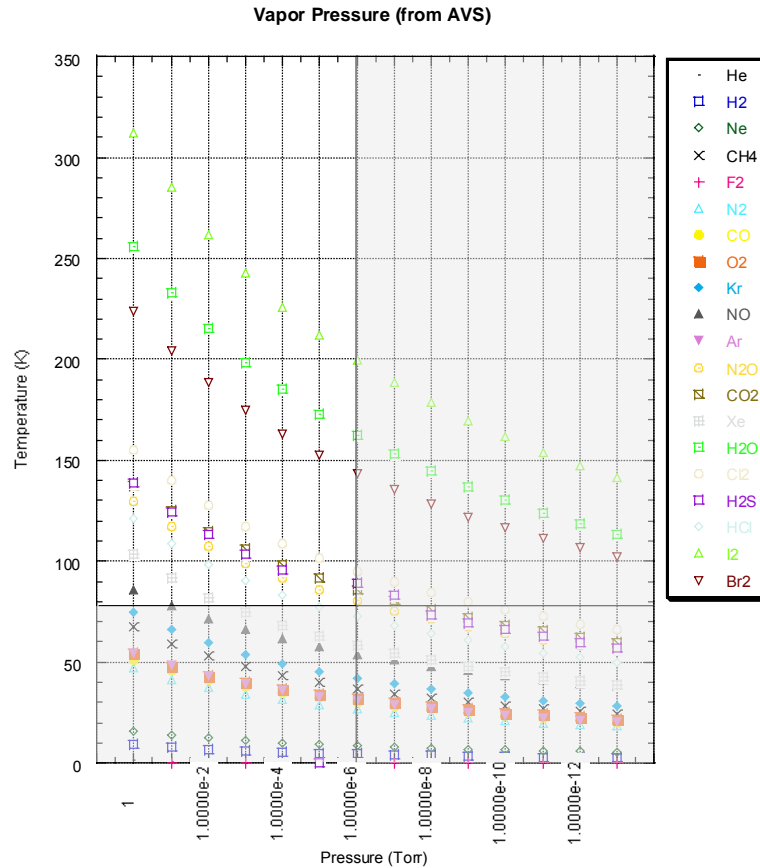


Figure 29: Vapour pressure of various gases. With WG3 temperatures and pressures, we can only expect to condensed gases as shown in the top left quadrant.

Several possibilities were studied, including putting the wall in contact with a bath of liquid nitrogen. It was decided that having a cooling channel running through a ‘cooling’ plate in the waveguide was the most practical solution as it provided good thermal insulation of the sample plate. LN<sub>2</sub> is also easily available and inexpensive, so it would simply be allowed to evaporate at the other end of the pipe.

The possibility of adding heating tapes to the cooling plate was also incorporated, so as to enable the heating of the surface in order to:

- clean it as would be required for adequate studies of coatings;
- activate getter materials (temperatures in the order of 180°-200°C over a period in the order of an hour are required for such purposes).

It was also possible during the previous experiments to take pictures of the glow through the Mylar windows that insured the vacuum integrity of the system. This facility was also conserved. Mylar windows were the only realistic solution regarding the vacuum system,

despite their limitations as a vacuum windows. The other option might have been to re-use old beryllium windows that were initially planned for use on CESR. They however never performed up to the required standard, and would have required heavy processing to be used for the waveguide experiment. The other stopping point was the toxicity of beryllium, which would have at the least imposed the introduction of major safety provisions to deal with the risks of window breakage.

The design chosen for the sample plate support was a large, rectangular sample plate filling up as much width of the waveguide as was reasonably possible and a length exceeding half a guided wavelength ( $\lambda_g=79.4\text{cm}$  for this waveguide). It later became apparent that coatings could not be applied to such a large surface due to the limited size of coating set-ups. A large sample plate with a circular insert of 15cm diameter was built to allow the coating of smaller sample plates.

#### 4.1.3.1.2 Design characteristics

Waveguide cross-section	18" by 4" (457.2mm by 101.6mm)
Waveguide length	Approx. 1080mm
Waveguide cooling mechanism	Flow of LN <sub>2</sub> (77K minimum temperature reachable)
Waveguide heating mechanisms	Heater tape groove in the 'cooling' plate, possibility of blowing hot air through the LN <sub>2</sub> channel
Vacuum isolation method	2 Mylar films (.1mm thick) at either end
Expected waveguide vacuum pressure	10 <sup>-6</sup> Torr at best (from previous experience) (best actual pressure at room temperature ~5.10 <sup>-4</sup> Torr)
Planned diagnostics	1 EEA, 8 electron pickup probes, 2 thermocouples on one sample plate 2 thermocouples on opposite sample plate 1 EEA, 1 viewport, 1 photodiode, 1 extra conflat flange on a sidewall Viewports on the bends outside the waveguide looking in
Max RF power from klystron	600kW pulsed
Max. RF power handling capability (estimated from experience)	300 kW CW, or equivalent average power in pulsed mode, limited by the Mylar windows

Figure 30: Basic waveguide characteristics

The waveguide interior is designed to present an 18" by 4" cross-section equal to that of the CESR input coupler. It is quite long, measuring 1.08m from flange to flange. This length is such that the sample plate could be long enough. The additional length presents the advantage that the effect of the Mylar windows is diminished in the vicinity of the diagnostic probes.

One waveguide sidewall is fitted with four 3.5" Conflat flanges that hold:

- An electron energy analyser (EEA), which is a Faraday cup fitted with a retarding grid. This probe (pictured in Figure 45) will be described in more detail in Section 4.3.
- A photodiode to detect light emission triggered by the discharge accompanying vacuum breakdown.
- A view-port looking at a broad wall, allowing better observation of the multipactor. It also allows us to verify the absence of arcing or other activity that would interfere with multipactor measurements.
- A spare flange, for use with other instruments that can include, depending on availability, a residual gas analyser (none was available for our experiments, however).

It was initially planned that the waveguide should have two changeable plates, one of which would have been drilled with the various holes required for the electron probes and Faraday cup. Budgetary constraints have, however, forced a number of simplifications on the waveguide. The first was to do away with one of the removable sample plates and simply put the probes in the waveguide wall. The effect of this is that rather than having an absolute measurement of multipactor behaviour in the waveguide, one now only has an idea of the trend that various surface conditions have on multipactor due to one surface being stainless steel in all configurations.

The removable sample plate uses up as much of the width of the broad walls as technically possible, and is long enough to ensure that most electrons collected by the EEA and the probes come from a portion of the sample material. This provides a reasonable degree of confidence concerning the origin of the measured electrons during any study.

The wall opposite the sample plate was fitted with a total of eight electron pickup probes and another EEA. The electron probes are arranged in the pattern of a cross in order to be able to localise the areas of maximum electron current. This should help measure the transverse spread of multipactor and verify predictions that multipactor occurs mainly in the centre of the waveguide. The distribution of probes along the waveguide axis is there to confirm that multipactor currents are identical along that axis in travelling wave (TW) mode. Two thermocouples will be fitted just behind the sample plates to measure its temperature. The sample plate will now only have thermocouples monitoring the temperature, since the electron probes were relocated to the waveguide wall opposite the remaining sample plate. Their configuration is still the same cross figure as they had on the plate.

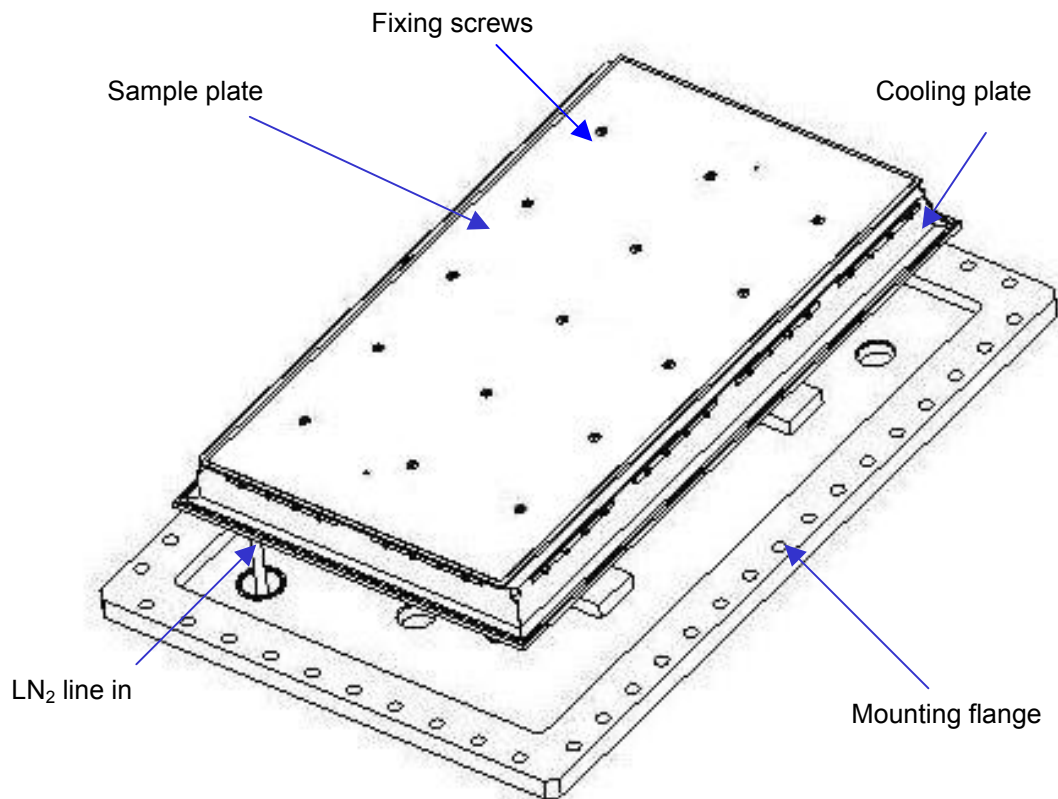


*Figure 31: View of the initially planned sample plate mounted on the flange. No electron probes or EEAs remain in the real sample plate.*

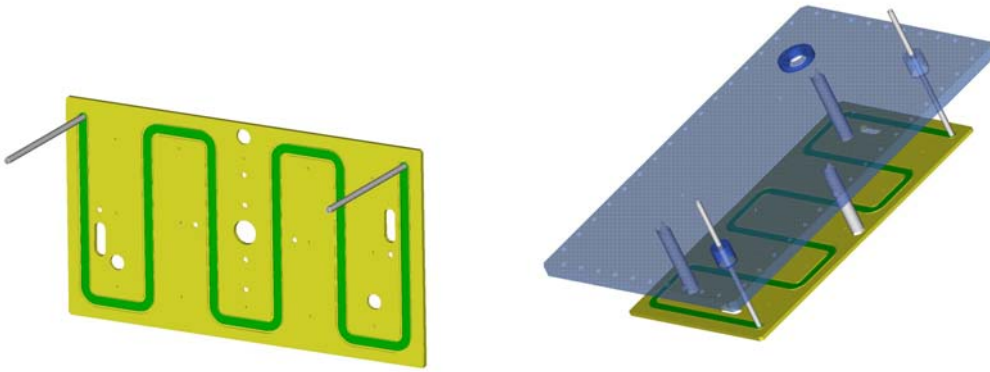


*Figure 32: View of the cooling channels on the cooling plate. Also visible are the holes (that were planned but not implemented) for the electron probes and EEA as well as the holes for the thermocouple wires. The second view shows the mounting of the cooling plate on the flange plate.*

The sample plates are cooled by a line of LN<sub>2</sub> running through the support plate. The test sample plates are quite simply thin (~3mm) plates of whichever material is to be studied, cut to the appropriate dimensions, with drilled holes for fixation to the cooling plate. These plates are thus of simple manufacture, and therefore relatively inexpensive to produce.

The cooling plate was stood off from the flange, held by 3 posts to minimise conduction losses while still being mechanically strong. The section of the waveguide behind the sample plates was also under vacuum, so there was no pressure-induced distortion of the waveguide walls. Two pipes connected to the main waveguide body assisted the pumping of those spaces. RF leakage into them was limited by having spring fingers insuring good electrical contact between the waveguide walls and the sample plate support. It was expected to be possible to safely absorb any RF still leaking through with some RF-absorbant material fixed onto the cooling plate (no excess RF was detected in the experiments).

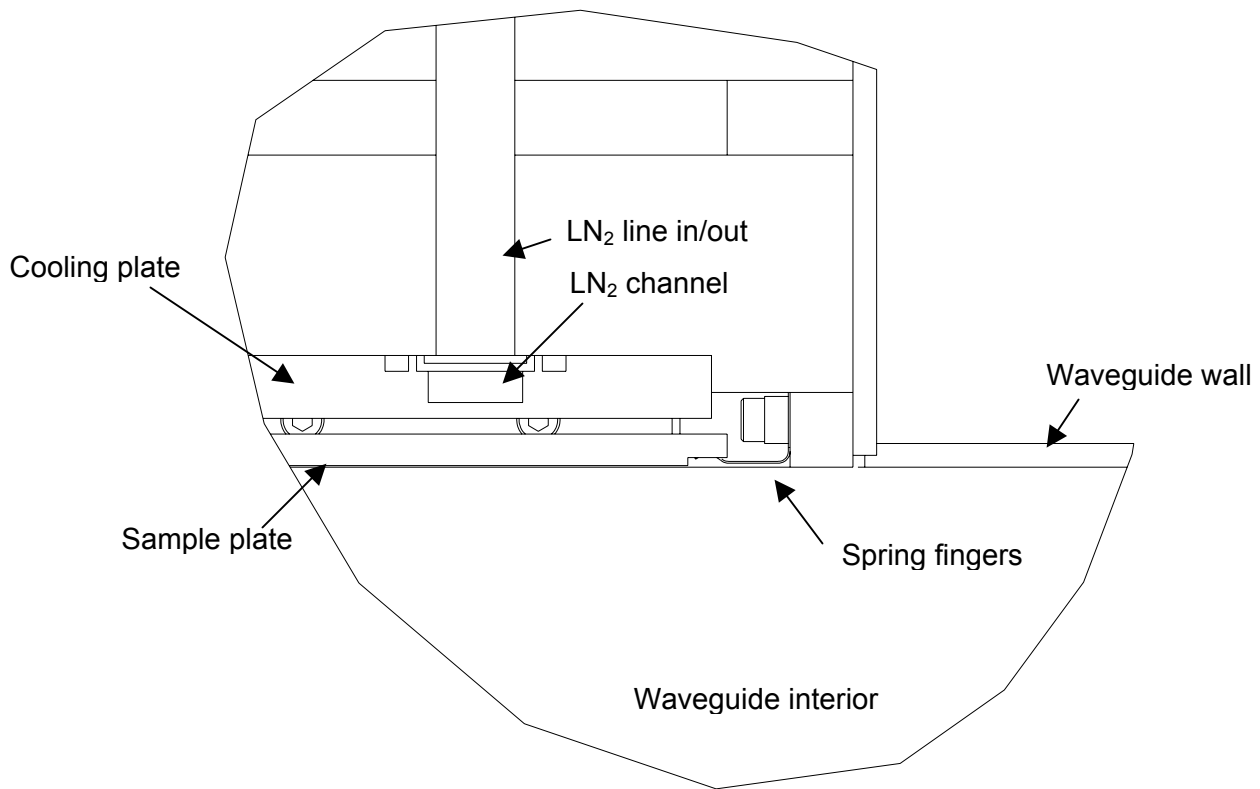


Figure 33: Detail of the sample plate fixation and RF contact with the waveguide walls



Figure 34: Picture of the waveguide being prepared in the workshop

Figure 33 shows the detail of the spring finger contact between the waveguide body and the sample plate. The sample plate is shown to be separated from the cooling plate by a small (~1mm) gap that is bridged by small blocks from the cooling plate ensuring good contact near the screw fixation points (these islands are visible on Figure 40 on page 58).

#### **4.1.3.2 *Experimental site***

The location of the experiment was mainly decided by practical considerations. Building the waveguide at Daresbury rather than at Cornell simplified the process and provided valuable experience. The location of the experiment depended on the availability of resources (high power RF, technical support etc.). A factor in favour of conducting the experiment at Daresbury would have been the learning experience for all involved while Cornell on the other hand had very experienced personnel and proven hardware resources. The unavailability of high power RF at Daresbury within reasonable timescales forced the choice of Cornell as the experimental venue.

#### **4.1.3.3 *Experimental programme***

The experiments were designed to take approximately a month of running time. The actual time taken was five weeks, due in part to the delayed arrival of the waveguide and a coaxial cable failure that required the repetition of several measurements. Tests conducted included:

- Testing the copper sample plate served as a baseline for all other experiments and allowed comparison with the real waveguide set-up. It was also be used for the set-up and verification of the waveguide. It also allowed experiments such as measuring electron energies at various power levels (compared with results from WG1 and 2), testing the effect of an electric field bias and studying the effect of condensed gases on multipactor behaviour, by comparing the frequency and RF power levels of trips depending on vacuum conditions, surface temperatures, etc.
- An aluminium plate allowed the testing of a different type of metal. Though the secondary electron yield of clean aluminium is very similar to the yield of most metals, aluminium easily forms an oxide layer that has a high SEY. It also provided a basic material for comparison (though we ran into problems with the Al plate, detailed on page 70).
- A stainless steel plate allowed the testing of another type of metal. The secondary electron yield of clean stainless steel is slightly lower than the yield of other metals. It also provided a basic material for comparison.

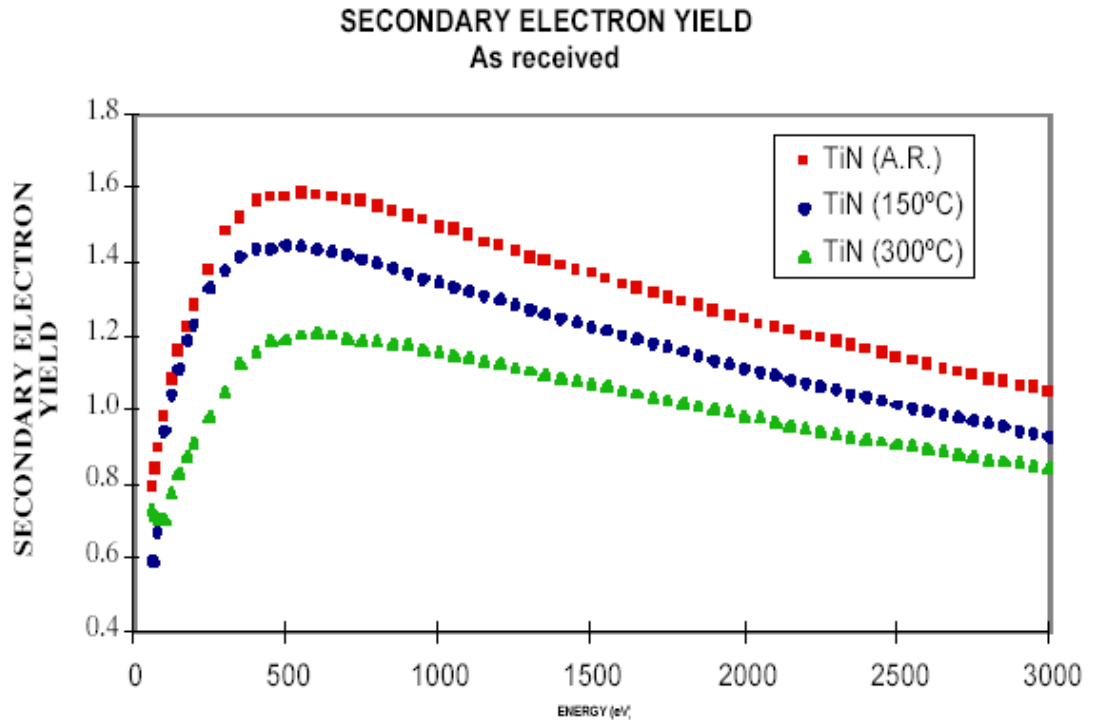


Figure 35: Secondary electron yield of TiN coated surfaces [25]

- A TiN coated plate evaluated the effectiveness of using such coatings to reduce or inhibit multipactor in vacuum waveguides. Despite the low conductivity of TiN (resistivity (TiN bulk material)  $> 1\text{M}\Omega\cdot\text{m}$  at room temperature, reduces to  $0.8\text{M}\Omega\cdot\text{m}$  at cryogenic temperatures), RF losses were not expected not be too important as the thickness of the coating was only of a few microns (similar to that of some RF windows which are much more demanding).
- Another coating that was interesting to study was a non-evaporable getter (NEG) coating. It had a low secondary electron yield, has the additional property of acting as a vacuum pump, and only needed a thin deposited layer (in the order of the micrometer). The drawback of NEG coating is that it needs to be baked to at least  $180^\circ\text{C}$  (TiZrV, for 24h) to be activated. In-situ activation was achieved using a combination of heating coils placed in the cooling plate and blowing hot air through the cooling plate channels.

## SECONDARY ELECTRON YIELD OF A GETTER LAYER **TI ZR V**

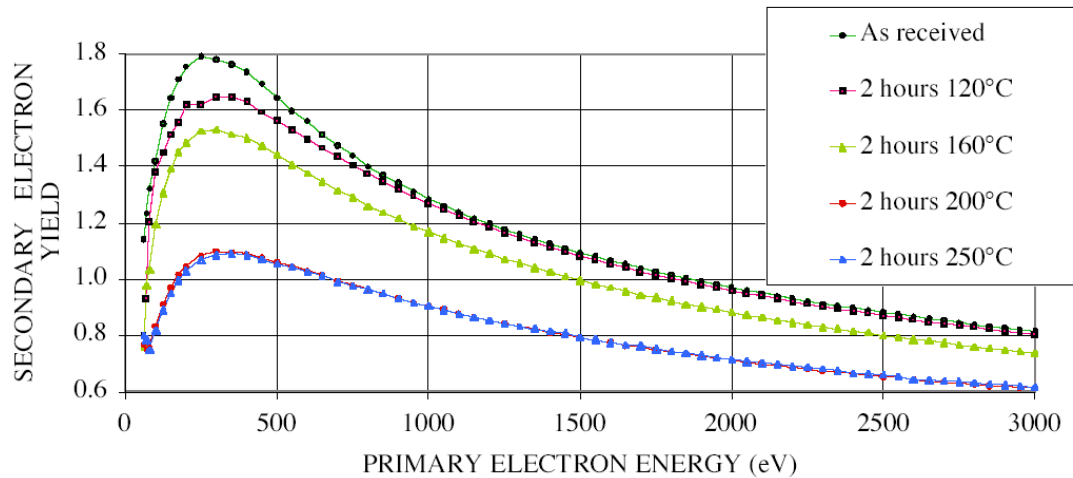


Figure 36: Secondary electron yield of a getter layer [25]

- To complement the study carried out in the WG2 experiment with the groove, several grooves were cut close to the centre-line into a Cu sample plate. These were expected to drastically reduce multipactor if the assumption that most multipacting electrons stay in the centre of the waveguide between the broad walls is correct. The sample plates were 4mm thick, so it was necessary to cut through the sample plate entirely to get grooves deep enough to have an effect.

### 4.2 Processing area set-up

The experiment took place in the RF processing area in the CESR main hall. This location is used for window tests and was used for vertical cavity tests as well until the processing area at Newman Laboratory became available.

The multipacting waveguide section is fitted between two tapers from full-height WR1800 (9 inches) to half-height (4 inches). The upstream section leads to the klystron, the downstream to a 300kW water load. The test section is placed between two bends so that the experiment can be observed through view-ports placed at either end.

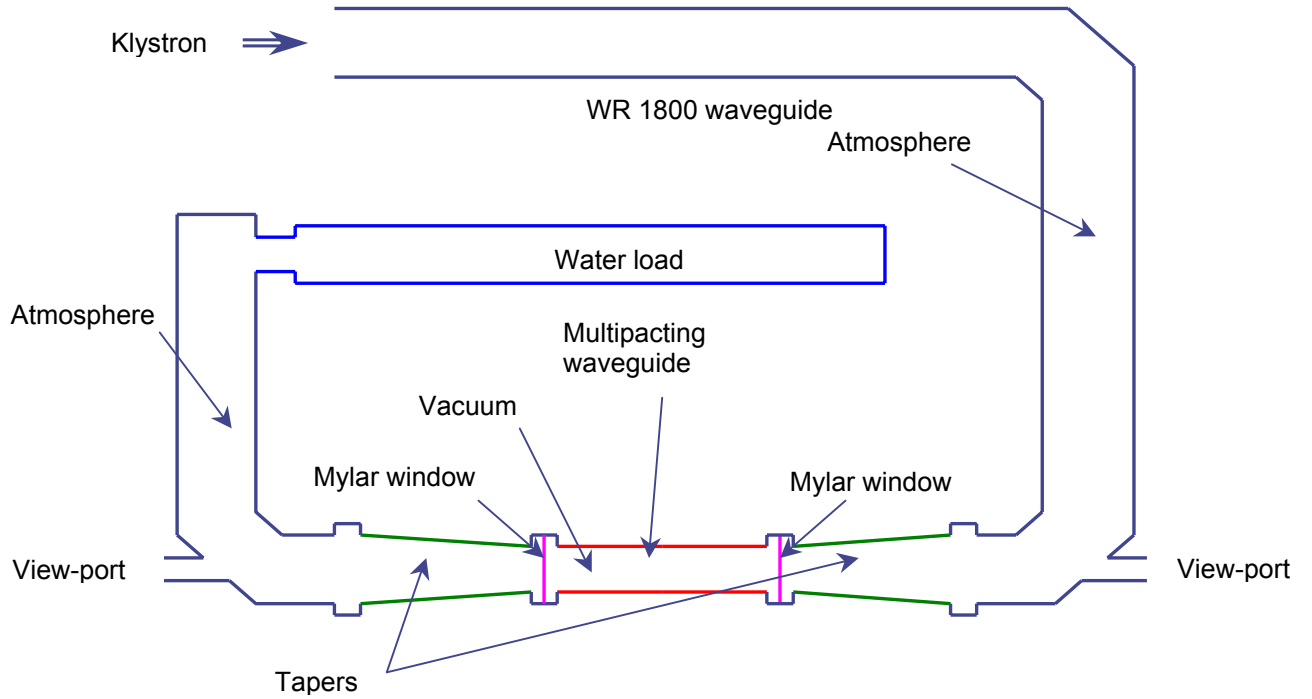


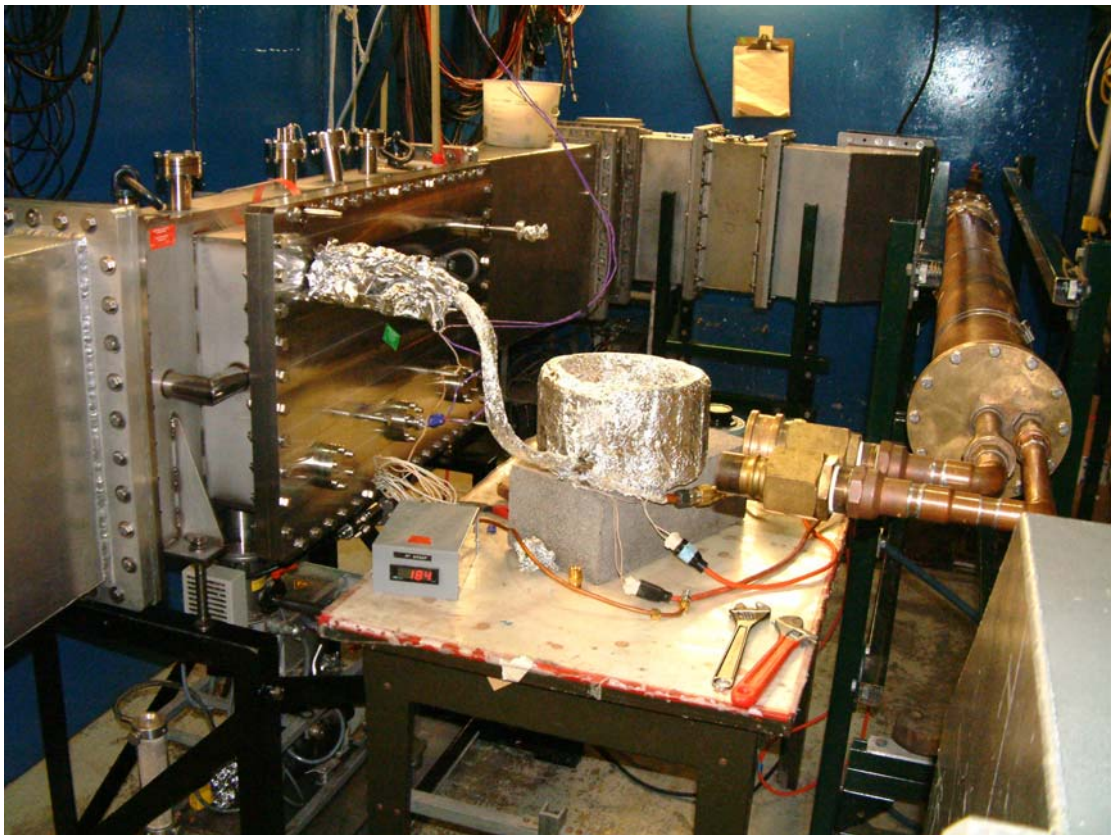
Figure 37: Layout of the experimental set-up in the processing area at Cornell



Figure 38: View of the processing area

The controls for the experiment were located on the other side of the shielding wall seen in the background of Figure 38. There, among other things, the klystron power can be set and the diagnostics read.

WG3 could be heated using a combination of hot air blown through the cooling channel and a heater wire that was fixed to the sample plate's side of the cooling plate (see Figure 40). The heating tapes were wrapped around a coiled air tube through which N<sub>2</sub> gas (initially at room temperature) was blown. The air temperature was eventually (after some trial and error) raised above 400C. By adjusting the air flow, the sample plate could eventually be brought to temperatures around 200C.



*Figure 39: Heater coil connected to the waveguide blowing hot air through the cooling plate channel.*



*Figure 40: Phil Barnes inspecting the heater wire clamped onto the sample plate support.*

### **4.3 Diagnostics**

The waveguide sections were fitted with as many diagnostics as possible. They were:

- 4 electron probes (for WG1/2), 3 on the middle line of the broad wall and one on a sidewall. They were initially connected to a multiplexer and to a 24V battery that provided an attracting potential to the electrons and increased the probes' efficiency as well as limiting secondary electron reemission from the probes (which might affect measurements). Current was measured by measuring the voltage on either pole of a resistor inserted in the circuit. Later on each probe was fitted to a separate battery for ease of measurement.

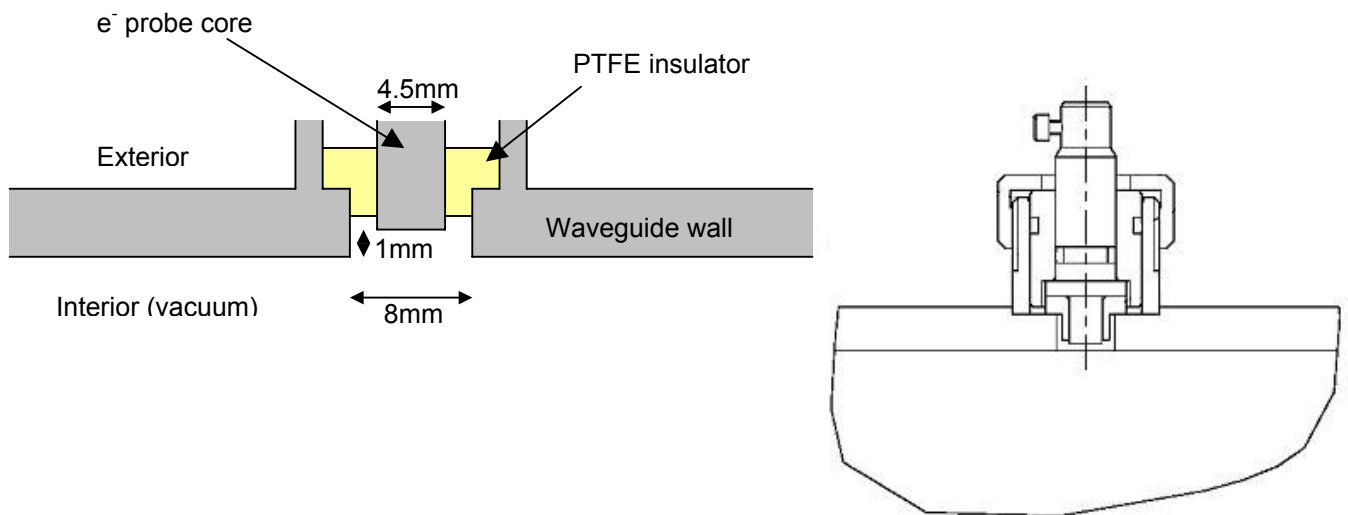


Figure 41: Electron probe schematic and engineering diagram (WG3)

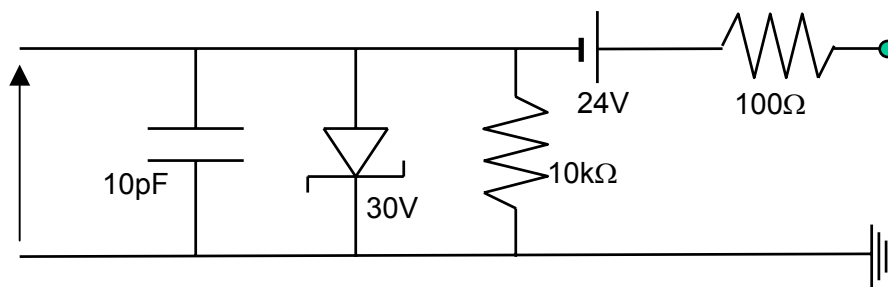


Figure 42: Circuit diagram for the electron probes used with WG3

- 8 electron probes positioned in a cross pattern on WG3. They allowed a better spatial resolution of the multipactor current, including some information about off axis multipactor currents. A picture of the set-up is shown on Figure 85 (page 107). It is also visible on Figure 44.



Figure 43: Electron probes and energy analyser (waveguides 1 and 2)

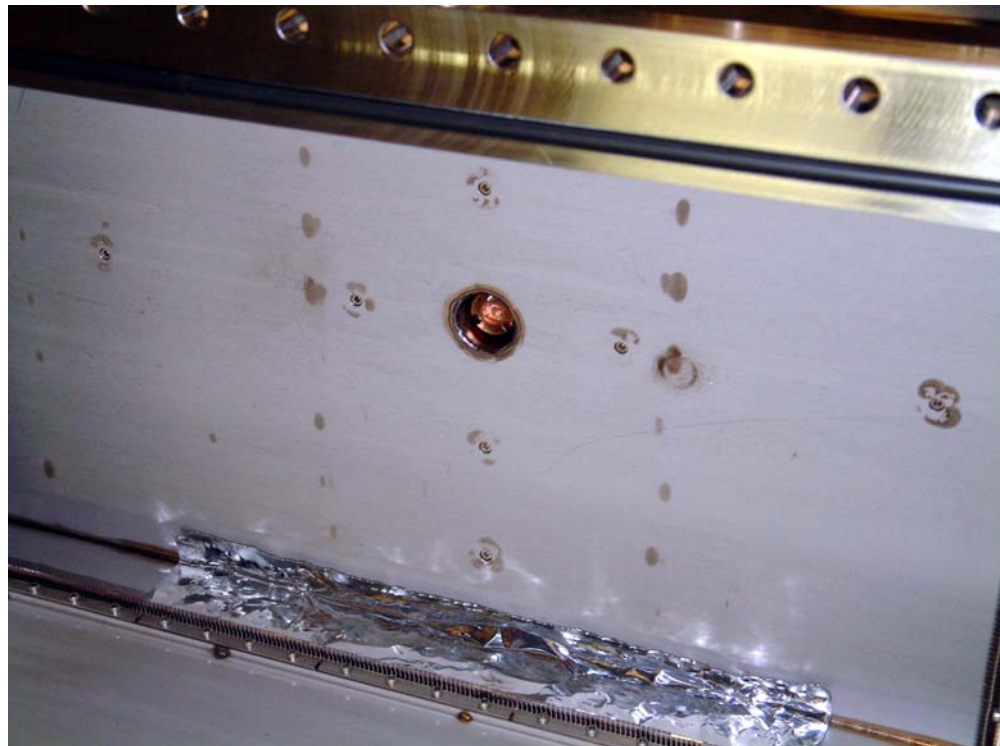


Figure 44: Picture of the inside wall of WG3 showing 7 out of 8 probes as well as EEA1.

- An electron energy analyser (EEA), which is very similar in concept to an electron probe, was located on the centre-line of WG1/2. It consists of a Faraday cup located behind a mesh that can be charged with a retarding potential to repulse low energy electrons. The cup was charged positively with a battery, as the electron probes were, to increase its efficiency. Electron energy could be measured by comparing the currents measured at various retarding potentials. The EEA is of a Rosenberg design [40] and built by RL Geng for the purpose of the experiments.

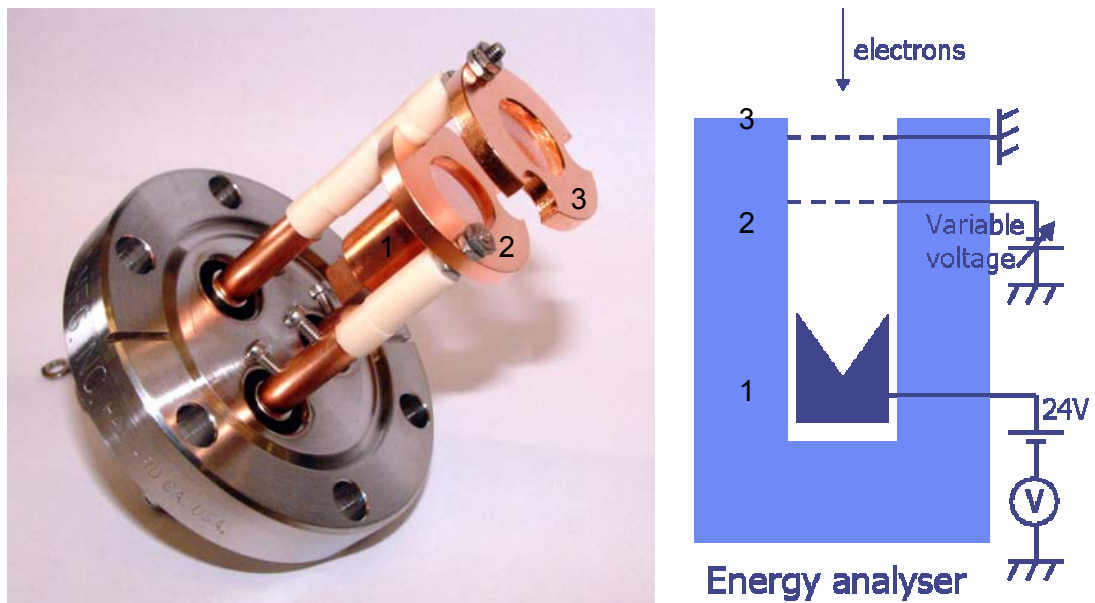


Figure 45: Picture and schematic of an electron energy analyser (the flange is a 2<sup>3/4</sup>" flange)

Two EEAs were placed in WG3, one in the centre of the broad wall (as can be seen in Figure 44 and Figure 85 (page 107)), the other on the sidewall.

- A photomultiplier tube (PMT) allowed the detection of events that produced light or soft X-rays (on waveguides 1 and 2). It could provide valuable information as to the nature of events in correlation with other diagnostics. The photomultiplier tube could also be used to protect the system by interlocking it with the klystron drive to shut down power if the average or peak light intensity exceeded preset levels. The initial levels were set pragmatically and were later reduced on due to excessive tripping. After a trip, the RF control system would recover automatically and power would return after three seconds.



Figure 46: Photomultiplier tube

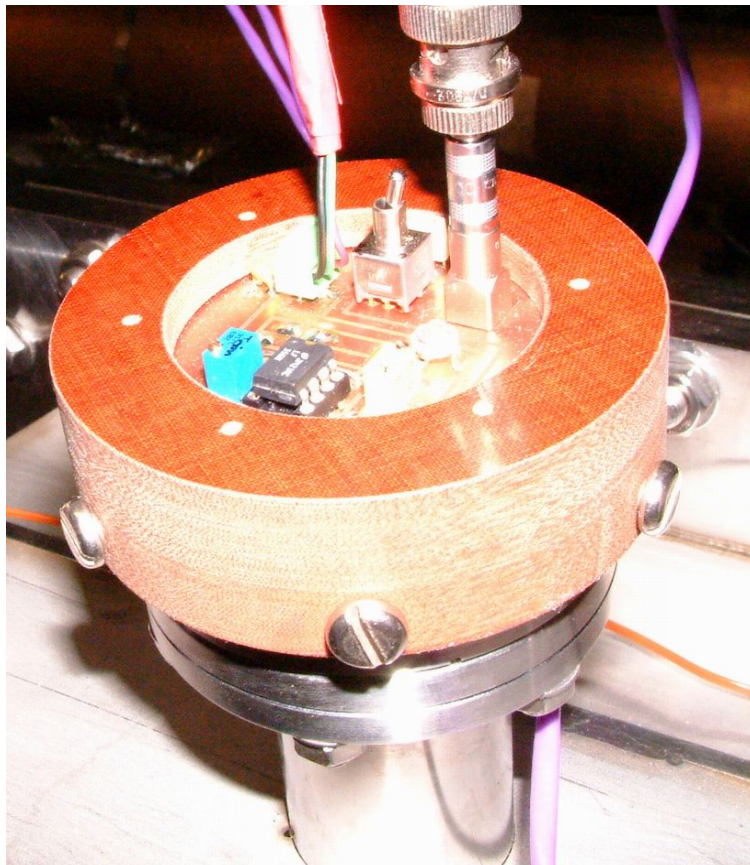


Figure 47: Photodiode on WG3

- A photodiode was used on WG3. It looked into the waveguide through a 2<sup>3/4</sup>" flange window. It had the same uses as the photomultiplier of WG1/2, but proved to be less successful due to an excessive time constant that smoothed out detail in the measurements.
- The three available view-ports (one on the waveguide sidewall, one on each elbow bend) also allowed the detection and capture (with a video camera) of any light. The fact that the windows were transparent was an unplanned advantage, as it allowed us to look into the waveguide during breakdown events, allowing both visual observation and the use of a digital camera.
- A vacuum pressure gauge was used to both protect the waveguide (through interlocks connected to a cold cathode gauge) and to detect the release of gas by either heating of the walls or flanges, or vacuum bursts due to breakdown. The gauges used were a convectron gauge (low vacuum range), and a cold cathode gauge for the higher vacuum levels.



Figure 48: Convectron gauge and pump-out ports on waveguides 1 and 2

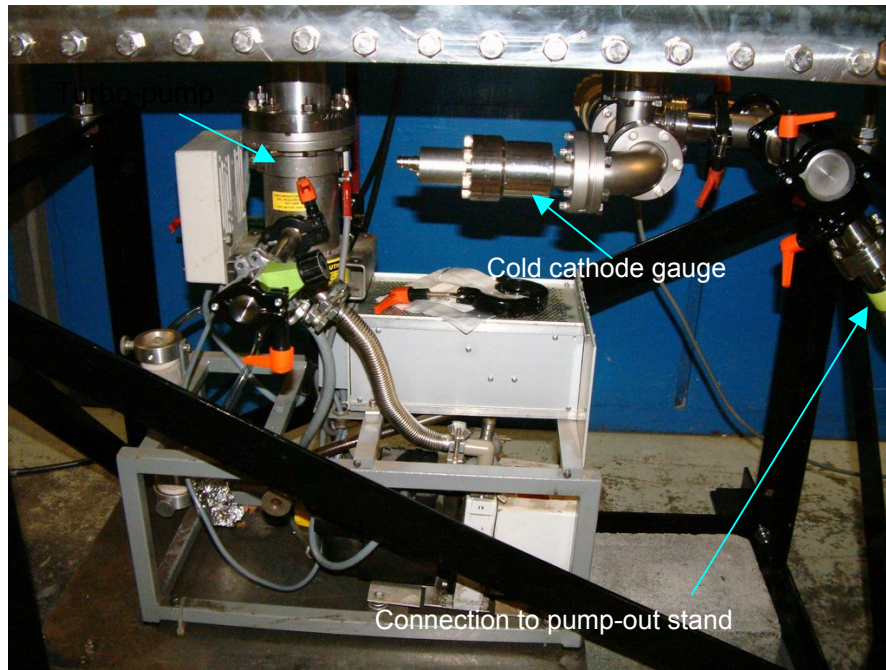


Figure 49: Pumping system on waveguide 3

- Type T thermocouples placed on the flanges and broad walls allowed the detection of any excessive heat accumulating in the system. As the Mylar windows were not designed to resist temperatures exceeding  $110^{\circ}\text{C}$ , keeping track of the temperature was important at high power levels. The usefulness of the thermocouples for the detection of multipactor was however limited as they measured the temperature of the mass of the wall and could not pick up the smaller variations one might expect the multipactor or breakdown to cause.

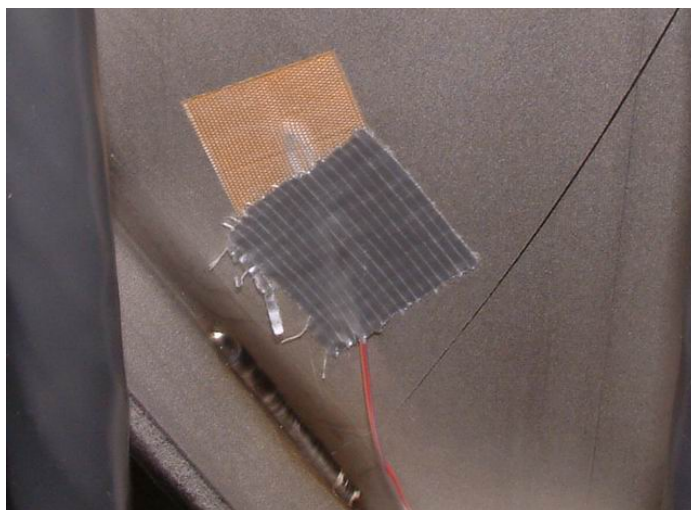


Figure 50: Type T thermocouple on the waveguide wall

In WG3, thermocouples were also placed on the backside of the waveguide sample plate. These thermocouples were used to monitor the temperature of the plate during heating and cooling experiments.

- Forward and reflected power levels could be read from the klystron control panel. This data was particularly relevant to pulse mode operation.

The available power was about 550kW in a short pulse (1-3% duty cycle) with a 10Hz repetition rate. The maximum power we used in CW mode was 300kW, which was the limit imposed by the windows (unfortunately, experimentally verified).

## **5 Experimental observations of multipactor**

### **5.1 Experiment set-up and issues**

#### **5.1.1 Introduction**

The first experiments were designed by R.L. Geng at Cornell to test the multipacting behaviour of the CESR cavity waveguides. To achieve this he designed and built two test waveguides (referred to as waveguides 1 and 2). I was invited to join in the experiments and actively participated in the experimental procedure and data analysis. Waveguide 3 was designed and tested by myself (with a lot of help from the Daresbury engineering group and workshop, as well as John Reilly, Phil Barnes and many more at Cornell University).

Unless otherwise stated, the experiments were run in pulsed mode (pulse length 2-3ms with a 10Hz repetition rate). This was to keep the average power low to avoid damaging the Mylar windows.

#### **5.1.2 Waveguide 1 and 2**

##### **5.1.2.1 Pre-experiment set-up**

Measurements of the magnetic field were carried out (using a hand-held gaussmeter) to evaluate the effect of the solenoid coil inside the waveguide. The coil was a multi-conductor cable, each of the conductors being connected in series by connecting the pins of a multi-way connector. The measurement found a very strong background magnetic field in the vicinity of the cold cathode gauge, which was reduced by adding shielding around the gauge. The measurements were only taken along  $B_z$  where the z-axis is the direction of the wave propagation. A background field of approximately 300mG was found, and the field produced by the coils was calibrated with the gauss-meter readings in the centre of the waveguide.

##### **5.1.2.2 Experimental issues**

The waveguide could reach pressures of up to  $2 \cdot 10^{-5}$ Torr after its first pump-down. Problems however arose when RF power was applied, as bad vacuum behaviour made

us realise that the o-ring was getting too warm due to the slight gap (~0.25mm) that allowed RF to leak through the flange to the joint. As we took the flanges apart we saw that the o-ring had been damaged quite seriously.



Figure 51: O-ring damage (detail)

The only solution to this was to close the gap as much as possible. Simulations carried out showed that RF leakage into the o-ring could not be totally avoided due to the Mylar film's inherent thickness. However, if the gap could be kept as narrow as possible, that leakage should remain small. A simple formula was found to stay very close to the results calculated by MAFIA ( $b$  = waveguide height,  $g$  = gap width). In terms of S-parameters, where ports 1 and 2 are the input and output ports of the waveguide and 3 is the leakage through the Mylar seal, the power flowing through the gap is:

$$S_{31}^2 = \frac{b}{b + g}$$

Gap width	1"	0.5"	0.1"	0.05"	0.01"
$S_{31}^2$ (MAFIA)	0.19	0.1	0.023	-	-
$S_{31}^2$ (theory)	0.2	0.11	0.024	0.012	0.0025

Considering a total power of 100kW, with a 0.01" thick Mylar film, the maximum power leak into the film would be 250W. If you consider that the  $\epsilon_r$  of the film is  $\epsilon_r = 3$ , the calculated result is divided by half for a total of 125W spread out onto all of the length of the o-ring, which was judged to be acceptable.

The waveguide was sent to the machine shop in order to flatten out the flange and recut the o-ring groove. A correct size o-ring was also used in order to minimise the risk. Water cooled plates were also clamped onto the flanges to help keep the o-ring cool. This had the effect of improving vacuum quality to the mid  $10^{-6}$ Torr range.

A not insignificant RF leakage was later detected (through the interaction it had with the main CESR ring) and a groove was added to the flange plates to allow the insertion of a metallic mesh preventing the RF from leaking out (see Figure 52 and Figure 53). The leakage involved did not pose any particular safety risk unless someone put a hand (or any other part of the body) in the immediate vicinity of the leak, while RF power was on, for a prolonged period of time.

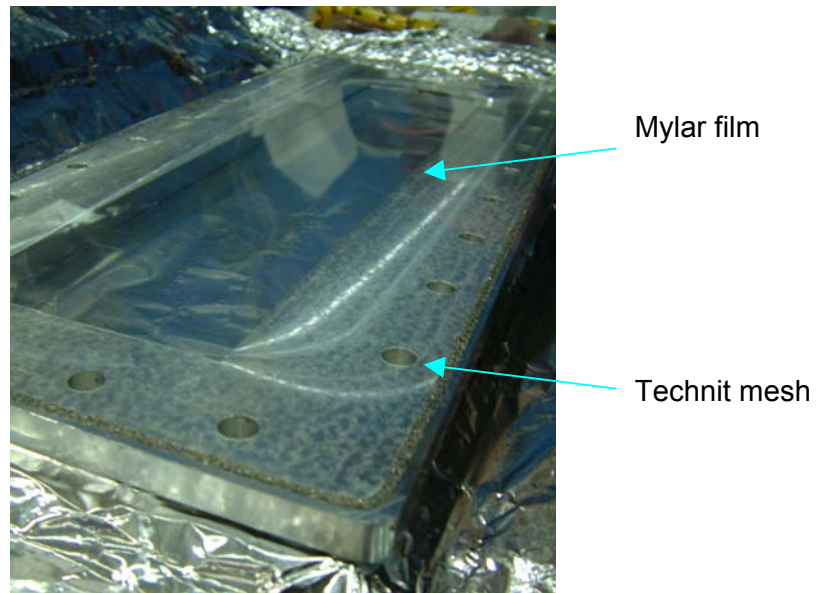


*Figure 52: Mylar window and flange showing the Technit mesh*

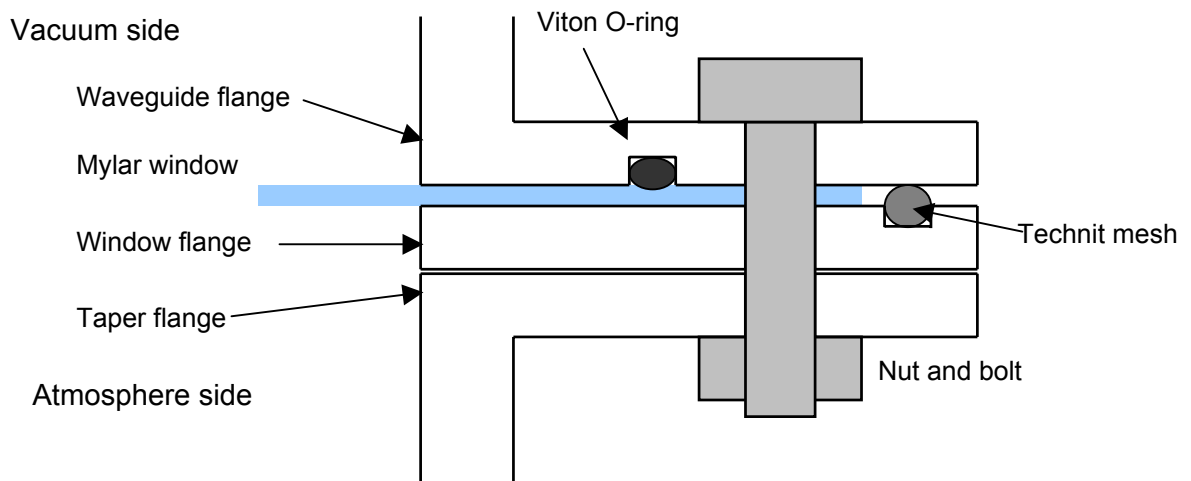


Figure 53: Schematic of the Mylar window flange set-up

The Mylar windows failed several times, but only when we pushed the average power up too high (an average power of 300kW CW seems to be the limit). Nonetheless, a discolouration was always visible in the centre of the intact window, indicating that it too was probably weakened and could have failed later on. Nonetheless the windows proved to be a viable option for short term experiments such as this, and windows have also been in operation in CESR for extended periods (albeit with no vacuum pressure to deal with, as they serve to separate a dry nitrogen section from a standard air-filled section of the waveguide). They had the additional advantage of being transparent, allowing us to look into the waveguide easily.



Figure 54: Discolouration in the upstream window after downstream window failure

### 5.1.3 Waveguide 3

The latest waveguide presented fewer problems than the previous two, but several issues did cost some experimental time.

The first problem is still not explained. The aluminium sample plate initially behaved normally and gave good results in the first tests. It was initially planned that the Al plate be used for the grooved waveguide experiments due to the relative ease with which grooves could be cut through the plate.

However, during a measurement that had started with on-scale measured currents, the level of multipacting went off scale after a brief ten-minute pause where no monitoring was done. No amount of processing could bring the levels back to their previous values. The plate was removed and cleaned locally at Cornell, using detergents and acetone, to no avail (very high multipacting currents remained), and even sent back to Daresbury to receive the same treatments it had been subject to initially (trichloroethylene treatment + sand-blasting). Even then the multipacting currents remained such that no measurements were possible. The most likely explanation is that the initial processing removed the layer of contamination that very likely existed on the sample plate and exposed the aluminium underneath. The question remaining, though, is why clean and pure aluminium should show such a high secondary electron multiplication factor. While aluminium oxide is known to have a high secondary electron yield, measurements of clean aluminium have shown levels comparable to other metals. A possibility was contamination of the aluminium surface by particles from other surfaces (e.g. the Mylar windows), but this is unlikely as this did not happen with any of the other plates, and the Al plate was cleaned several times after the first observation and still did not return to its initial state. Further investigations would be necessary to elucidate this question. They should include attempts to repeat the experiment (forthcoming investigations at Lancaster University could provide a suitable test-bench) and possibly attempts to study the surface of the plate.

The other problem that occurred was trivial but cost some experimental time. The problem came from an incorrectly connected cable, whose outer conductor was in contact with the oscilloscope, but not the core. It was therefore possible to see a signal from the waveguide, but at a very low level. This was not spotted for several days and

led us to believe that the reason behind the illogical measurements we could take lay somewhere else.

#### **5.1.4 Accuracy of the measurements**

One major difficulty with the measurements was that they were heavily dependent on surface conditions. Measurements of electron currents for different surfaces or sample plates were very difficult to compare to one another as repeating a measurement on the same plate might give different results. However, what is believable is the consistency and accuracy of the values of the electron current within a given measurement. It was verified that apart from the fact that as the measurement progressed, the surface was in the process of being conditioned (discussed in section 5.2.4), meaning that returning to the same value of forward power would result in measuring a slightly lower current (~0-5%, depending on the time between the first and second measurement – see also Figure 63 for an example of such behaviour).

As a result, none of the current measurements have error bars attached to them as the relative error between points is very small, but two measurements of the same phenomenon taken at different times could lead to different measurement curves. The reason for this is the difficulty in controlling surface conditions, not only of the sample to be studied but also of the entire vacuum system.

The difference in current measured by two different probes at the same time is however quite reliable, and the relative difference even for points taken at different times is quite small (i.e. the ratio of the current between the same two probes measured at the same power level, in the same conditions but during different sessions would be the same).

### **5.2 General observations**

#### **5.2.1 Starting conditions of multipactor**

Initially turning on RF power leads to electron activity observable on all electron probes and on the electron energy analysers starting at powers as low as 30kW of forward power. Vacuum pressure, initially stable in the range of  $5 \cdot 10^{-6}$ Torr also increases rapidly. This electronic activity typically increases rapidly with time, eventually leading to a light or vacuum trip (vacuum interlock set to trip at pressures over  $10^{-4}$ Torr). The whole process could take a fraction of a second initially, up to several tens of seconds on a waveguide

close to being processed. A light signal can be detected by the PMT (or photodiode) when the electron current builds up significantly, but is not consistently detected. In particular, as the electron activity eventually tends towards a stable level, no light signal is measurable on the PMT, and vacuum quality begins to recover despite the electron current still being picked up by the probes.

Figure 55 shows two graphs on the same event with two different timescales. The top graph clearly shows the build-up of electron current as measured by the EEA. The bottom curve, showing the signal from the photo-multiplier tube, only registers a signal when the current has built-up to a given level. The light then sets off the interlock, shutting down the RF leading to the disappearance of the electron current. The lower graph shows the detail of the PMT signal. Its non-continuous behaviour hints that the gas released by the multipacting current, when ionised, provides the light that the PMT measures, is released in clumps off the waveguide wall.

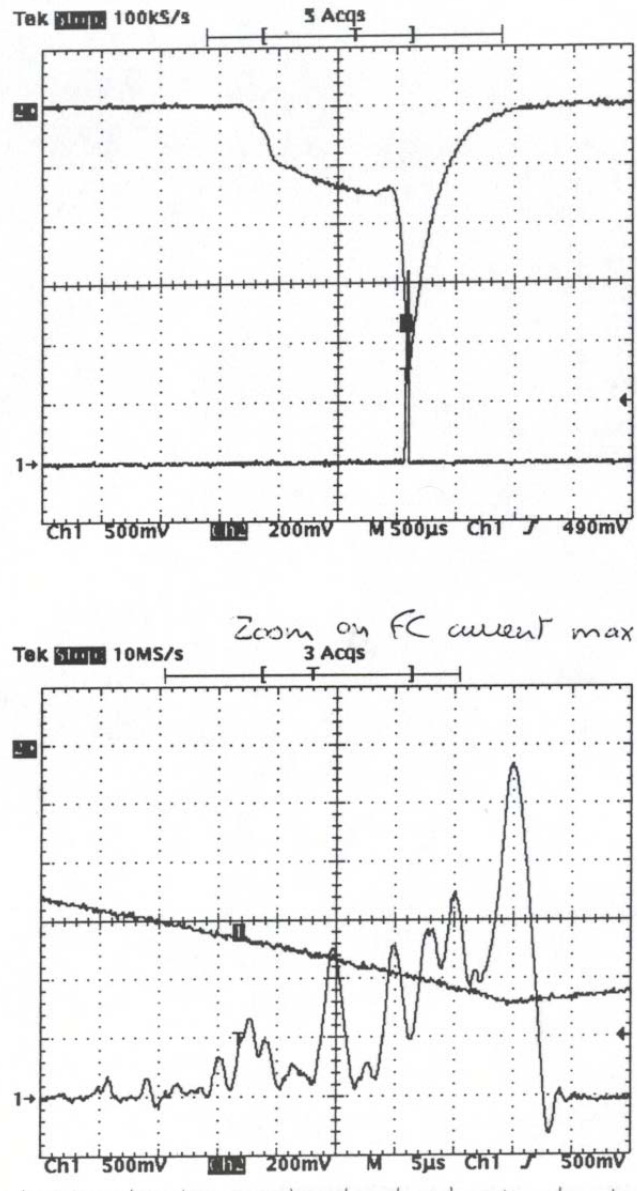


Figure 55: Electron current (channel 2, top) and PMT signal (channel 1, bottom). Bottom graph shows greater time detail than the top graph.

The onset power for the electron activity is typically around 30-100kW for an unprocessed waveguide, rising to 170-250kW for a waveguide that has been processed for several minutes. This applies to travelling wave situations only, standing waves lead to a lower onset power due to the higher electric fields at the anti-nodes of the standing wave pattern. An example of onset powers in a TW case is shown on Figure 56.

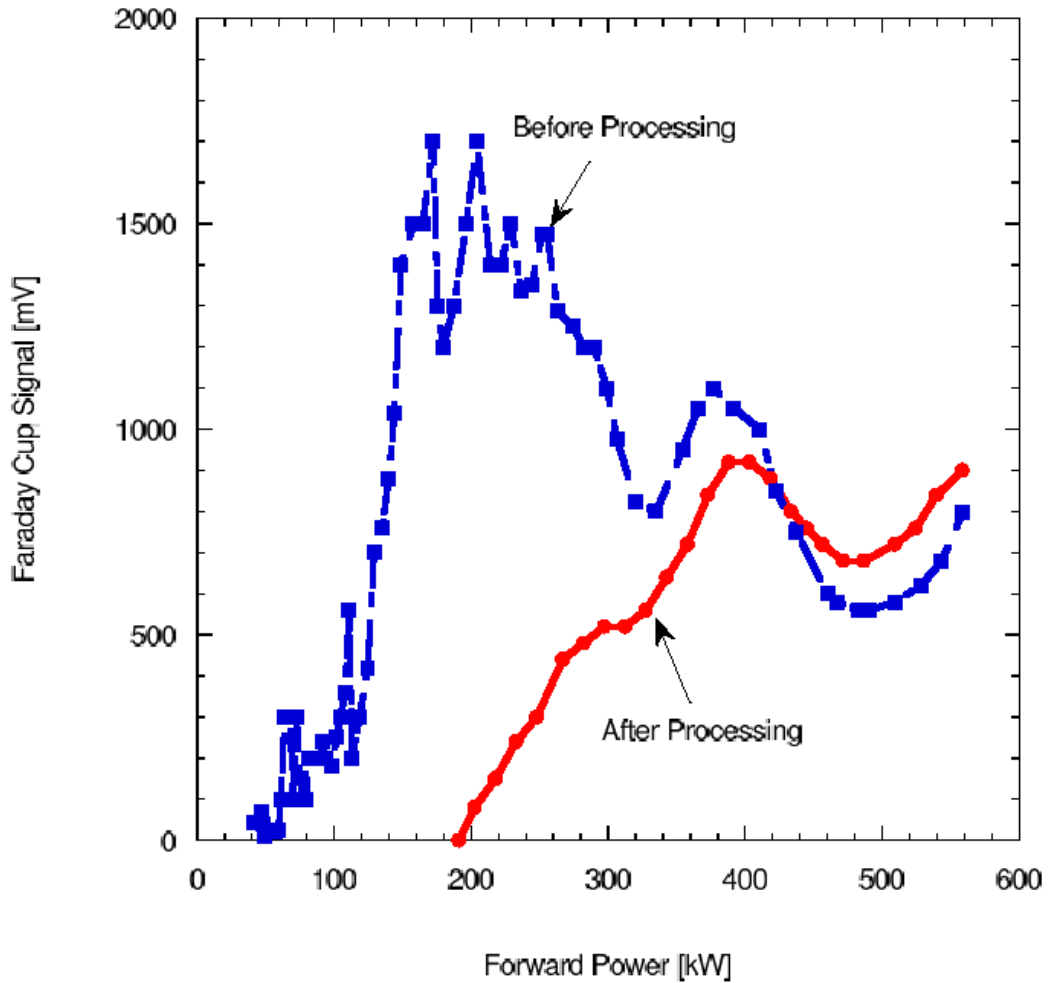


Figure 56: Electron current at different power levels (TW mode), before and after processing

A well-processed uncoated waveguide with no additional treatment, such as heating of the surface, typically has a multipactor onset point of 180-200kW. Assuming also that a processed waveguide has a maximum secondary electron yield of 1.2, while an unprocessed waveguide would have a yield of 1.9 (values from Figure 13), a simulation of the multipactor current in the waveguide (see Figure 57) gives a range between 80-90kW for multipactor onset on an unprocessed waveguide. This agrees quite well with most experimental measurements. The simulation tended asymptotically towards zero accumulated charge, but some slow multipactor build-up was always measurable even at low power levels. This would tend to indicate that to obtain multipactor build-up in the real situation, the effective average electron yield needs to exceed 1 (as measured from the simulation for 180kW, the average yield is approximately 1.2 and for 80kW,  $\delta \sim 1.1$ ). The reasons for this are likely to include phenomena not modelled in MAGIC such as collisions with gas molecules that would act in opposition to the multipactor phenomenon.

**Accumulated secondary electron charge  
after 120ns of simulation time  
at various maximum delta values**

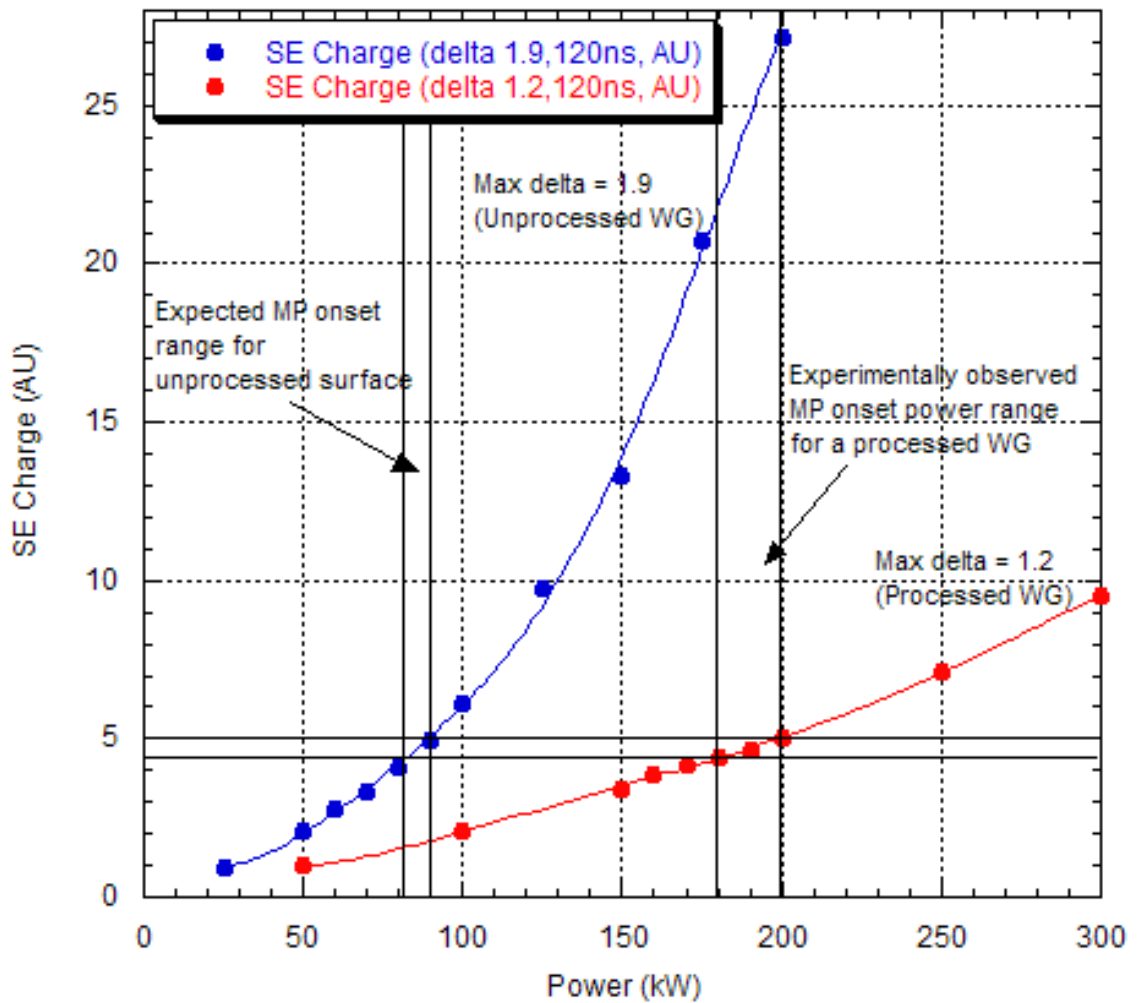


Figure 57: Accumulated secondary electron charge from a 120ns long MAGIC simulation for two values of the maximum secondary electron yield.

Our experimental observations allowed us to conclude that electron activity begins spontaneously with no need for stimulation other than that of the RF. The onset level is quite consistent and it can be estimated that the onset time once a given power level is reached is on the order of a few tens of micro-seconds. This is visible in Figure 59, where the initial rise-time is very short. Figure 58 also shows that the delay between a variation of the forward RF power and the multipactor signal is very short.

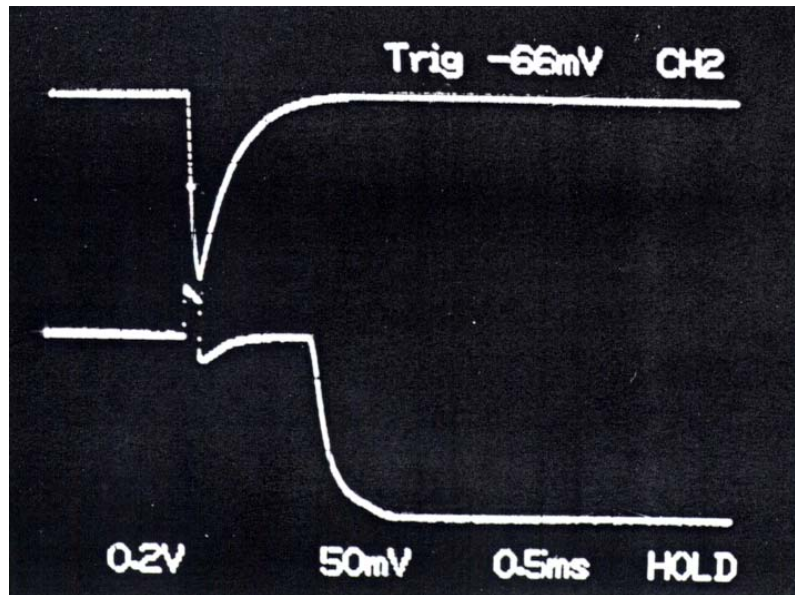


Figure 58: EEA current (top) and forward power (bottom) showing a 'tickle' on the power and its effect on the multipacting current.

Several attempts to seed multipactor while the RF was slightly below the multipacting threshold were unsuccessful. Several methods of triggering the multipactor have been tried, such as UV light aimed at the walls or a radioactive source applied next to the wall to release electrons into the waveguide and provide a 'seed' for the multipactor. None of the experiments were successful in consistently establishing a correlation between the source's proximity and the multipacting current. Sources such as  $^{60}\text{Co}$  ( $12\mu\text{Ci}$ ) and  $^{137}\text{Cs}$  ( $26\mu\text{Ci}$ ) were used. A reason for the lack of success is probably due to the fact that the source had to be placed outside the waveguide, and even though some of the radiation can pass through the wall, most of the interaction must happen at places where the electrons released can't make their way into the waveguide. Those electrons that do get freed must be in insufficient numbers to have any significant impact on multipacting.

One method that successfully restarted multipactor at power levels below the threshold was applying a magnetic field using the solenoid coil. This would allow multipactor to exist briefly before eventually processing itself away. An explanation for this would be that the magnetic field allows electrons to have multipactor trajectories impacting on areas of the wall that had not been processed as thoroughly as the central region of the waveguide that is cleaned by the classic multipactor (as described later in section 5.2.3).

### **5.2.2 Identification of multipactor**

The electron activity observed in the waveguide could at first glance be due to a number of phenomena. Given the rather poor vacuum in the waveguide, it was conceivable that the activity could be due to a gaseous breakdown discharge. However, for such a discharge to occur, across a gap width in excess of 10cm, the electric field would need to be in the order of  $10^4\text{V}$ . Once significant electron activity has been excited by multipactor, it however releases gas from the walls and may lead to a discharge as described in [41].

Multipactor is dependent on the existence of a resonant process of electron multiplication. By altering the trajectories of electrons, the multipactor process can be affected. A method of achieving that while not affecting any other condition is to introduce a weak (several Gauss) magnetic field. This was done and a change in the measured signal was immediately observed. A field of  $\sim 10\text{G}$  was sufficient to completely remove the signals (this is discussed in more detail in section 6.1.1). This, coupled with the electron energies measured (section 5.2.5) allowed us to conclude that the phenomenon was indeed multipactor.

### **5.2.3 Location of electron multipactor**

The electron current can be measured by the probes located in the centre of the waveguide broad wall and the probe located on the sidewall (for WG1 and WG2, WG3 has similar arrangements). Whenever any current is measured at one probe, all of the probes pick up some signal, meaning that even though the multipacting phenomenon may be localised, some electrons travel as far as the sidewall. The general trend of the various signals is also very similar, as shown in Figure 59. P3 and P4 are electron probes located at different locations along the centreline of the broad wall. This graph effectively shows the similar evolution of the current at two different locations on the centreline over a RF pulse.

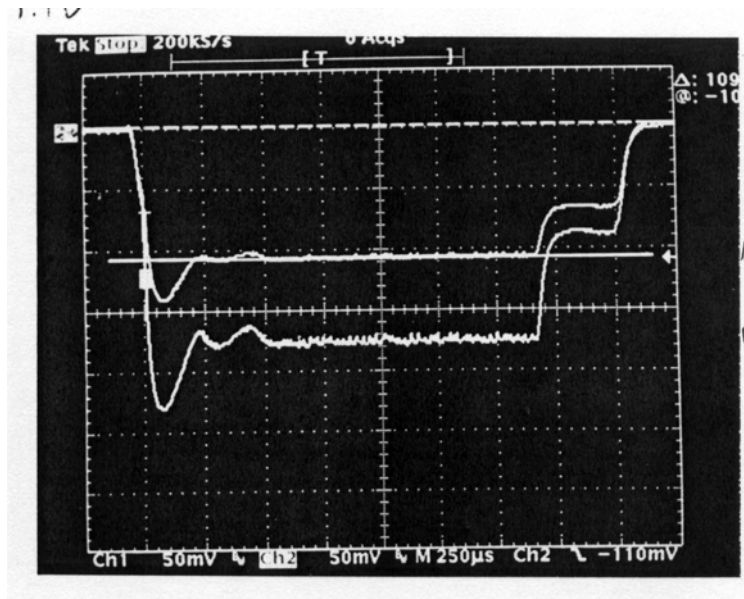


Figure 59: Signal from probes P3 (top) and P4 (bottom) (on centreline of broad wall) as a function of time (WG1/2)

Figure 97 and Figure 98 (in section 6.2.1, pages 118-119) show the current measured by otherwise identical probes (P1-P8) located at various locations over the waveguide. All probes pick up a similar signal that generally shows the same trends of evolution at different power levels.

The current intensity was measured to be most important at the edges of the waveguide, as shown on

Figure 60. This can partly be attributed to the uneven processing of the waveguide walls (due to the central location of the sustainable multipactor region as well as the higher electric field intensities (leading to higher electron energies) near the centre-plane). The secondary electron yield of the waveguide wall was therefore lower in the centre than the edges, allowing the electrons drifting towards the sidewall to multiply before rejoining the cloud of low energy electrons that congregate near the sidewall (due to the lack of electric field in that region). Further discussion of this effect is given in Section 5.3.2, where it is shown that the higher current near the sidewall is a fundamental property of multipactor in rectangular waveguides.

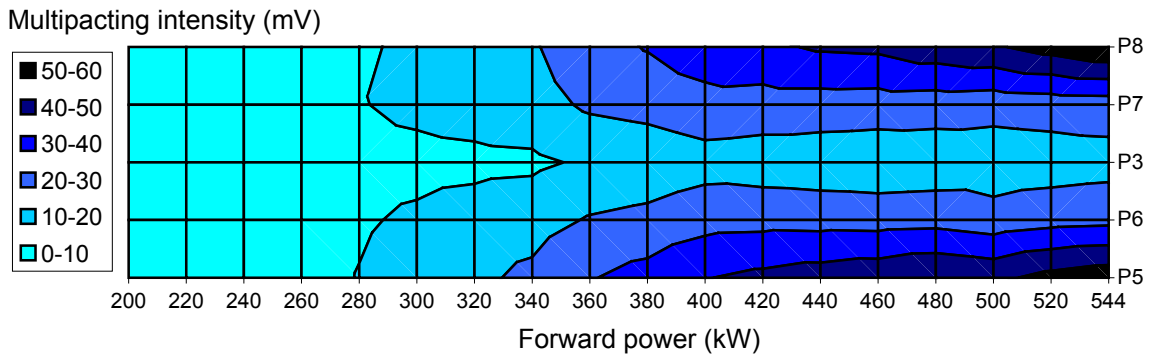


Figure 60: Intensity of multipactor current at different power levels (Cu plate, WG3))

Attempts were made to capture temperature maps of the breakdown event, both from the view-ports on the waveguide bends and from the outside of the waveguide. An IR camera was used for this purpose (Infrared Solutions – IR Snapshot). Due to the long scan time of the camera (2-3 seconds) no instantaneous data could be captured. The figure below is an example of the pictures that were taken. It shows a central spot of heat, most likely due to the heating up of the Mylar film. The other hot spots are actually reflections of the main one on the waveguide walls.

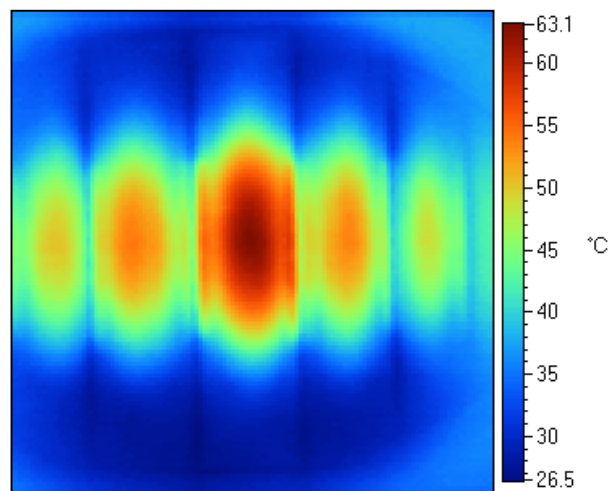


Figure 61: Temperature map of waveguide interior taken from view-port

## 5.2.4 Surface conditioning

The evolution of multipactor in the waveguide with time is affected by what is commonly termed processing, or conditioning. Studies of the process have been carried out

extensively by the CERN vacuum group [25, 42] in order to understand the electron cloud effect, which is a form of beam-induced multipactor that occurs in accelerator beam tubes. Many other studies of processing have been conducted by teams at CERN [43], KEK-B [44] and SNS [45] for instance.

We have observed processing in the course of the waveguide experiments. Initially, when applying RF on a new (vacuum cleaned but unprocessed) surface at a power level where multipactor can exist, the vacuum quality in the waveguide is severely degraded (exceeding the vacuum interlock limit, usually set at  $5 \cdot 10^{-4}$  Torr); this is accompanied by flashes of light. Either of these can set off the interlock system, which shuts down the RF for three seconds (preset duration chosen for the RF control system). This can be seen in Figure 62, which shows electron current (negative) and the PMT signal over a long timescale (5s/div). Initially RF trips occur frequently, with a rapid electron current build-up and PMT signal. This leads to an interlock trip and a three second downtime. As time passes, the trips become more and more infrequent and finally cease. The current stabilises and begins to diminish slowly. The light signal also disappears and we enter a phase of stable multipactor current, at which all of the other numerical measurements were made.

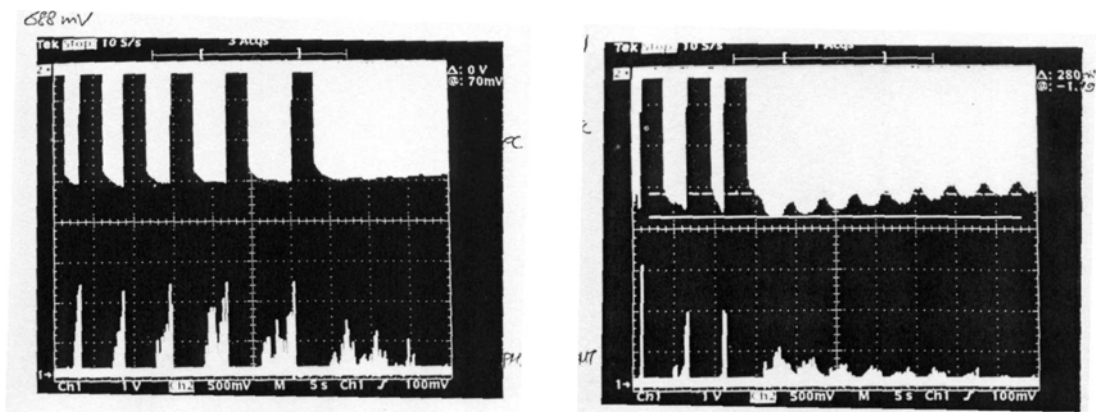


Figure 62: Electron current (top) and PMT signal (bottom) evolution with time (5s/div)

The power level studied in Figure 62 was such that some electron current remained after the trips had cleaned the surface. In other lower power cases, the electron current would disappear completely. This limit is shown on Figure 56. This difference is commonly referred to as a ‘hard’ multipacting band as opposed to a ‘soft’ band that can be processed out entirely; soft bands typically occur at the lower power levels.

The oscillation apparent in the trace of the current measurement (of Figure 62) was due to an instability of the RF drive that translated into a slight oscillation of the RF power, which in turn translated into a noticeable variation of the multipactor current. The explanation for this is that the waveguide in the experiment above was only processed up to the power level at which the measurement was taken; higher power levels had not been reached yet. The oscillation therefore briefly allowed electrons to multipact at higher power levels, therefore affecting surfaces that had not been processed yet.

This appears to be in contradiction with the observations of section 5.2.3 that show that electron multipactor is picked up all over the waveguide. However, while the electron spray may occupy the entire volume of the waveguide, the higher energy multipacting electrons can still have localised trajectories and scrub particular surfaces of the waveguide only. This explains why processing a waveguide requires a gradual ramp-up of the power until the maximum power level is reached. It was also apparent that if RF was applied at a given power range (high power, for instance), the benefit of the conditioning at other power ranges was gradually lost. Continuing the example above, after a long stay at high powers, when we returned to lower power levels the waveguide would quite often exhibit tripping behaviour (this is illustrated in Figure 63 where there is a large current spike (accompanied by some RF trips) at the lower power levels despite the fact that the waveguide was processed thoroughly before measurements started at a high power). This is likely to be due to gas being shuffled around the surfaces, ejected from those areas affected by the given power level only to deposit itself in unaffected areas.

Also visible on Figure 63 is the difference in current at the start and end of the measurement (e.g. 540kW, 183mV on P3 at 12:55, compared to 157mV on the same probe at 14:28). This graph illustrates the effect of processing, at various locations on the waveguide, which is also very visible in the fact that the large spike measured from 13:20 to 13:40 is very much reduced the second time the RF power was at the same level (13:55-14:10).

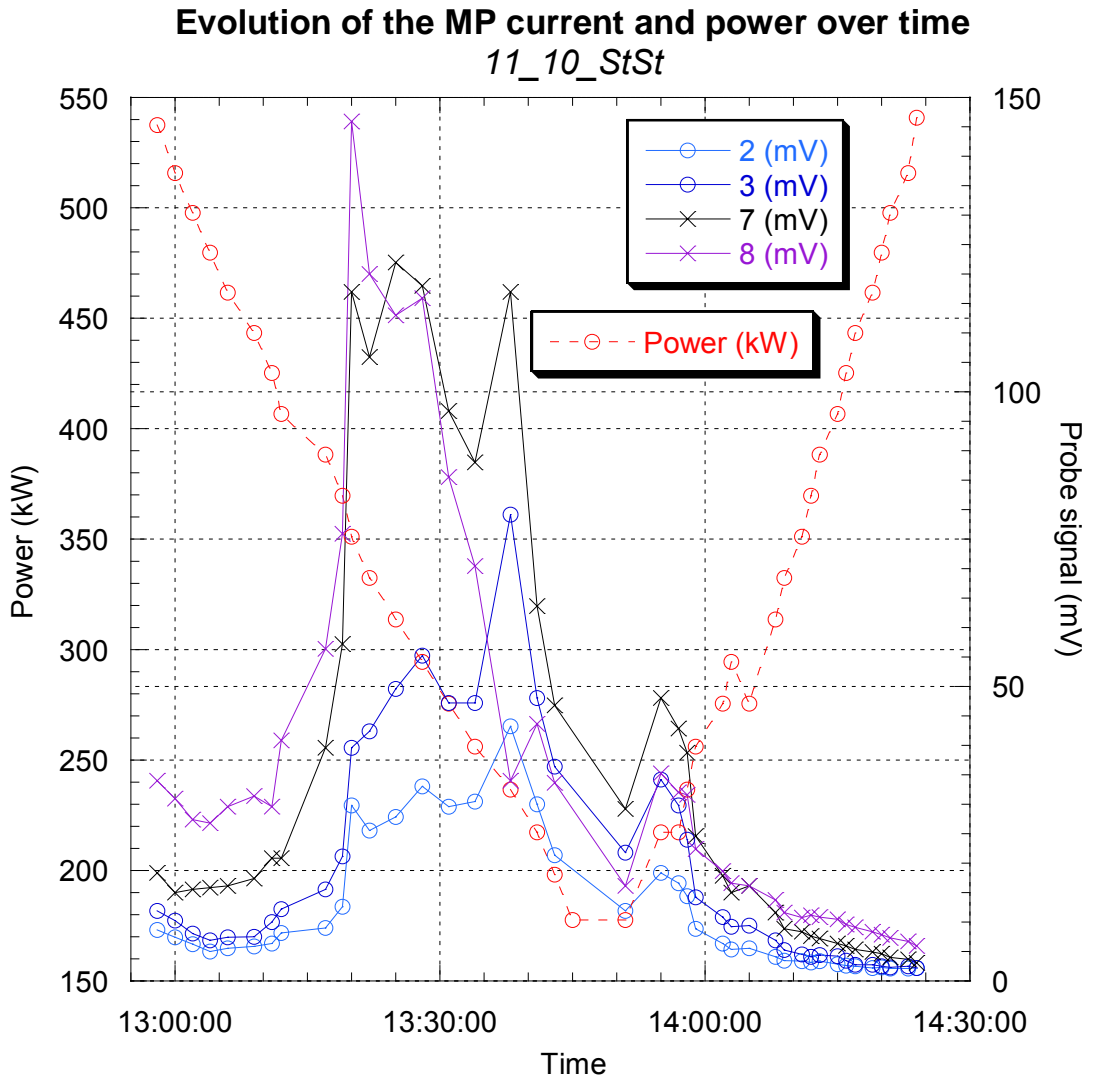
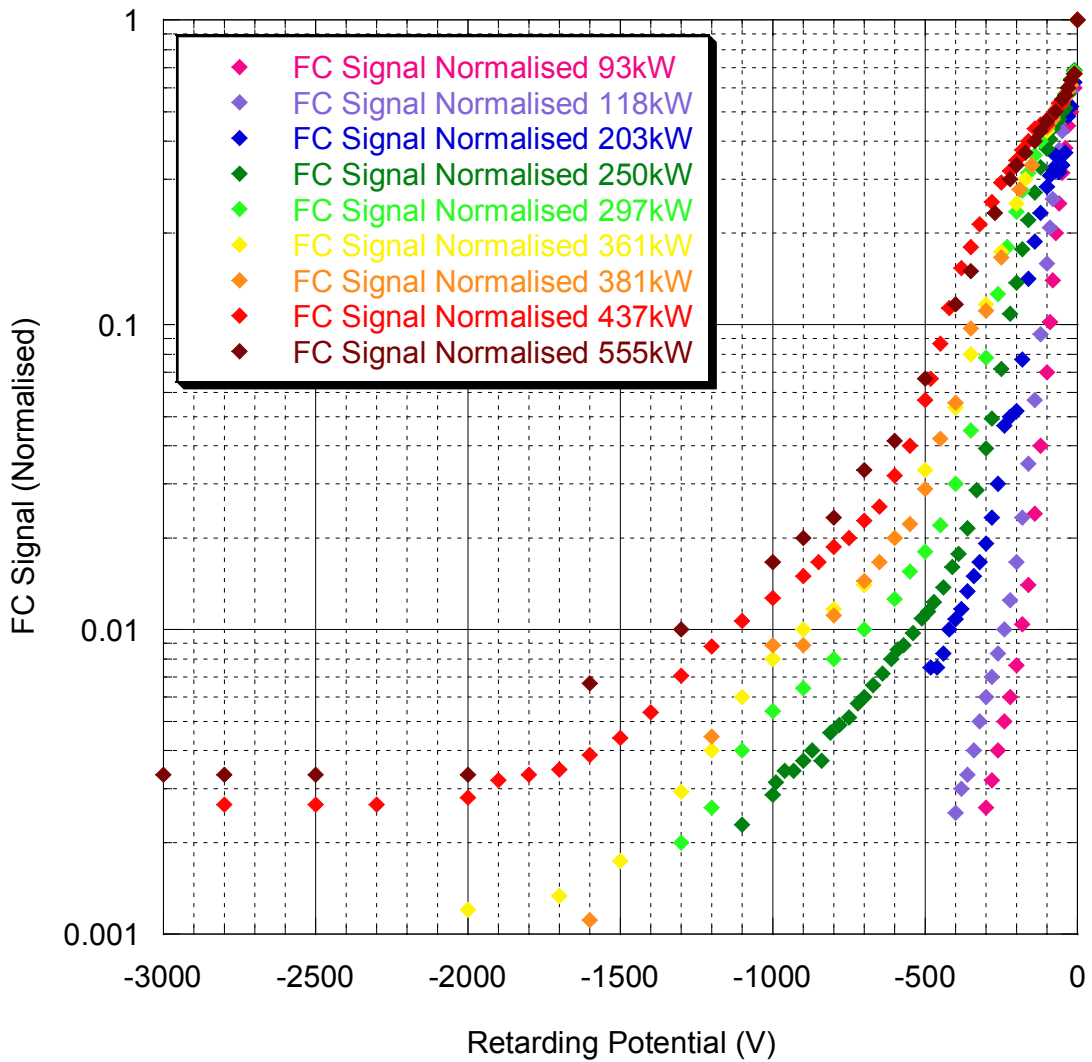


Figure 63: Evolution of (post-processing) multipactor current during a measurement

### 5.2.5 Multipacting electron energies

The electron energy analyser was used to scan the energy ranges of the electrons in the waveguide. A summary of the results from WG1 and 2 can be seen in Figure 64. To minimise the time-dependent effect of processing, each measurement was taken in as short a time as possible (generally 15-20 minutes) after the power had remained stable for at least 10 minutes. The effect of processing was nonetheless generally still measurable by re-measuring a point. The difference in current was typically in the order of 5%.

**Normalised EEA scans WG1/2**  
*All EEA Norm Data.qda*



*Figure 64: Normalised integrated electron energy distribution at various power levels for WG 1 and 2. All plots normalised at 0V retarding potential.*

The EEA was mounted behind a small hole in the centre of the broad wall. The measured energies were normalised at a 0V retarding potential. It is apparent on Figure 64 that most curves show a significant (30-50%) proportion of very low energy electrons (energies below 10V). These electrons compose the electron cloud that does not directly participate in the multipactor process but drifts in the waveguide and helps to seed the multipactor.

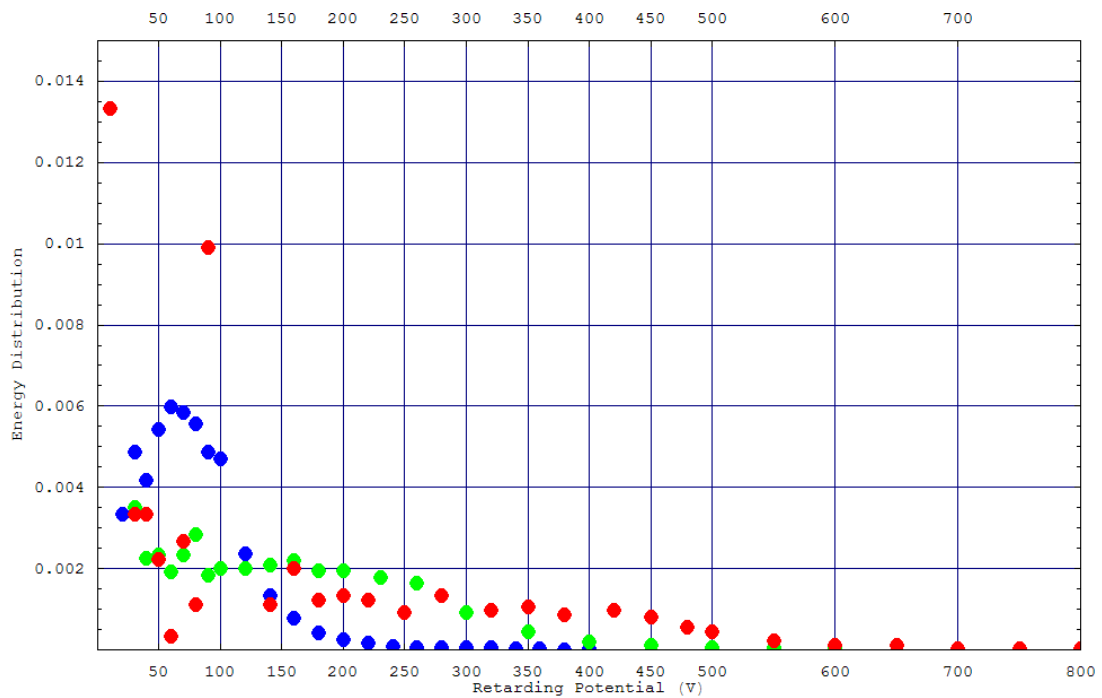


Figure 65: Differentiated energy spectra for a forward RF power of 118kW (blue), 297kW (green) and 437kW (red).

Differentiating the data led to distribution curves such as those shown in Figure 65. The curve for a forward power of 118kW (in blue) clearly shows a peak centred at 60eV. The two other curves aren't as distinct but also show a distribution of electrons up to energies of around 500eV, with maxima around 155eV and 260eV for forward powers of 297kW and 437kW respectively. Figure 64 shows that most of the multipacting electrons (>90%) have energies below 100-450eV (for RF forward powers from 93-555kW). The number of higher energy electrons appears to increase linearly with the RF power level, as can be seen in Figure 66. It is interesting to notice that the measured electron energies compare well with those at which the secondary electron yield of the surfaces (as measured in Figure 17) is maximised (stainless steel:  $\delta_{max} \sim 400\text{eV}$ ), evidence of the self-sustaining nature of the multipacting process that allows most of the electrons to impact at energies that result in increased in multipacting.

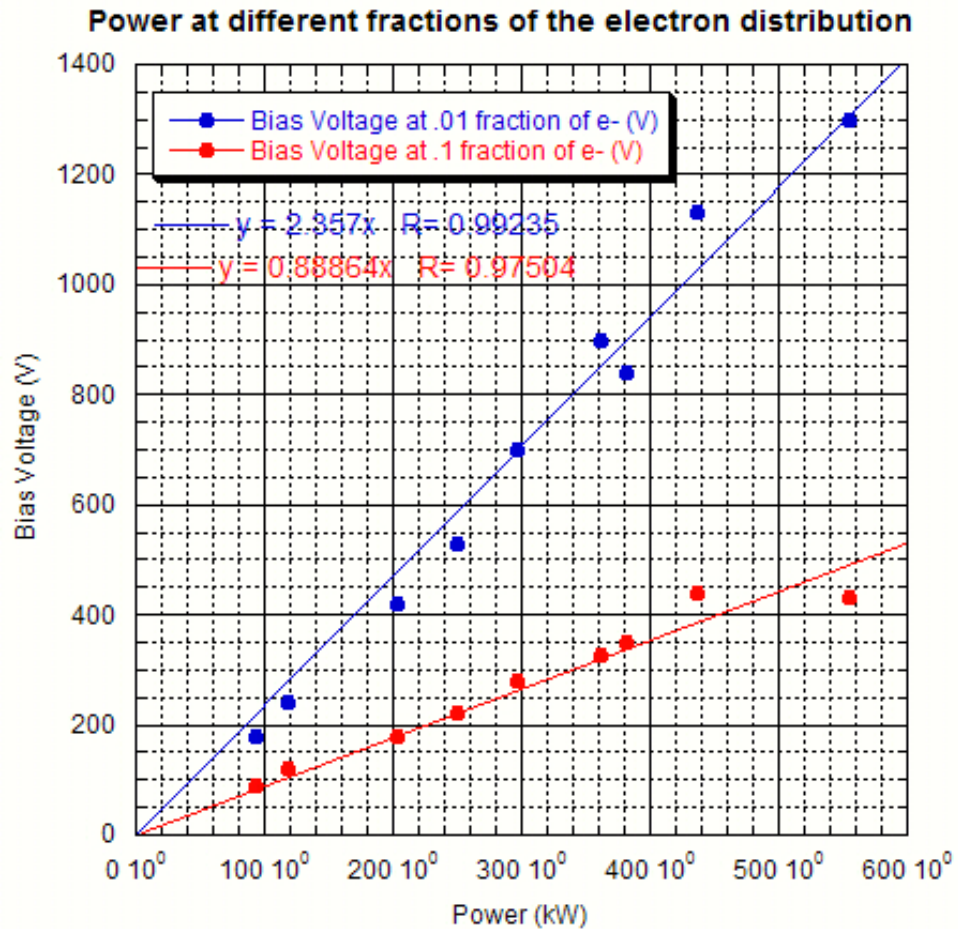


Figure 66: Bias voltage for given fractions of the electron distribution at different power levels (from data in Figure 64)

Data were also collected during the WG3 experiment. There were two Faraday cups on the waveguide; EEA1 is similar to the EEA on WG1 and 2, being in the middle of the broad wall. EE2 is on the sidewall at the same level as EEA1.

Figure 67 gives results for EEA1, showing the same general trends as for WG1/2 as on Figure 64. No systematic scan of the electron energies was carried out in the WG3 experiment, but an attempt was made to see if the various groove or coating configurations had any notable effect on the electron energies. None is immediately apparent, though the copper bar seems to have added an inflection point around 500eV (green solid dot and red solid square on the graph for powers of 407kW and 498kW respectively). The curves being normalised at 0V, it seems to indicate a lower proportion of mid-energy electrons (10-300eV approximately) than the other cases. This could be explained by the fact that more multipacting electrons are lost on the bar than with the other cases, while the electron cloud retains a distribution similar to that of the other sample plate configurations. Supporting evidence of that is that there is no apparent

difference in the data measured at EEA2 between the cases with a copper bar and without (Figure 68).

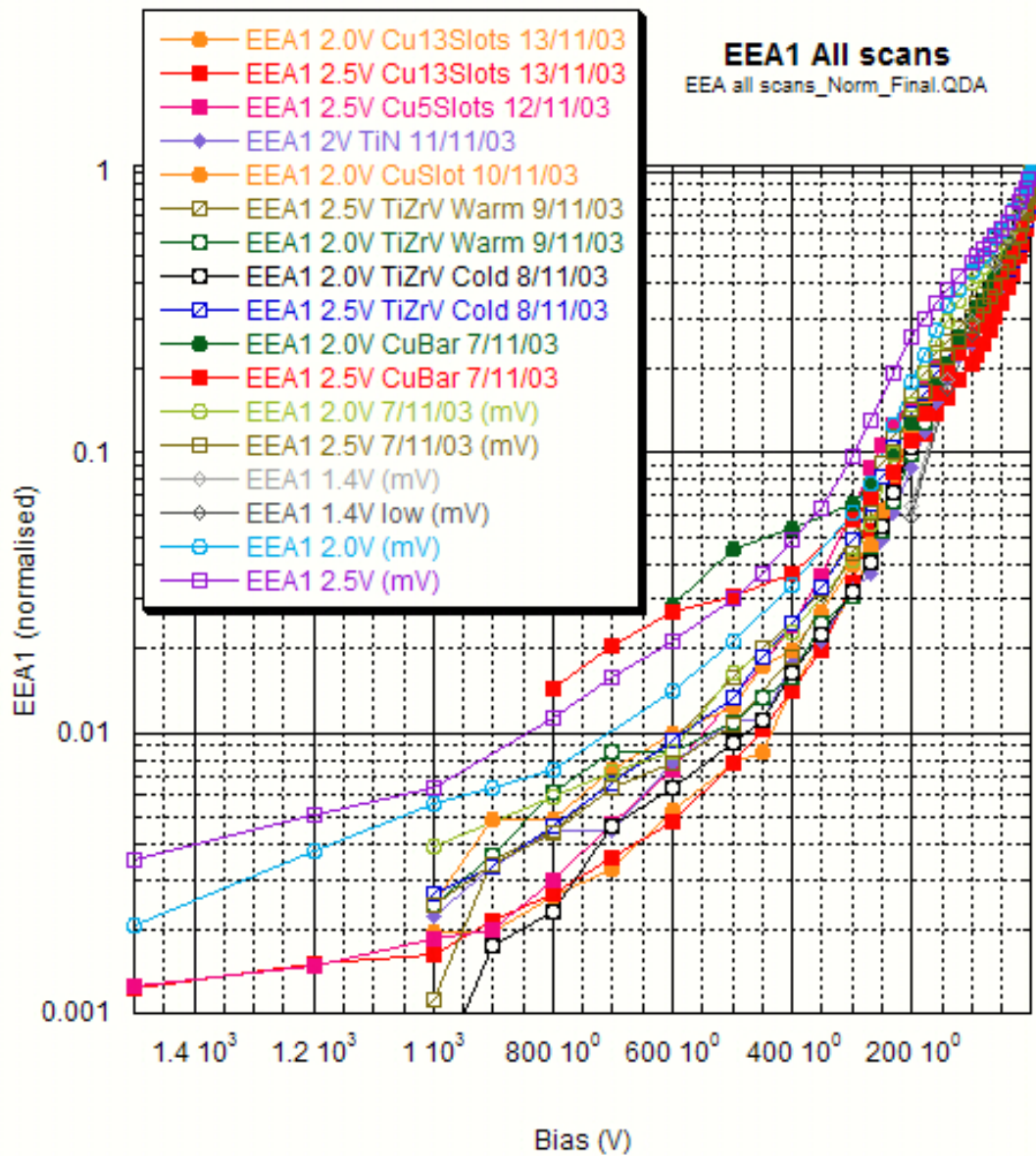


Figure 67: Normalised integrated electron energy distribution at various power levels for EEA1 of WG3. The voltage given in the legend refers to the power as measured by the meter. The power calibration gives 2.5V=498kW, 2V=407kW and 1.4V=295kW.

EEA2 being located on the sidewall, the current it picks up consists of electrons not actively engaged in multipactor. This gives a fairly good representation of the energies of the secondary and reflected electrons in that low field region. It is readily apparent from Figure 68 that more than half of the electrons picked up at that point have energies below 10eV. Less than 1% of electrons have energies greater than 100eV; these are likely to

either have been reflected off a surface or crossed the waveguide laterally as the field in the vicinity of the probe is close to zero (the waveguide transmits RF in a TE<sub>10</sub> mode).

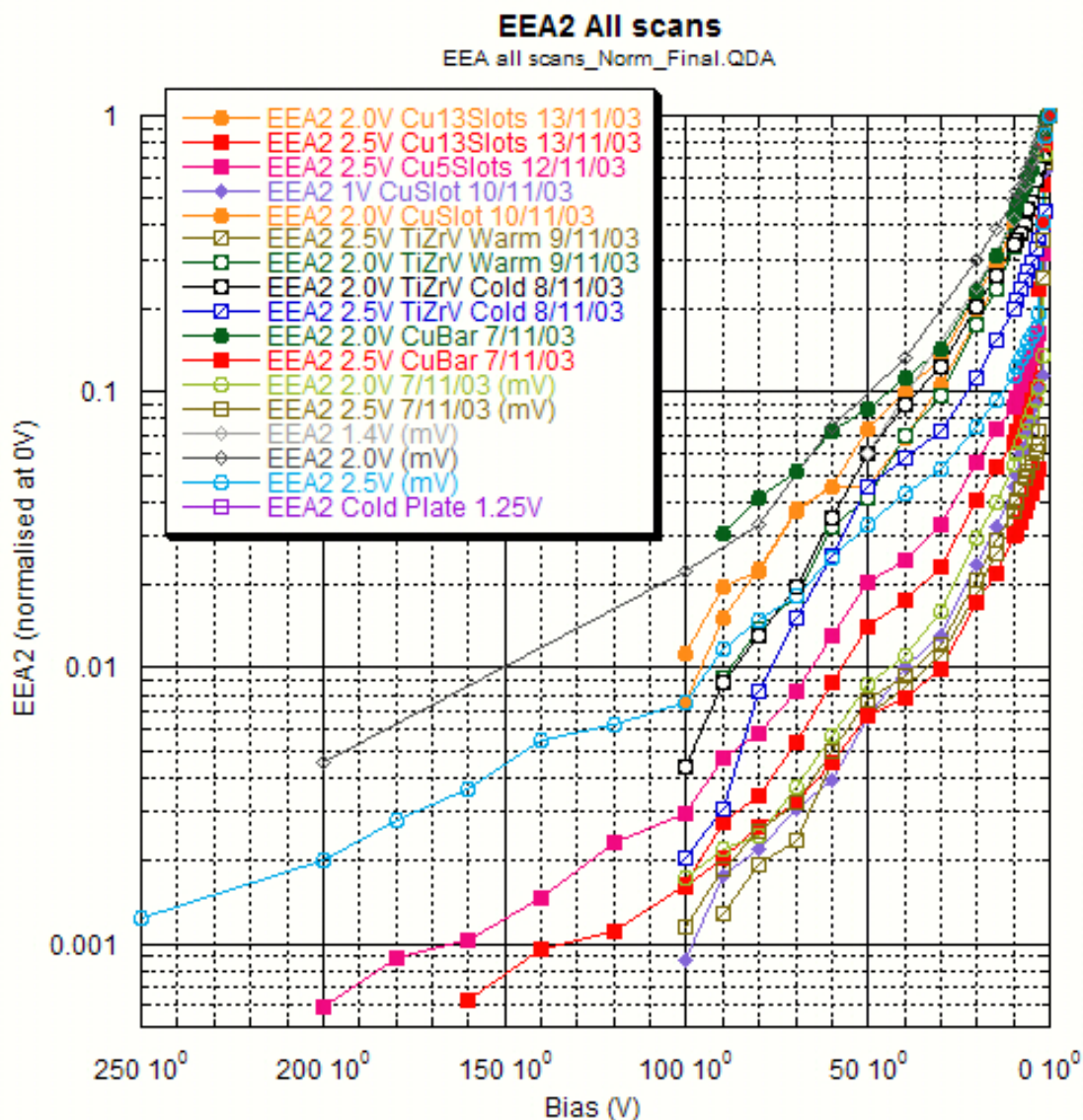


Figure 68: Normalised integrated electron energy distribution at various power levels for EEA2 of WG3. The voltage given in the legend refers to the power as measured by the meter. The power calibration gives 2.5V=498kW, 2V=407kW and 1.4V=295kW.

A comparison of the distributions measured at EEA1 and EEA2 can be seen in Figure 69. The much greater proportion of higher energy electrons captured by EEA1 is clearly visible. Both curves show an important very low energy component. The curve from EEA2 mirrors the shape of the curve from EEA1, which gives confidence that the electrons measured by the energy analysers come from the same phenomenon. The accuracy of EEA scans is quite high, as they are taken over a short time period and do not suffer greatly from surface conditioning and the resulting diminution in electron current.

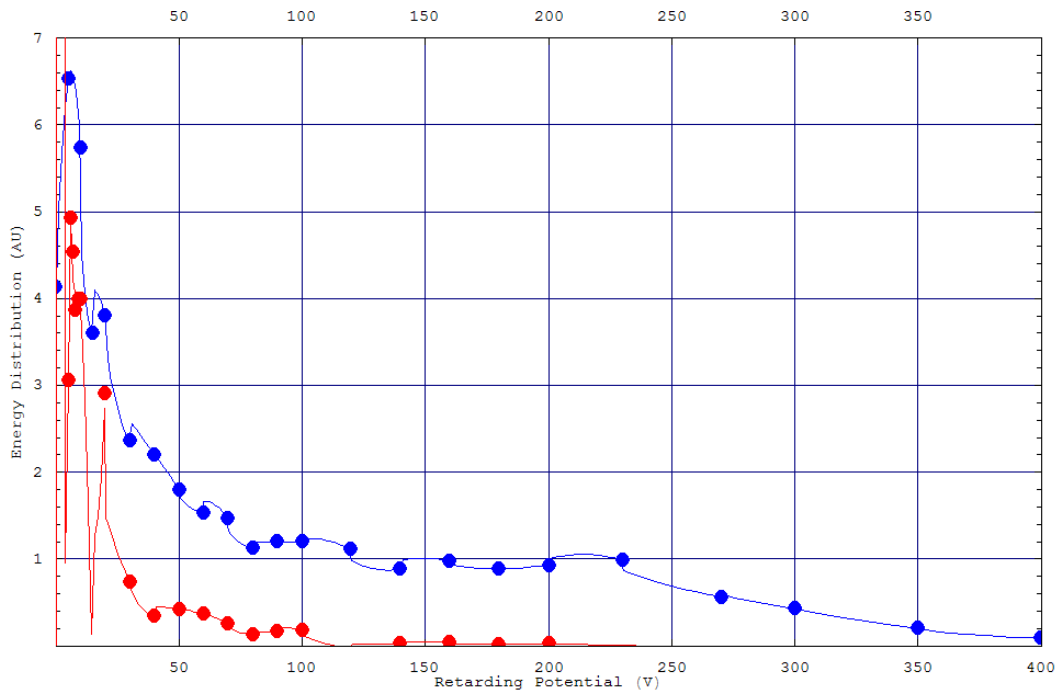


Figure 69: Electron energy distribution for EEA1 (blue) and EEA2 (red) at 498kW with a copper plate (from EEA1\_2.5V and EEA2\_2.5V). The fit is the result of an interpolation and can be disregarded, particularly in the area around 20eV.

It is interesting to notice that the small bump at 20eV that might otherwise be dismissed as an error inherent in the data taking is visible in both curves (despite having been sequentially in time). No explanation obvious for this bump was forthcoming.

## **5.3 Comparison with simulations**

### **5.3.1 Multipactor bands**

Standard multipactor simulations show distinct multipacting bands. Experiments show a continuous multipactor current with peaks and troughs but no gaps in the spectrum. Once multipactor appears (experiments gave a lower power limit of 80-200kW, depending on the degree of processing the waveguide has been exposed to), the current remains unless the entire wall processes to such a point that no multipactor current remains regardless of the power level.

Experimentally, band-like behaviour was occasionally observed. On such example can be seen on Figure 59 in the jumps from one level of current to another depending on RF power, time, or the level of cleanliness of the surface at a given moment. No distinct band structure was observed, but peaks and troughs are clearly visible in the various power scans of the waveguide (examples of this are visible in Figure 56, Figure 97 and Figure 98). This suggests that the phenomenon is much more complex than simple simulations might suggest. It is very probably also a result of the fact that the multipactor that can occur in the waveguide is a high order multipactor, its order being between 7 and 9 depending on the power level. High order multipactor bands are close together (as can be seen in Figure 16, the high order bands being the ones to the left of the figure, as they require less power to send the electron across the waveguide). That closeness leads to the increased possibility of blurring the bands, due to such processes as out of phase electrons having the possibility of bouncing off the surfaces (high low energy backscattering probability) until they drift back into the multipacting electrons. Simulations carried out with MAGIC, as well as other codes [31], show the possibility of cross talk between the stable multipactor phases. Another factor acting in favour of blending the bands is the fact that the electric field envelope in the waveguide has a cosine distribution across the width of the waveguide in the TE<sub>10</sub> mode (maximum in the centre, no field near the sidewall). This allows different wall-to-wall trajectory transit times to exist in the waveguide, and can be compared to having electric fields equivalent to a variety of power levels in a two-plate system across the width of the waveguide.

## Comparison between MAGIC simulation of multipactor and experimental data

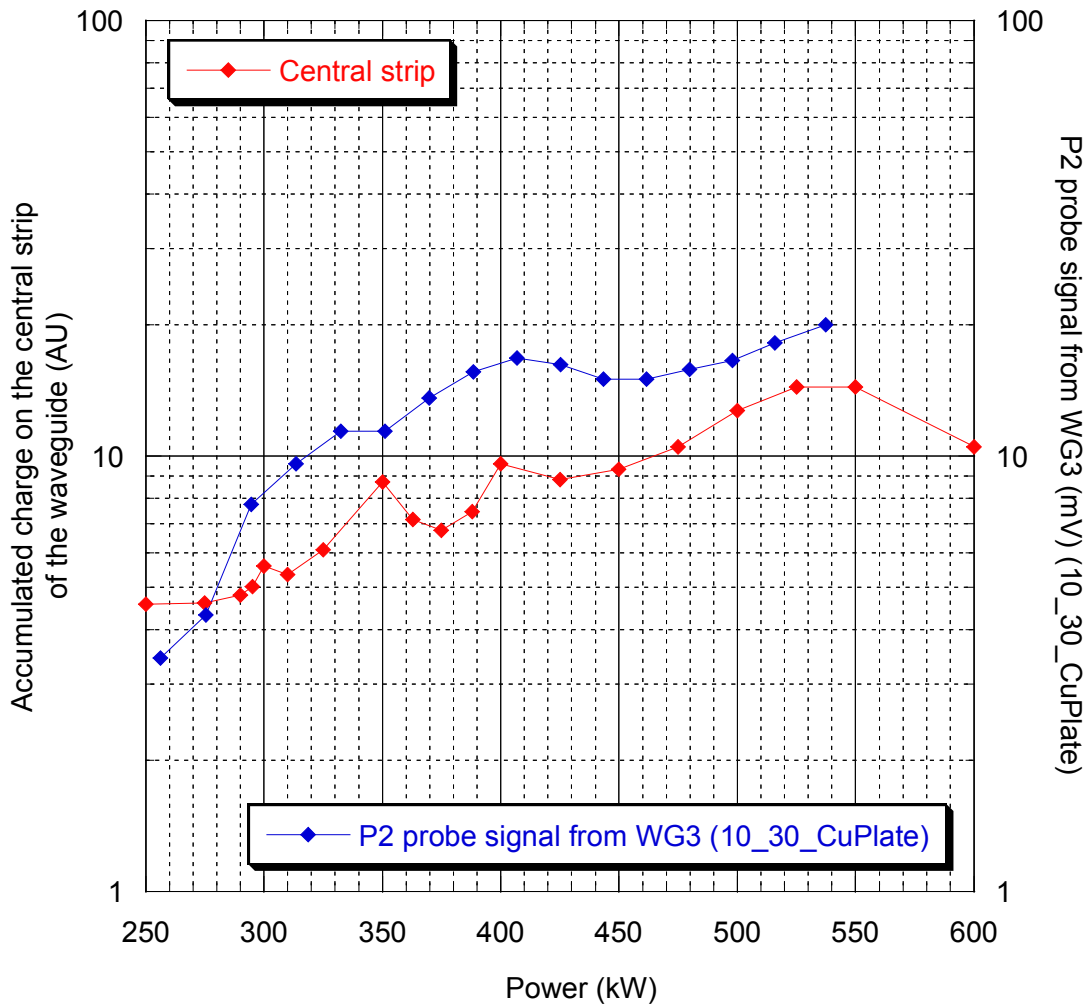


Figure 70: MAGIC simulation of multipactor with only a 3.04cm strip on the centreline having a non-zero secondary electron yield, compared to a measurement from P2 (located on the centreline) on a plain copper waveguide

The introduction of low energy electron reflection widens the bands in standard simulations, while the early MAGIC simulations that did not incorporate such a low energy reflection showed little or no multipactor. MAGIC simulations show only minor effects on the charge ‘accumulated’ on the walls in a given time at different power levels, as can be seen on Figure 70 (‘accumulated’ is in brackets as the charge is not conserved by the wall, which is a perfect conductor, but only counted by the code for the purpose of the measurement). That particular series of points was taken after 100ns of simulation at the various power levels. It also restricted multipactor to distinct sections of the waveguide width. The simulation shows a continuum of multipactor current similar to

what was observed in the experiments (a curve showing similar behaviour on a plain copper waveguide is added for comparison).

### 5.3.2 Location of electron multipactor

MAGIC simulations conducted in a rectangular waveguide show the drift of electrons towards the sidewall of the waveguide. That effect was already observed in previous particle tracking simulations, but MAGIC and the possibility of making videos of the phase-space make it even more obvious. It is readily apparent in Figure 71, which shows a majority of electrons following nearly direct wall-to-wall trajectories in the centre of the waveguide, but also a number of completely off-phase electrons travelling slowly across the breadth of the waveguide. It is also apparent that as we look at electrons further away from the centre of the waveguide, the rate at which they head towards the sidewall (i.e. the angle of their trajectory compared to a vertical line) increases dramatically. This helps explain the high current picked up by the probes located off-centre and on the sidewall.

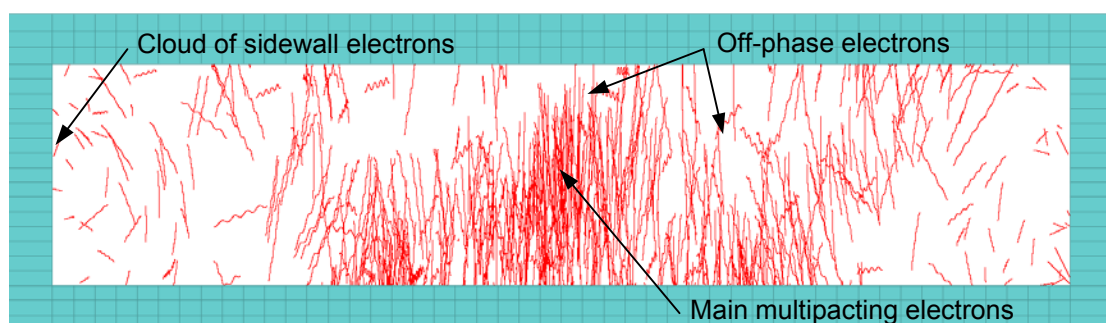


Figure 71: Trajectories of multipacting electrons after 105ns of simulation time (~5 impacts of the main multipactor mode)

Simulations have also been conducted measuring the accumulated charge on small areas of the surface placed at the same location as the electron probes in WG3. While the results (shown in Figure 72) show quite a lot of noise, it is apparent that P1 to P4 show very similar levels of charge. This is to be expected because they are all on the same line in the middle of the simulated waveguide. The levels measured in WG3 experiments tend to show similar levels between the probes composing the pairs P1-P4 and P2-P3. The pairs P1-P4 and P2-P3 may however show different signal levels, even in cases where they theoretically should not measure any difference (as in Figure 73). Causes for that difference may include the greater proximity of P1 and P4 to the Mylar windows, as well as the fact that the actual stainless steel waveguide body is closer to

P1-P4 than P2-P3 that measure electrons coming almost exclusively from the sample plate. The kink apparent in the figure around 375kW appears to be more than a glitch of the code (nearby power levels confirm its presence, but no explanation was found for it).

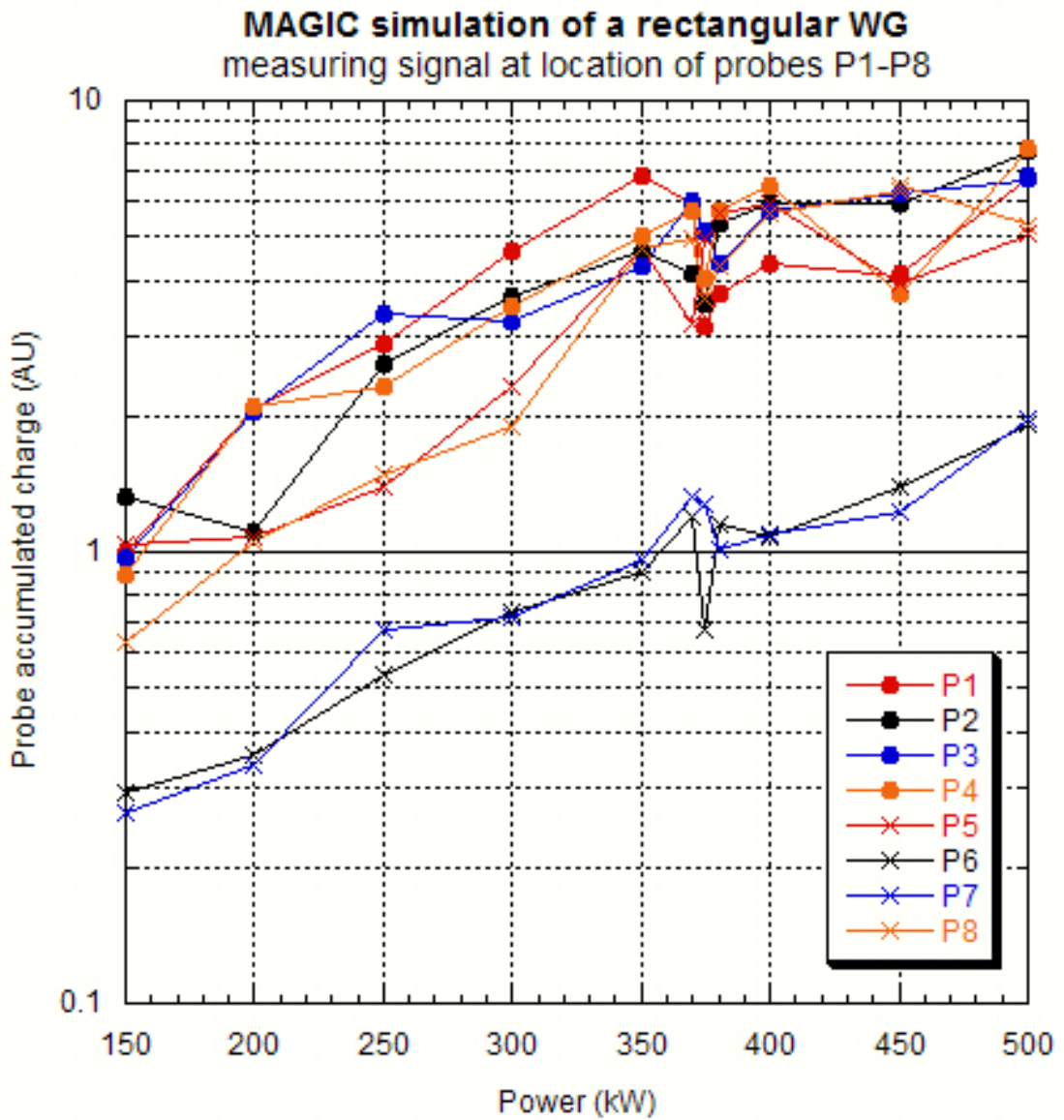


Figure 72: MAGIC simulation measuring the accumulated charge at the location of P1-P8 after 100ns of simulation run-time

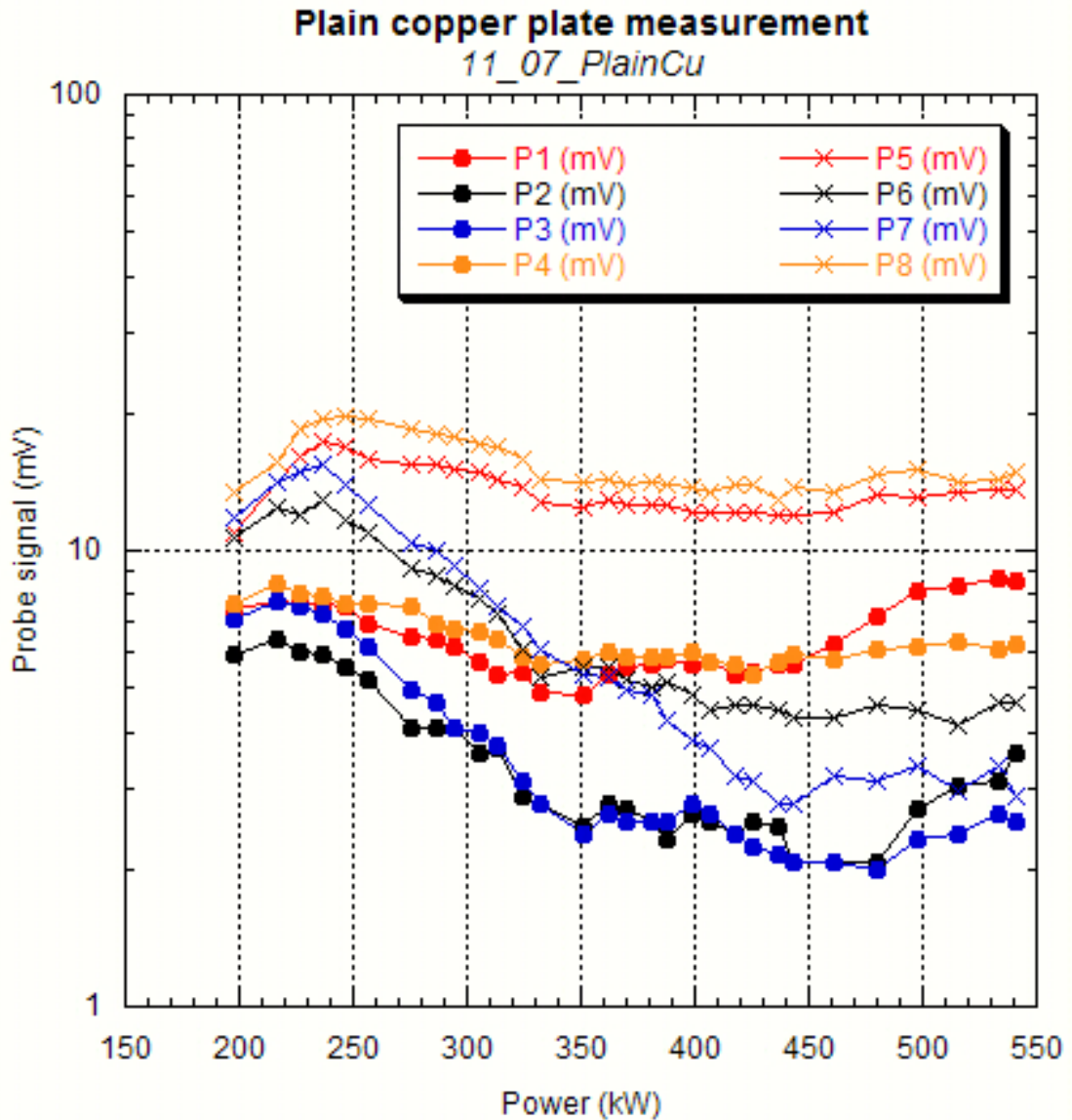


Figure 73: Measurement of P1-P8 from a plain copper plate

It is also interesting to notice from Figure 72 that P5-P8 in the simulation, that has a uniform secondary electron yield along the waveguide surface, shows a higher signal level than P6-P7. This tends to show that the higher P5-P8 signal consistently measured by experiments is a fundamental property of rectangular waveguides and not exclusively due to variations in the secondary electron yield of the surface due to differences in processing (as suggested in Section 5.2.3). The higher signal measured may well be due to the observed accumulation of electrons towards the sidewall of the waveguide (as described above). It is however notable that the MAGIC simulations also show that the signal from P6-P7 is much lower than P1-P4, while in the experiments the signal from P6-P7 was often greater than that from P1-P4 (but always lower than P5-P8 as discussed above). This tends to support the theory that the secondary electron yield of

the surface is indeed uneven due to uneven processing of the waveguide, but that the higher current present near the waveguide wall may indeed be a fundamental property of multipactor in rectangular waveguides.

## **6 Multipactor suppression**

### **6.1 *Modifications to the electron trajectories***

#### **6.1.1 Static longitudinal magnetic fields**

##### **6.1.1.1 *Static magnetic field in TW mode***

RF transmission of power down a waveguide relies on the propagation of electromagnetic waves. Static electric or magnetic fields in no way affect the transmission of RF power (unless the addition of the static and RF fields lead to voltage breakdown or other high field phenomena). Static perturbations can affect the trajectories of free electrons in the waveguide, and can therefore allow the suppression of multipactor by ensuring that no trajectories leading to electron multiplication exist.

Static electric fields have already been shown to be effective in suppressing multipactor in the case of coaxial waveguides [39, 46]. In that case, the electric field is applied between the central and outer conductor of the waveguide. In a rectangular waveguide, however, there only is one conductor, preventing the easy application of a similar solution. It may be possible to apply electric field perturbations by having small coaxial antennae opening into the waveguide.

Static magnetic fields, however, are relatively easy to apply. In the WG1 experiment, an axial magnetic field could be applied by passing current through a coil wrapped around the waveguide body (as can be seen in Figure 27). The field generated by the coil was measured using a hand held gauss meter. It was found to be relatively uniform and its axial component was dominant over any transverse components. The fields corresponding to given coil currents were calibrated using the gauss meter. A positive  $B_z$  indicates a magnetic field in the RF wave propagation direction; a negative  $B_z$  indicates the opposite.

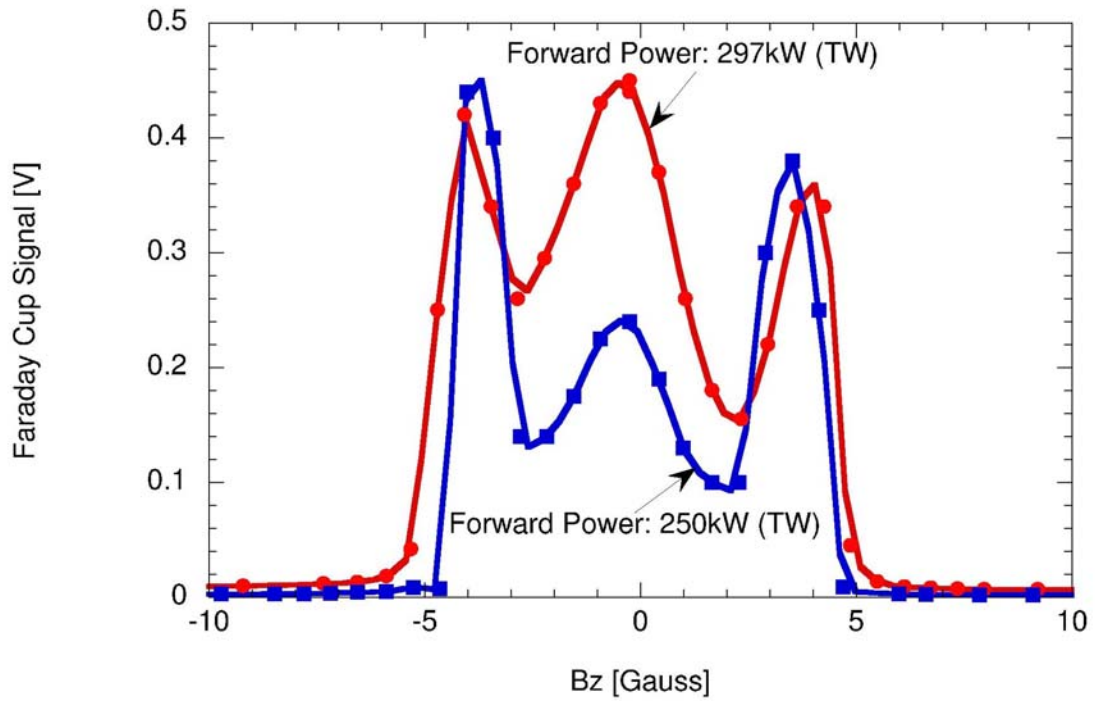


Figure 74: Effect of a solenoid field on the multipactor current measured at 250kW and 297kW by the EEA

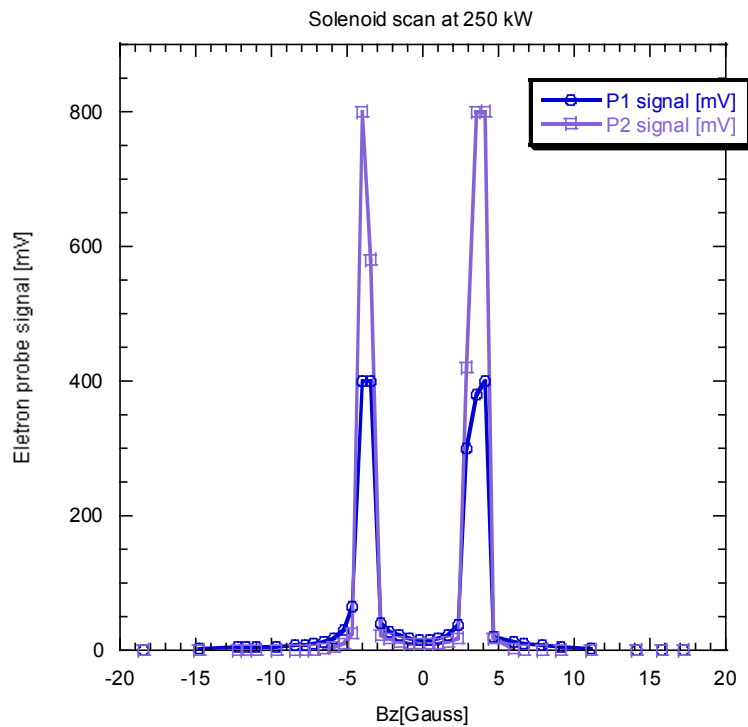


Figure 75: Electron current measured on broad (P2) and sidewall (P1) with varying magnetic fields, showing a strong +/-4G spike as measured by the two different  $e^-$  probes.

An axial magnetic field were expected to have the effect of bending the electron away from the wall to wall trajectory multipacting electrons adopt in an unperturbed waveguide. Given a starting multipactor current at 0G, applying the field would in theory lead to a decrease in multipactor current. The experimental results are shown in Figure 74, Figure 75 and Figure 76. Figure 74 and Figure 75 show the effect of the field at given RF power levels.

Both figures show a clear symmetry, which is to be expected given that the system is largely symmetrical (only the direction of propagation of the RF wave and the resulting electron drift imposes a favoured direction). Figure 74 also clearly illustrates the decrease in electron current as the field increases. A field of only 6G leads to total multipactor suppression for the power levels studied here. The field for which suppression is achieved will be denoted  $B_s$ . As Figure 76 shows, a field of 10G is sufficient to suppress multipactor even at higher power levels.

## Summary of the solenoid field effect (TW)

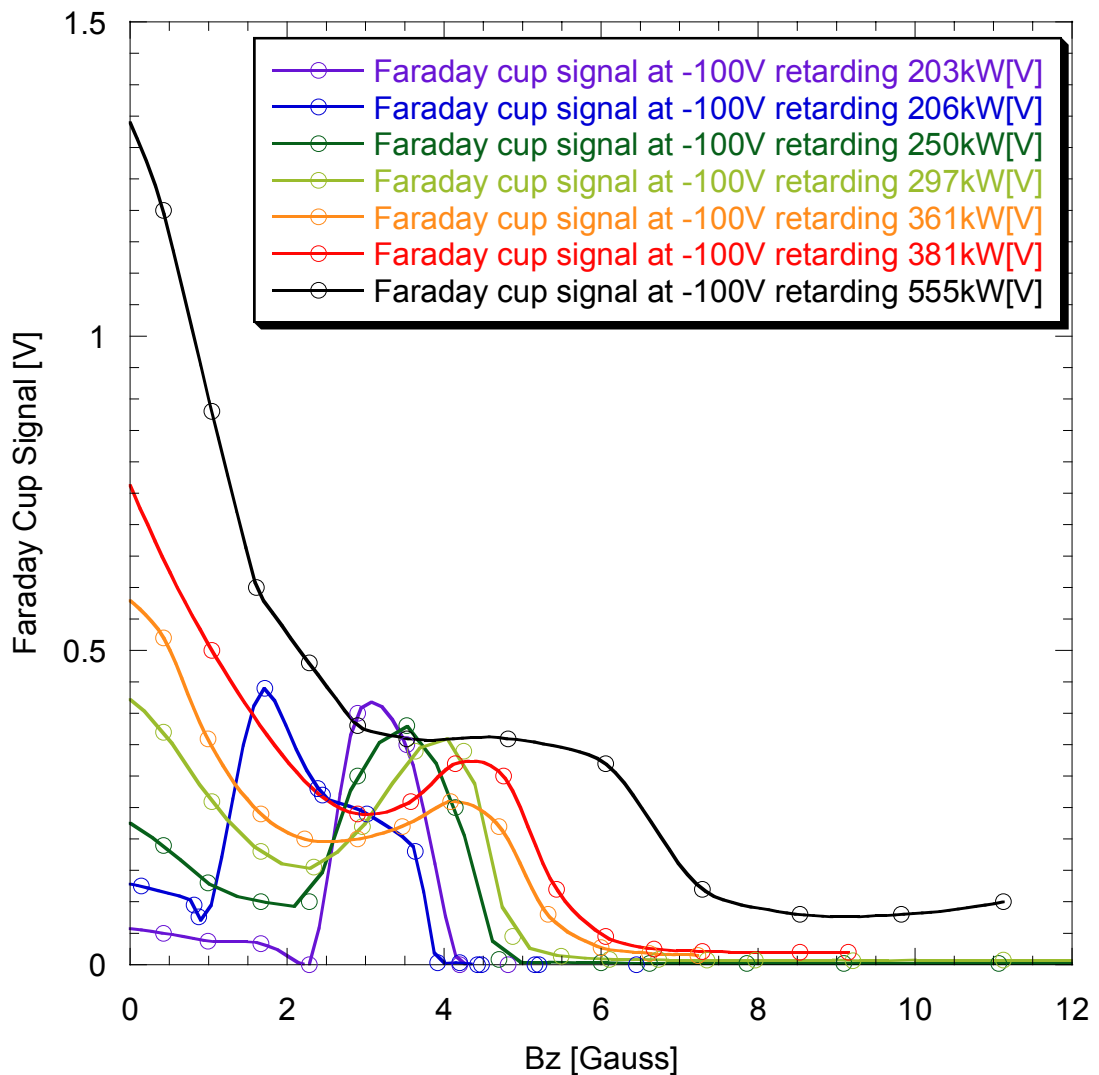


Figure 76: Effect of the bias field (as measured by the EEA at a retarding potential of 100V)

What was not expected are the spikes at or around 4G that appear on the figures, most prominently on Figure 75. There, while the 0G multipactor current was very low, the field around 4G led to a greatly increased multipactor current. The reason for this was found to be the magnetic bias itself. Without magnetic field, the multipactor current develops between the centres of each broad wall, with electron impacts normal to the surface. With a bias field, however, the trajectories are progressively bent away, introducing a transverse component to the electron motion (shown by a MAGIC simulation in Figure 78). As the secondary electron yield of surfaces is strongly dependent on the incidence angle of the primary electrons, an insufficiently strong bias field can enhance multipactor. The problem is compounded by the fact that with a bias field, the electrons impact on areas of the waveguide that have not been processed as thoroughly as the main

multipactor region (the centrelines of the broad wall). This leads to additional out-gassing and higher secondary electron yields due to lower surface cleanliness.

### 6.1.1.2 Analysis of the critical bias field

The critical field at which total multipactor suppression is achieved is therefore very important. The bias field at which the electron trajectory is just crossing between the broad walls and for which the enhancement is maximized by glancing incidence is thereafter called the critical bias magnetic field and denoted  $B_z^*$ . A simplified model has been developed by Rongli Geng [47] to correlate  $B_z^*$  and the forward powering the TW mode. The underlying assumption of the theory is that the multipacting electron moves at a constant speed, which is the time average of its actual sinusoidal velocity. This assumption is later shown to be reasonable as a first approximation. By equating the cyclotron radius of the hypothetical steadily moving electron with the narrow dimension of the waveguide, the following equation is derived for  $B_z^*$ ,

$$B_z^* = \sqrt{\frac{4\mu_0 P_f}{k\omega ab^3}} \quad (1)$$

where  $P_f$  is the forward power,  $k$  the wave propagation constant,  $\mu_0$  the permeability of vacuum,  $\omega$  the angular RF frequency, and  $a$  and  $b$  the wide and narrow dimensions of the waveguide respectively.

Inserting the parameters for the CESR type coupler waveguide, the critical bias field in practical units becomes

$$B_z^* [Gauss] = 0.21\sqrt{P_f [kW]} \quad (2)$$

The results of this simple theory, as well as the experimental results measured from the Faraday cup current, are given in Figure 77. Also given in the figure are results of a numerical calculation, for which no “constant speed” assumption is made. The measured results are systematically higher than the theoretical predictions. This may well be explained by the fact that the narrow dimension of the test waveguide was actually smaller than the 4” design value because of wall deflection under the load of the atmospheric pressure. Another theoretical curve for a 3” high waveguide (of the same width) is also given in Figure 77. It can be seen that the experimental results (taken on a

waveguide that had collapsed to a height of 3.625" in the centre) fall reasonably within the constraints set by the theory.

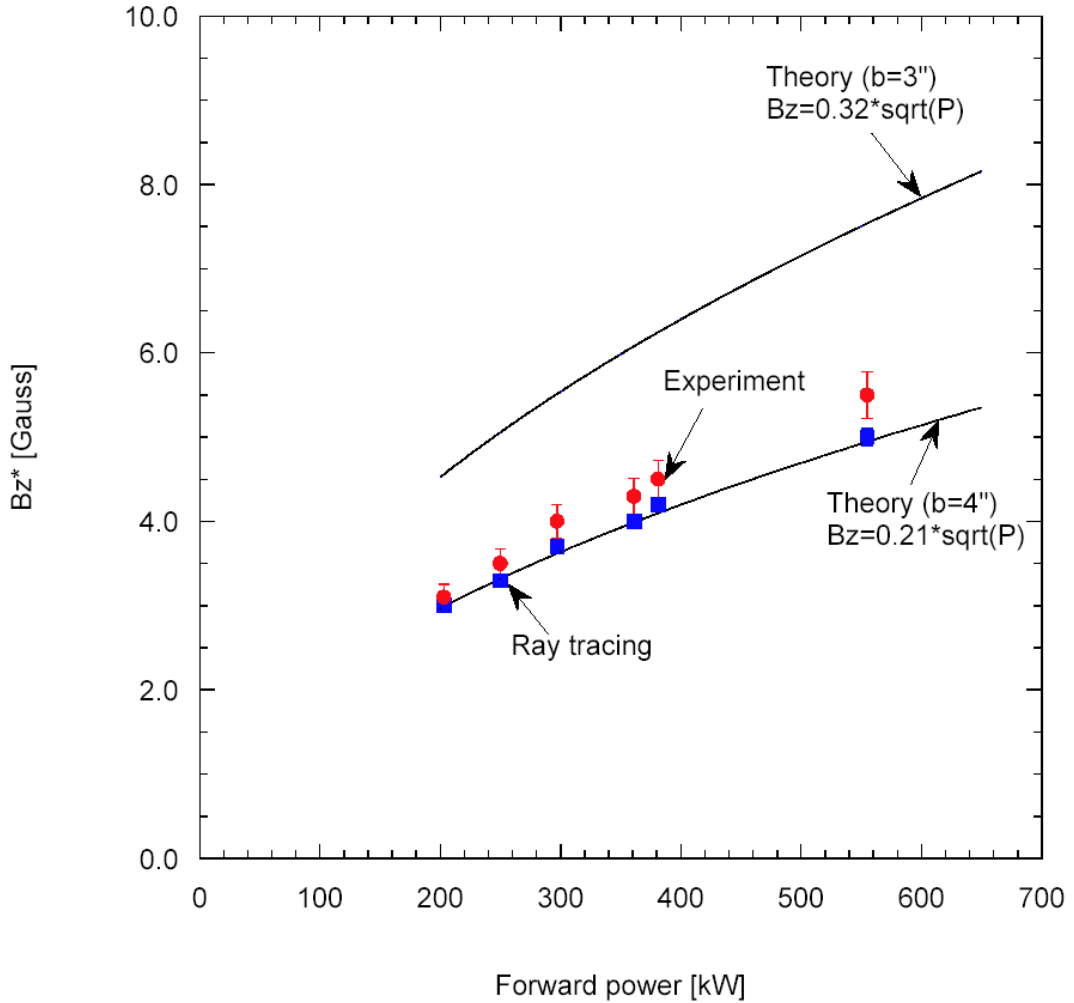


Figure 77: Critical bias magnetic field for a CESR type coupler waveguide. In red solid circles are experimental points, the blue solid squares denote numerical calculation from Xing; the black lines show the theory for two waveguide gaps.

At bias fields higher than  $B_z^*$ , multipacting quickly becomes suppressed. A value above  $2B_z^*$  was experimentally found to be sufficient to achieve total multipactor suppression. Ultimately, a simple formula for the suppression magnetic field,  $B_s$ , is:

$$B_s = 2B_z^* = 4\sqrt{\frac{\mu_0 P_f}{k\alpha ab^3}} \quad (3)$$

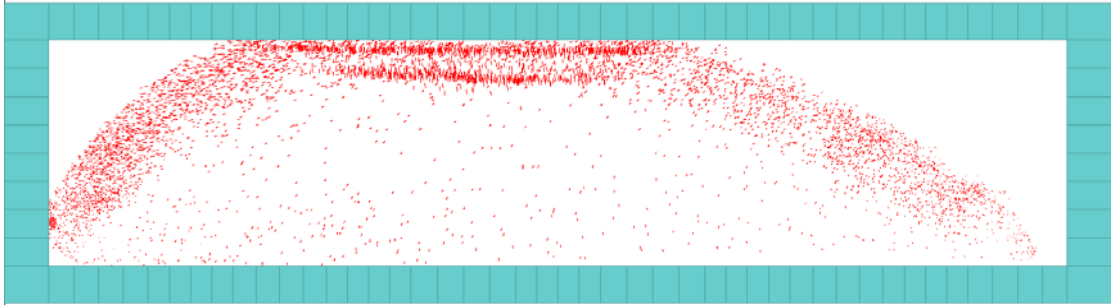


Figure 78: MAGIC simulation at  $B_z=3G$  and 250kW power. This frame is 23ns after the electron emission from the bottom wall.

The figure above shows a simulation of the waveguide with a static magnetic bias field. The first re-emitted electrons are visible just off the top wall. What is also apparent from the short lines representing the velocity of the electron is the glancing incidence at which the primary electrons hit the top wall. A video of the phenomenon shows that more clearly (Included in the attached CD-ROM).

### 6.1.1.3 *Static magnetic bias in SW mode*

The static magnetic bias in SW mode (standing wave, full reflection) was found to be more involved, as shown on Figure 79. Full reflection was achieved by inserting a shorting metal plate across the waveguide between the downstream taper and the load. In contrast with what was observed for the TW mode, no complete multipactor suppression was achieved within the field range we could produce with the coil (-20G to +20G).

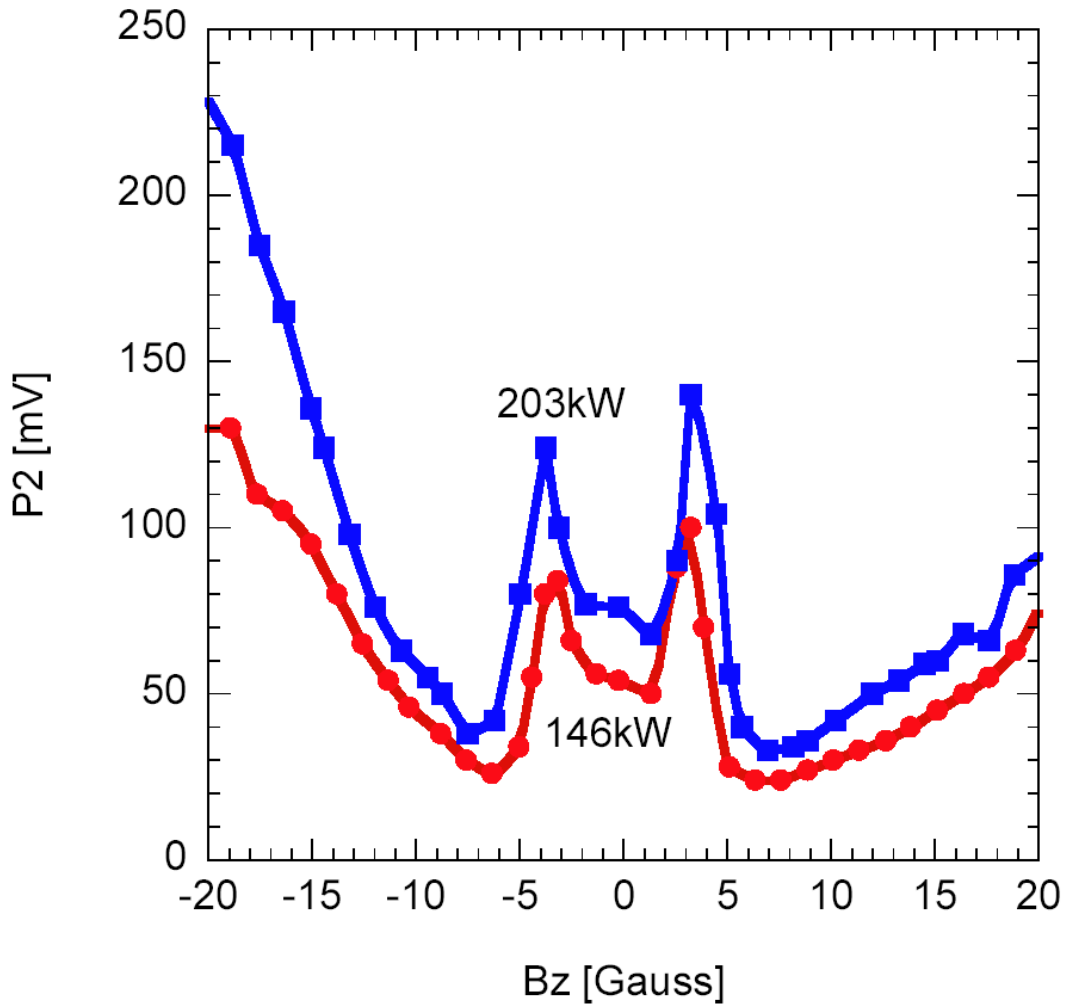


Figure 79: Multipactor current measurement (P2) measurement in SW mode at various bias field levels.

There appears to be a second enhancement peak after the first one at 4G. This effect was also seen in MAGIC simulations conducted with a standing wave and a bias magnetic field of 8G and 20G, where after 160ns of multipacting the accumulated charge was measured to be about ten times greater with a 20G bias than with an 8G bias. From a practical standpoint, one should not be too concerned with its effect on the operation of a cavity input coupler. A coupler waveguide would normally be operated in the TW or possibly a MW mode with very little reflection. The effect observed in SW mode may however be useful in conditioning a waveguide by promoting multipacting in the coupler. In that case, a sliding short would allow the anti-nodes (maximum RF power) to sweep the waveguide.

### 6.1.2 Grooves

Predictions from RL Geng's code, Xing, simulations suggested that stable multipactor trajectories only existed in the plane perpendicular to the centre of the broad walls and parallel to the wave propagation direction. It was surmised that if the electrons in that area could be trapped, multipactor should not be able to develop. A mechanism by which multipactor could be trapped is the use of a groove cut along the centreline of the broad wall. The groove needs to be deep enough to trap electrons entering it into an area with no field. It also needs to be narrow enough to minimise field leakage, yet its effectiveness also depends on its width so as to trap as many electrons as possible.

The groove concept was first tried in WG2, which had an opening cut into the side allowing the insertion of a grooved bar. The insert is approximately 1cm wide and can be fitted with various bars. It was first fitted with a grooved copper bar as shown in Figure 80. The slot on the bar was 0.5cm wide.

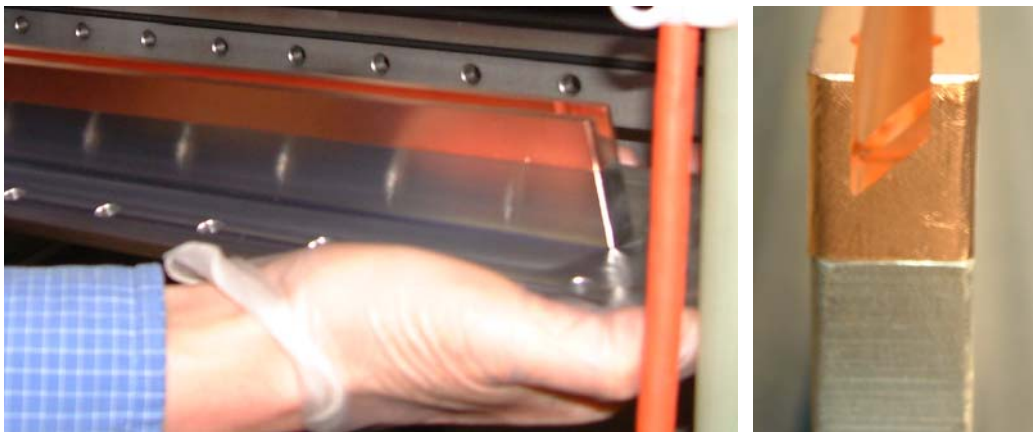


*Figure 80: Copper groove for WG2 (with the profile of the slot in the bar)*

The profile of the groove was chosen to minimise the escape of primary and secondary electrons. The design incorporated an angle so that the majority of secondary electrons emitted by the bottom would hit the sidewall of the groove.

The groove did not prove to be quite as efficient as the simulations had predicted. Indeed, it was apparent even before this that they were insufficient to fully describe real multipactor, as the sidewall probe picked up a disproportionate amount of current (more current than the broad wall probes once the waveguide had been processed). Measurements with WG2 showed that in equivalent conditions, the current picked up

with a groove fitted in, as opposed to the case where a flat copper insert was used, is reduced by approximately fifty percent (instead of the full multipactor suppression that was predicted). However, the probes were located in the middle of the broad wall, so the measurement of the current in that particular location may not have been the best way of evaluating the efficiency of the groove. Measurements taken with WG3 had probes off-centre and allowed a better evaluation of the effectiveness of the groove. Results from WG3 are discussed later in this section.

Several pictures of the flashes that occur during breakdown were taken from the view-ports at the end of the waveguide bends. The best picture of such an event is shown on Figure 81. Note the darker area in the middle of the waveguide where the groove is located. A picture of the waveguide taken from the same viewpoint is also shown for comparison. The groove can be seen on the right side, its reflection is visible on the left hand wall of the taper.

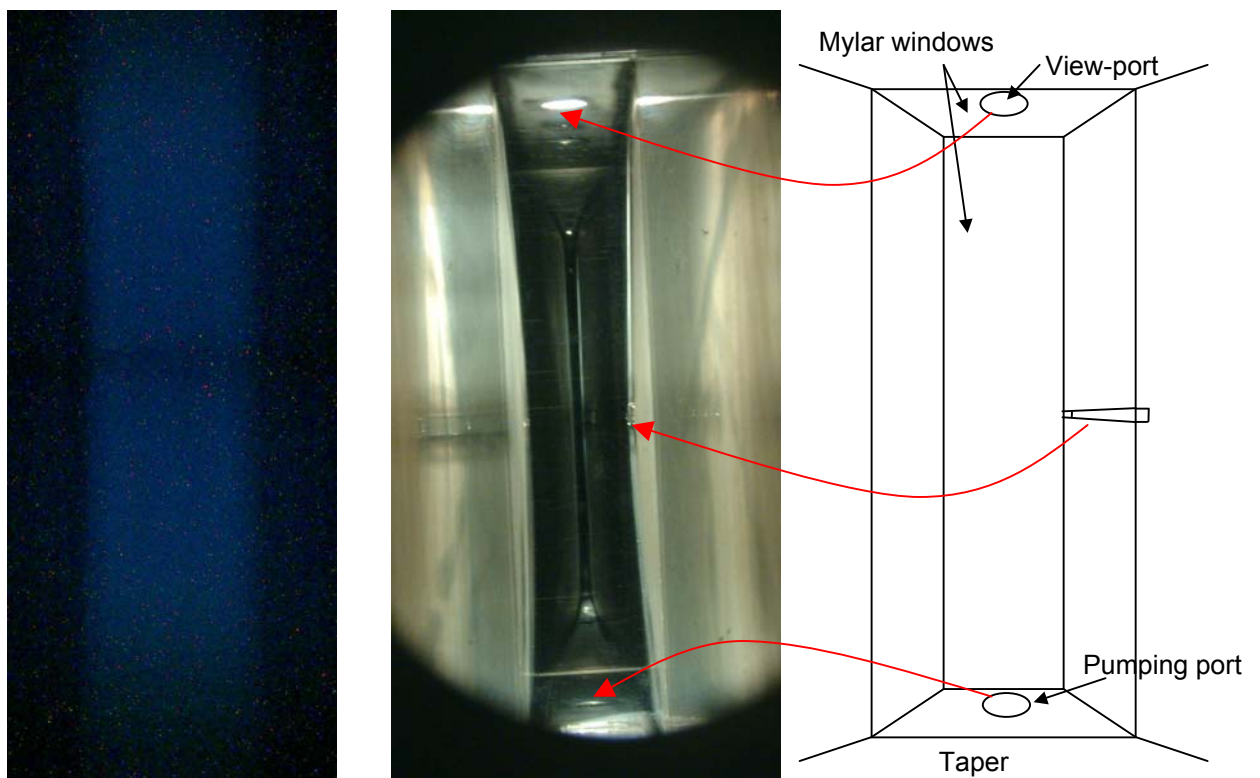
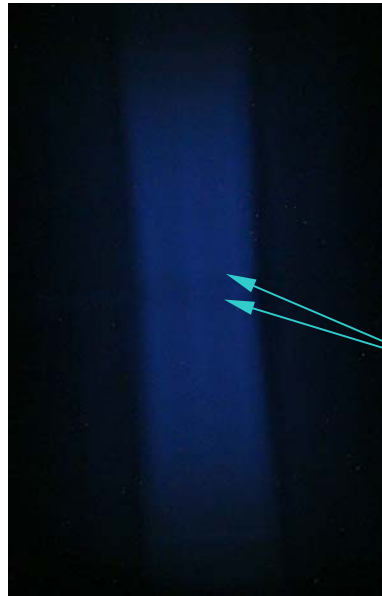


*Figure 81: Picture of a breakdown event in the grooved waveguide, also showing the waveguide interior from the same viewpoint (with a schematic representation of what is seen in the pictures).*

Surprisingly, an aluminium bar showed less multipacting current than the copper bar. The best explanation that we have found so far is that clean aluminium has a very low secondary electron emission coefficient (similar to that of many other clean metal

surfaces including copper), whereas aluminium oxide has a high one, explaining the generally high measured values of secondary electron yield for aluminium (this however conflicts with the observations on the Al plate discussed in section 5.1.3).

Figure 82 is a picture of a breakdown event that occurred with the aluminium bar. Note the small darker areas where the small (~0.6mm) gaps between the bar and the waveguide walls are. The multipactor suppression given by such small gaps was not measurable.



Gaps between the wall and the insert have an effect on the flash, suggesting that the light seen corresponds to actual electrons travelling in the waveguide.

*Figure 82: Picture of a breakdown event with the aluminium bar insert*

Further grooved waveguide experiments were carried out with WG3. In that waveguide, the grooves were cut into the Cu sample plate. The experiments began with a small (5x5mm) copper bar fixed onto the sample plate (pictured in Figure 83). The purpose of the bar was to disrupt the RF fields in the vicinity of the centre of the waveguide.

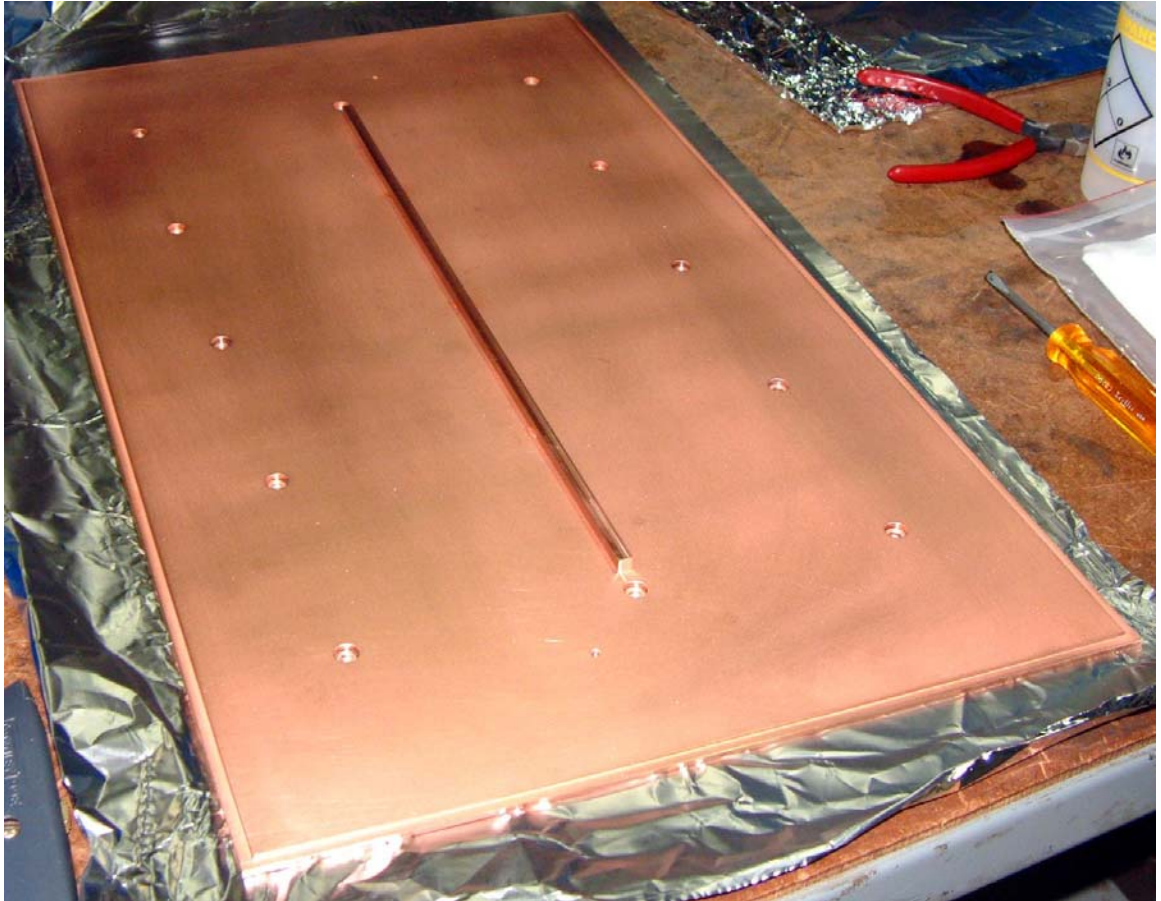


*Figure 83: Copper sample plate with bar.*



*Figure 84: Picture of a discharge with a Cu bar (speckles are the result of noise in the camera)*

The set-up was conditioned and measurements made. They compared very favourably with those carried out on a plain copper plate, as can be seen on Figure 87, looking at the values of P1-P4 (on-axis probes) for cases with and without a bar. No adverse effect

(sparks, excessive reflected power) was observed while using the bar. The bar helped shorten the processing time and lowered the overall multipactor levels. The bar did not, however, suppress multipactor completely. The graph that can be plotted from such measurements is shown on Figure 86. It shows very low voltages (measured across a  $10\text{k}\Omega$  resistor, therefore  $10\text{mV} = 1\mu\text{A}$ ) for the centremost on-axis probes, P2 and P3 (see Figure 85 for the location of the probes on the waveguide wall). The probes receiving the most current were P5 and P8, which are furthest from the centre-plane of the waveguide. An explanation for this were given in Section 5.2.3, where it was suggested that the waveguide walls were unevenly processed by multipactor which is initially at its strongest in the centre of the waveguide, and where the electron energies are the highest. The probes receiving the least amount of current were P2 and P3, which are the ones directly opposite the ridge. P1 and P4, while on the axis of the waveguide, were beyond the ends of the ridge and therefore measured a current equivalent to a ridge-less waveguide.

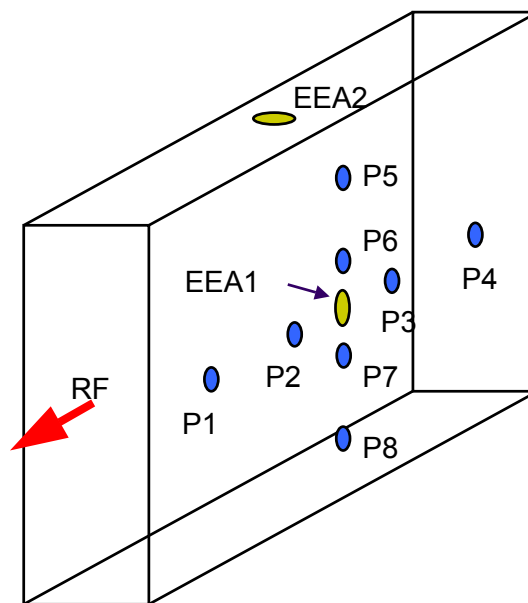


Figure 85: Layout of the probes on the waveguide

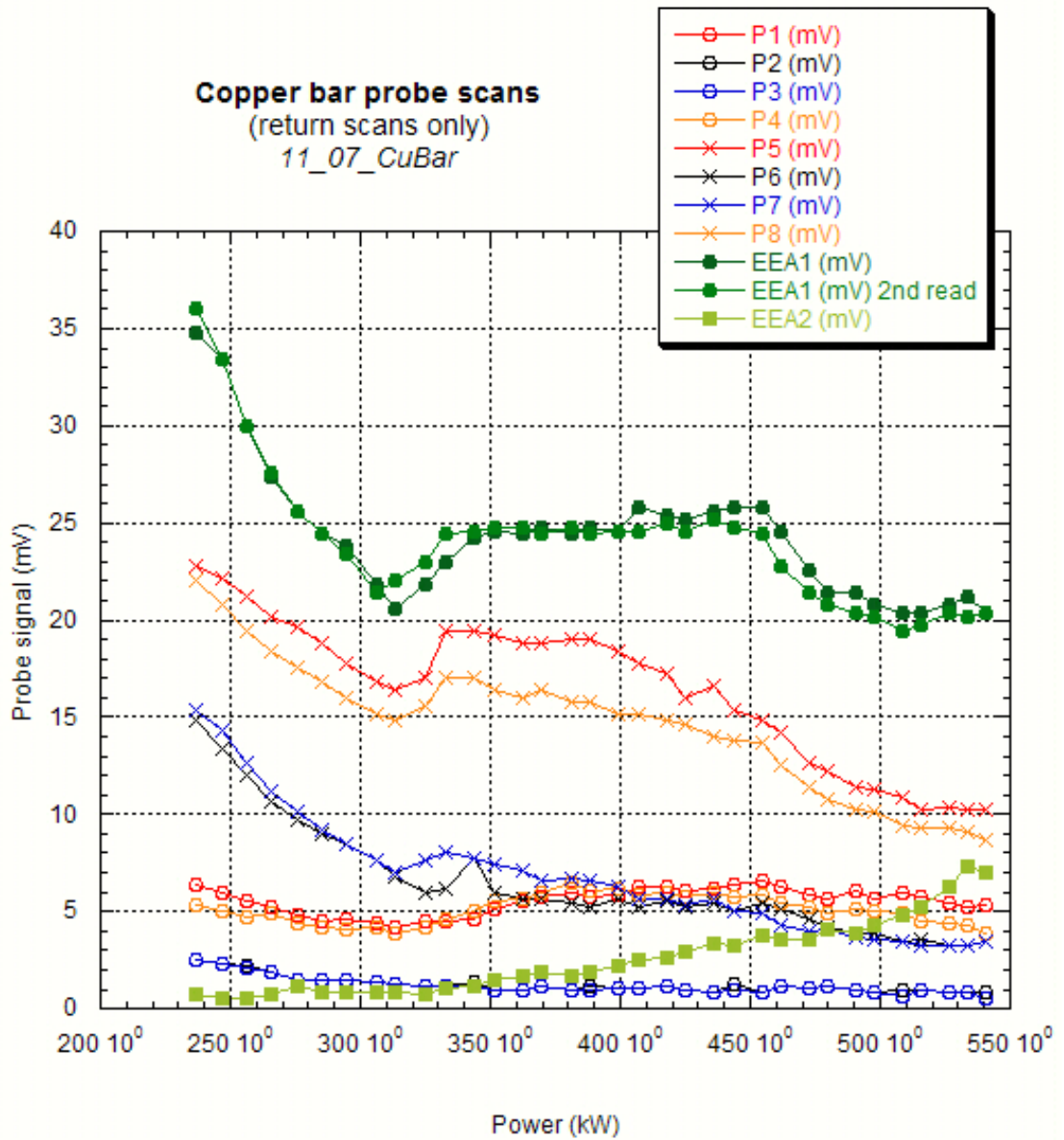


Figure 86: Measurement results with copper plate and bar (in mV across a 10kΩ resistor)

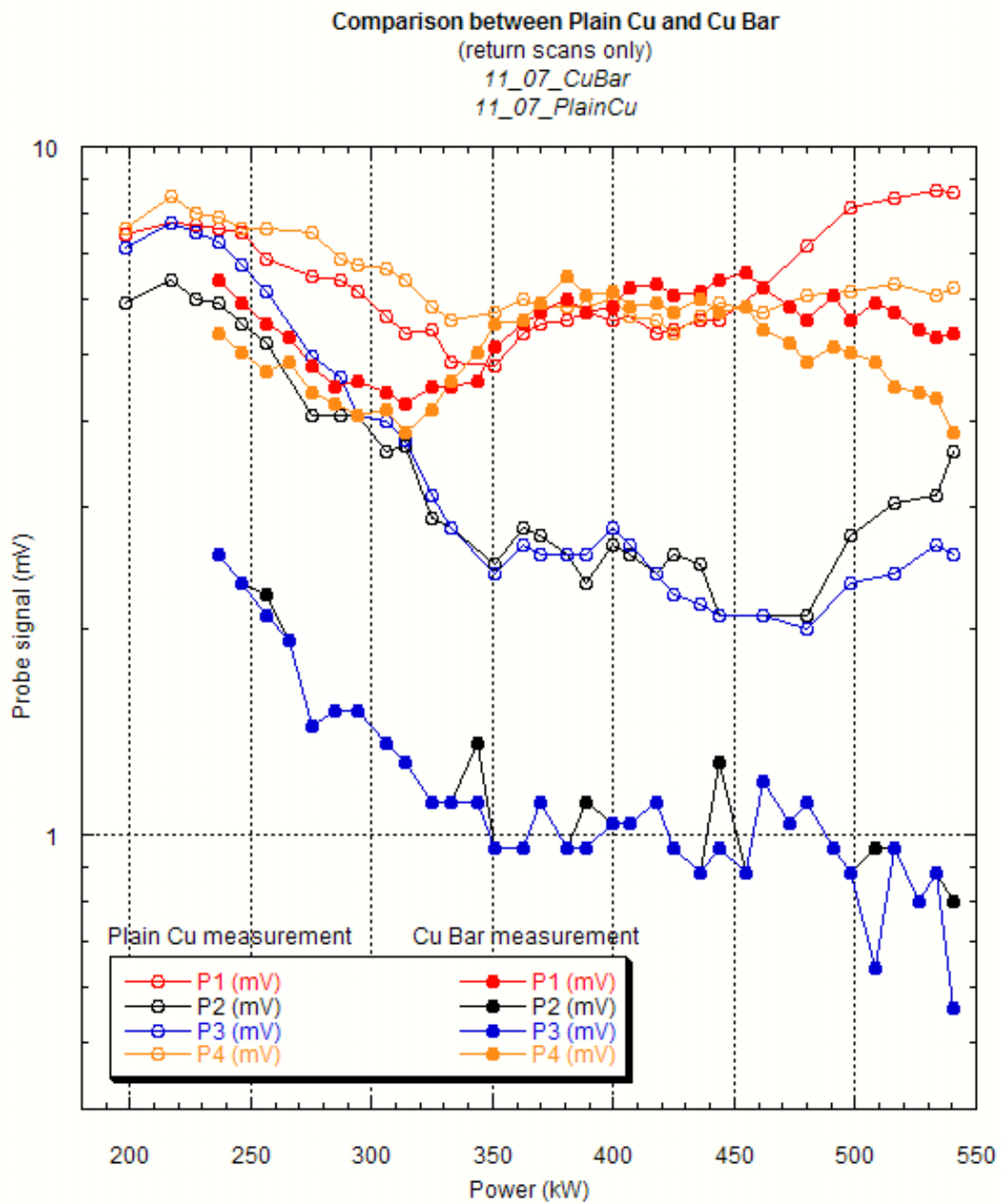


Figure 87: Comparison between measurements of the on-axis probe signal with and without the bar. This plot is plotted as a logarithmic plot to highlight the differences in signal picked up by the same probes in the two cases.

Comparison between Plain Cu and Cu Bar  
 (return scans only)  
 11\_07\_CuBar  
 11\_07\_PlainCu

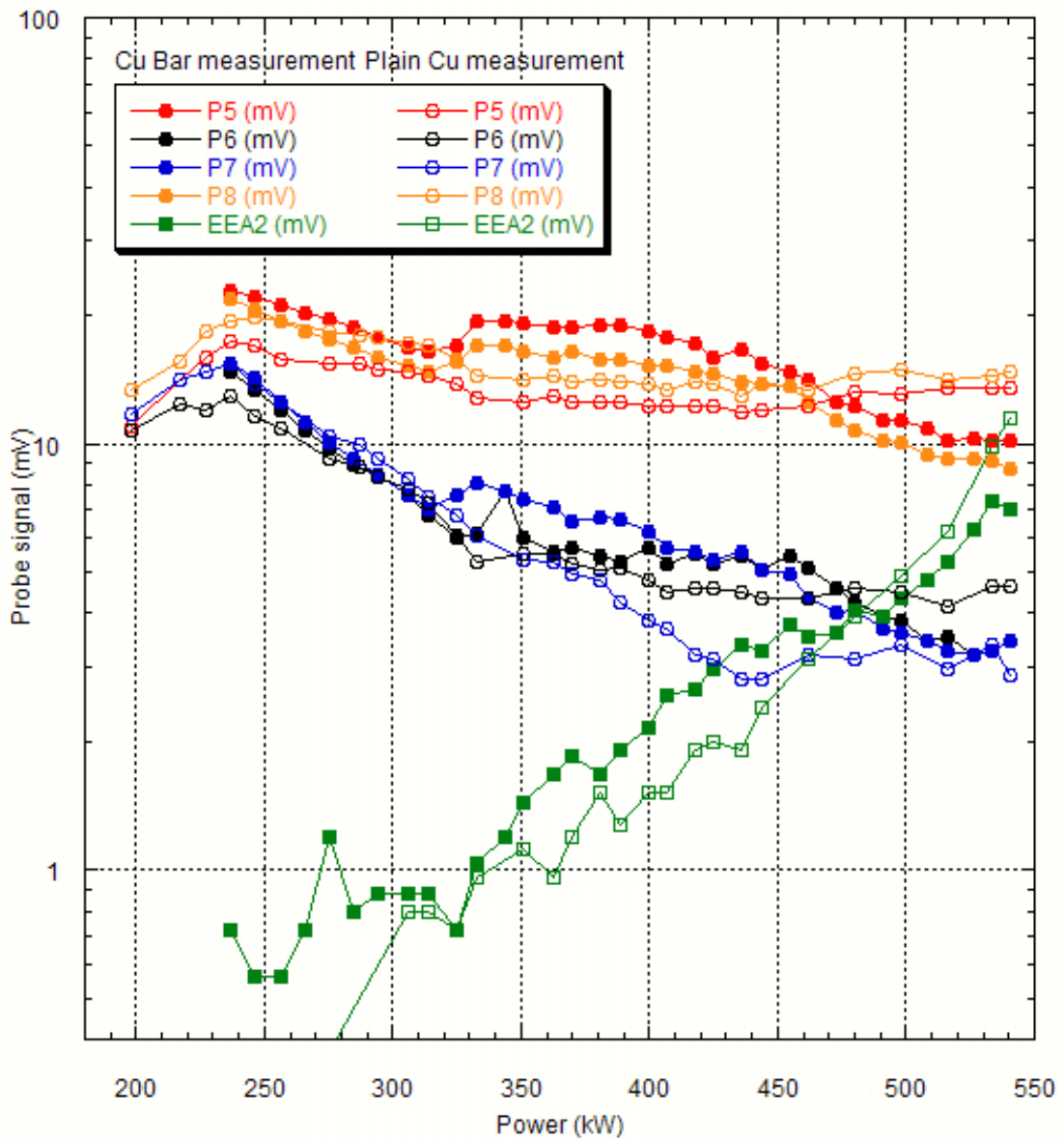
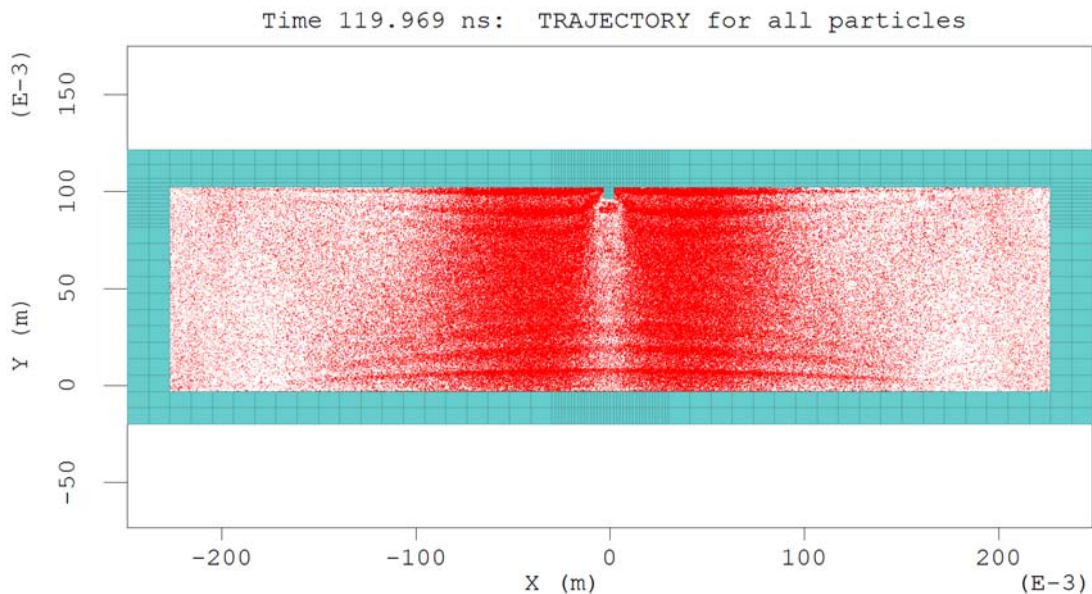


Figure 88: Comparison between measurements of P5-P8 and the sidewall EEA with and without the bar.

Figure 87 shows that though the bar is successful in reducing multipactor in the centre of the waveguide (probes P2 and P3 being the best indicators), the overall level of activity is very much the same as when a simple sample plate is studied (as shown by the measurements from EEA2 (Figure 88), which picks up the background electron ‘splash’, i.e. those electrons not directly involved in multipactor). Curves from P5 and P8 (situated on either side of the centreline, 85mm away from it) show very similar levels of current,

indicating that the most intense electronic activity is located in this area (even in the bar-less case).

MAGIC simulations also pointed towards the effectiveness of the bar as a way of disrupting multipactor in the centre-plane of the waveguide. A snapshot of the electron positions in the waveguide after 120ns of simulation is shown in Figure 89.



*Figure 89: Status of the MAGIC simulation after 120ns (a photograph of the experimentally observed situation can be seen in Figure 84)*

However, much like the experimental waveguide, the simulations did not lead to complete suppression of multipactor and also indicated similar rates of electronic build-up between cases with a ridge and cases without (accumulated charge measured at 5.25 (arbitrary units) with a ridge and 5.4 (AU) without, after 80ns of simulated multipactor).

Once the bar test had been completed, tests were carried out on a single groove (cut into the same sample plate, as shown in Figure 90). The groove did not, as was case for the groove in experiments from WG2, suppress multipactor completely. Instead, the effectiveness of the groove was very similar to that of the bar as far as multipactor suppression was concerned, as is shown on Figure 93.

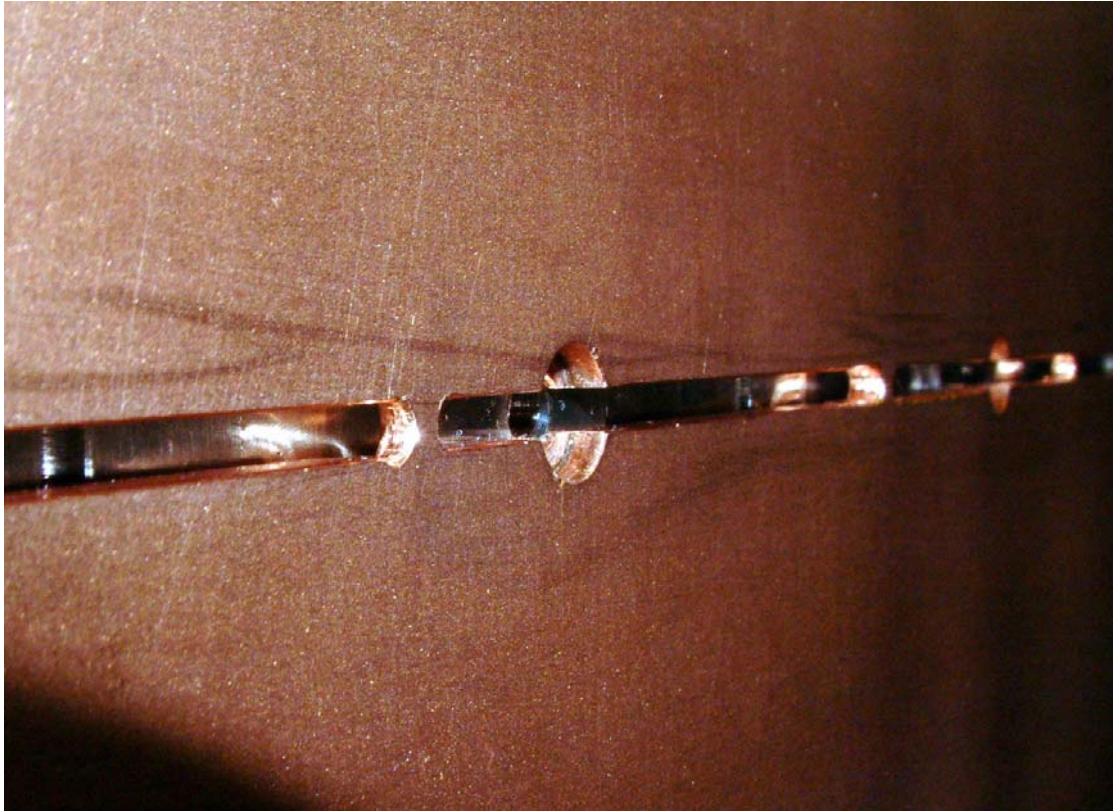


*Figure 90: Close up of the single groove. Bridges were left across the groove so as to minimise the impact of the groove on RF and structural strength. The groove was cut through the sample plate, opening onto the cooling plate behind it.*

A logical next step, given that a single groove did not, on its own, suppress multipactor, was to add grooves next to the first and cover more of the wall surface. This was done with five, then thirteen grooves. In the last case, the grooves covered the central third of the waveguide width. The grooves were 1cm apart and covered over 40cm in length on the sample plate.

Neither the five nor the thirteen groove case suppressed multipactor completely; instead, it appeared to be worse than with a single groove or bar. A comparison of the results from the various grooves can be seen on Figure 93. The reason for the failure to help multipactor suppression is likely to be that the off-centre grooves, by intercepting wall current, lead to the creation of tangential electric fields. This would have the effect of completely modifying the surface fields and therefore the development of multipactor in the waveguide. A plot of the fields created by thirteen grooves is given in Figure 94.

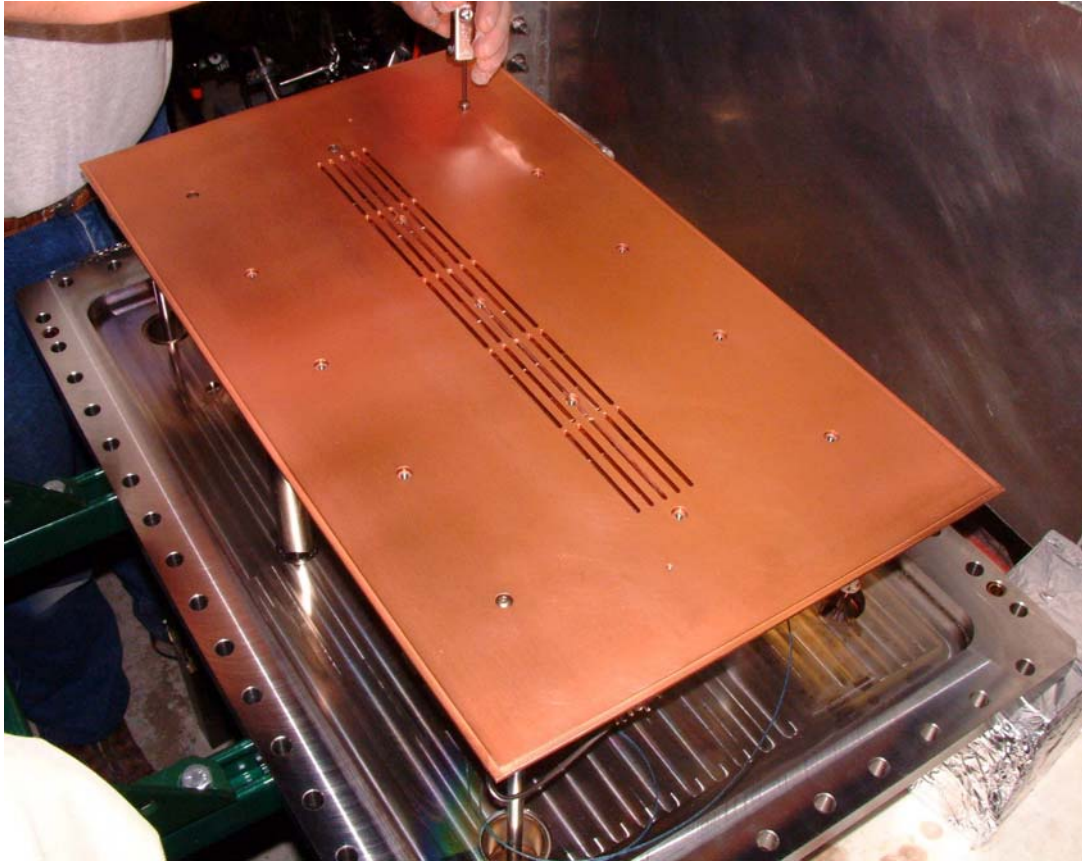


*Figure 91: Copper plate with five slots, mounted on the flange*

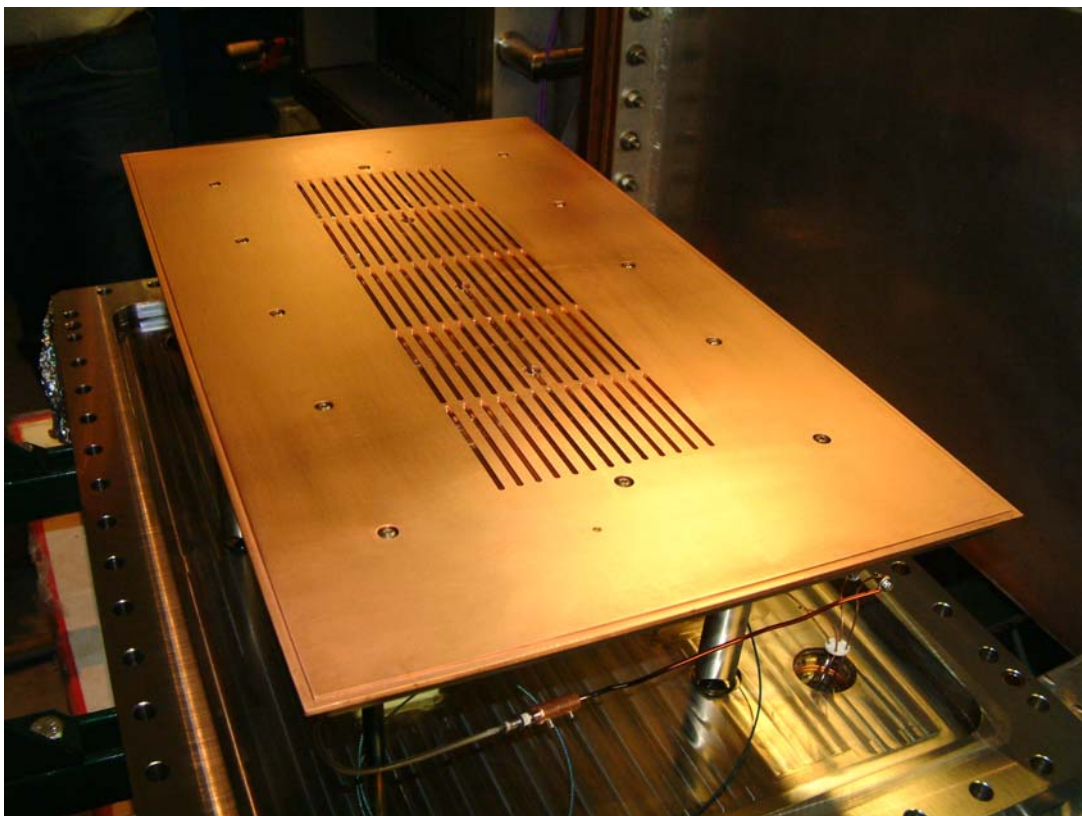


*Figure 92: Copper plate with 13 slots*

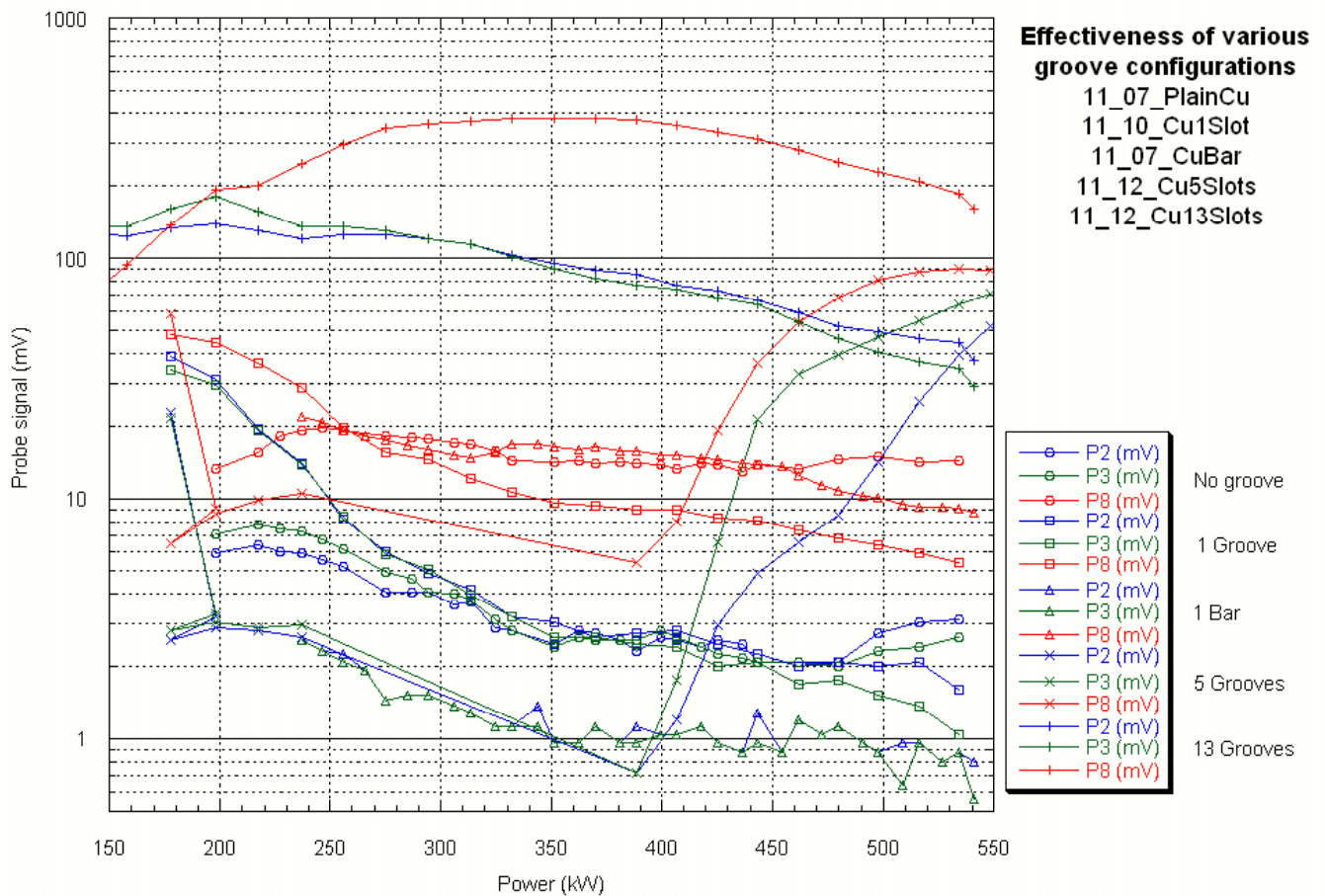


Figure 93: Summary of the grooved waveguide results. P2 and P3 are on the centre-line of the waveguide, P8 is near the sidewall.

As is apparent from the figure above, having thirteen grooves is never an advantage, as the current is some ten times greater than with no grooves. The multipactor onset level is also lower than the other cases. Having five grooves is also not an advantage at most power levels, particularly at higher power levels where their effect is detrimental. There is however a gap between 240kW and 380kW where no current could be measured since it was below the measurable threshold (the plot on Figure 93 only shows the second scan across the power range, the first pass showed a dip in measured current but no extinction in the 240-380kW range). Multiple grooves (or bars) may still prove to be effective in certain circumstances, but these experiments show insufficient multipactor suppression for the reasons given above.

The single slot and the bar gave results that were quite similar. The bar led to a greater reduction of current in the centre of the waveguide (as measured by P2-P3), while the groove led to slightly lower general multipactor activity than the bar (as measured by P8).

Neither case was worse than the plain sample plate, at any power level. The conclusion from these experiments would be that a groove or bar does not harm the operation of the waveguide, and has a positive effect on multipactor suppression. The bar in particular has the additional advantage of being easy to manufacture and install.

CST Microwave Studio simulation of the 13 groove waveguide showing  $E_x$

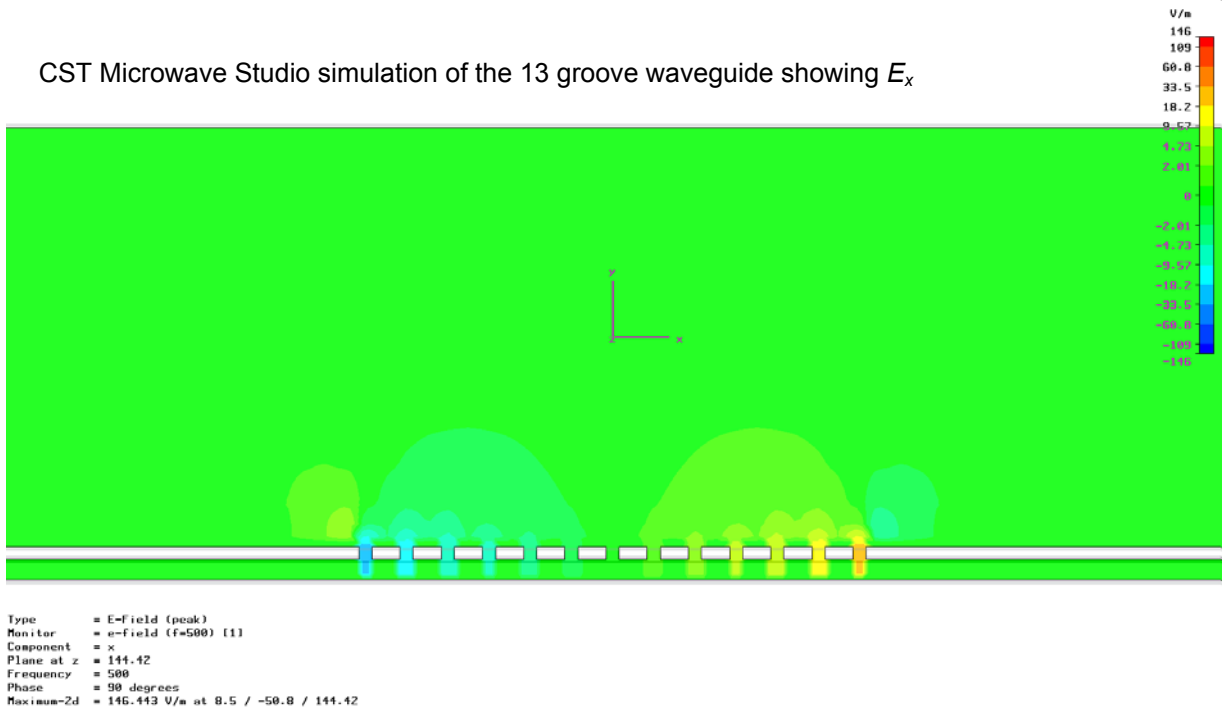


Figure 94: CST Microwave Studio simulation of a 13 groove waveguide with a gap under the sample plate, showing the  $E_x$  component of the electric field

## 6.2 Modifications to the electron yield

### 6.2.1 Coatings

Coatings have often been used in the past to help solve breakdown problems, in particular on vacuum windows. Most vacuum window ceramics have a very high secondary electron yield (for alumina,  $\delta \approx 12$ ), requiring the application of an anti-multipactor coating to reduce the surface yield. The coating the most commonly applied in this case is titanium nitride (TiN).

Coatings could also be used to limit multipacting in a waveguide. Several possibilities exist to limit the secondary electron yield of the surfaces. Shown on Figure 17 are the measured electron yields of TiN and various other common accelerator materials. A graph of the yield of TiN at various activation temperatures is shown on Figure 35 and of a TiZrV non-evaporable getter material is shown on Figure 36.

Several measurements were taken of TiN and TiZrV coated sample plate inserts before and after activation of the surface by heating to more than 200°C (250°C for the TiN plate) for several hours. The sample plate was heated using hot air blowing through the cooling channel (shown in Figure 39) as well as the heater wire (shown in Figure 40). The temperature of the sample plate insert could be measured by averaging the read-out from the thermocouples located in the corners of the sample plate holder.

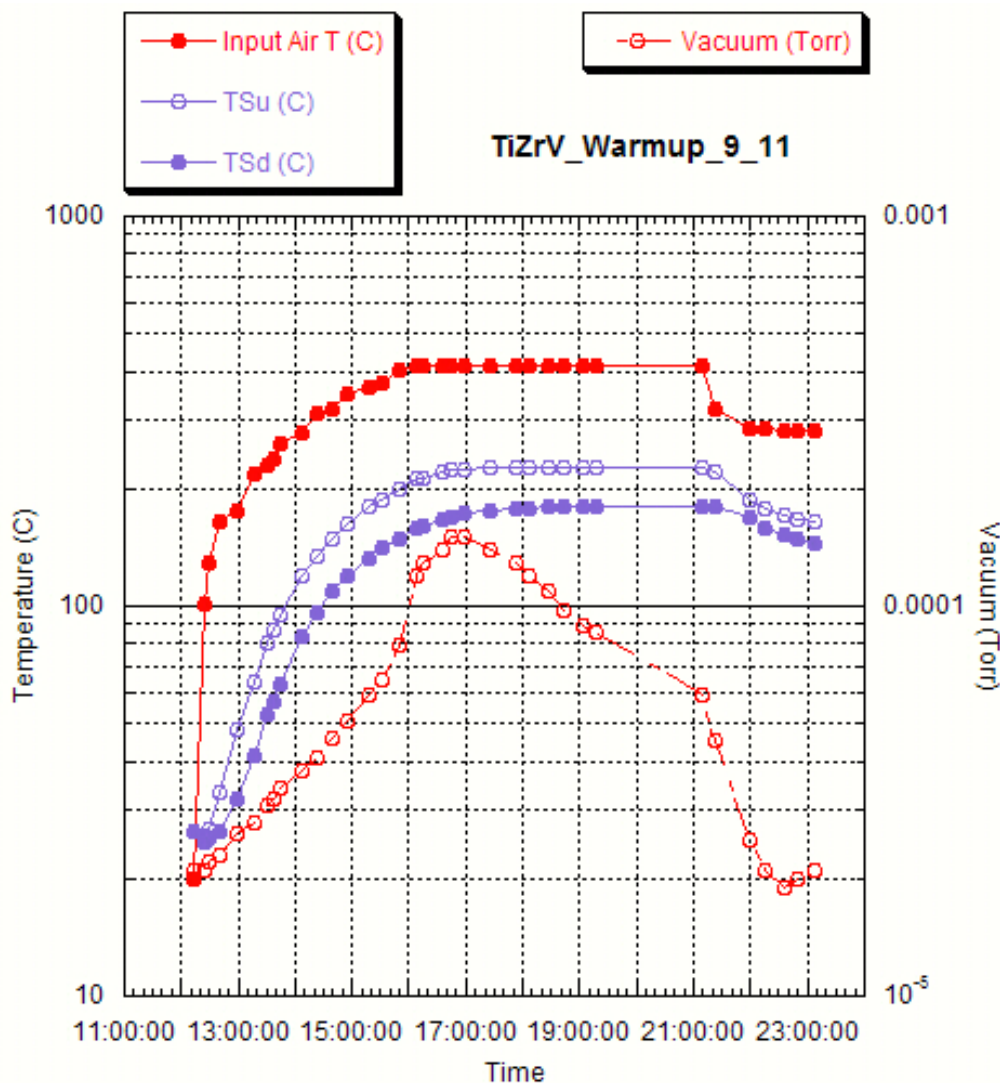
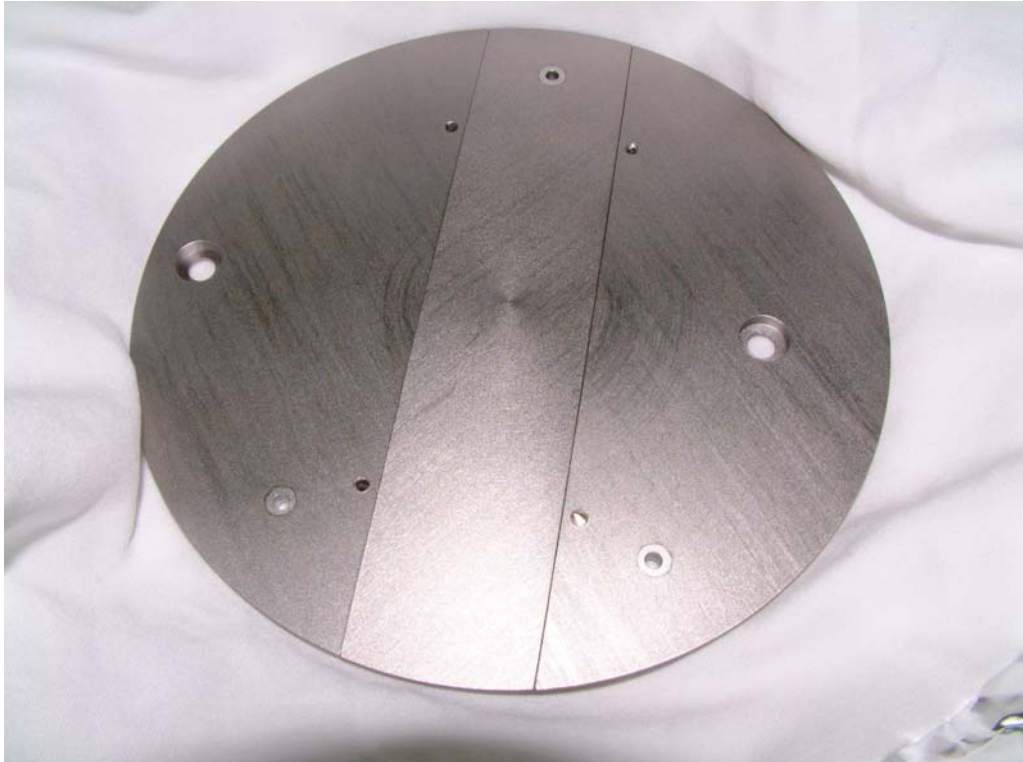


Figure 95: Warm-up temperatures of the sample plate ( $T_{su}$  and  $T_{sd}$  being the upstream and downstream thermocouples respectively on the corners of the sample plate)

The NEG coated sample plate insert was prepared by Dr. Yulin Li of Cornell University in a DC magnetron sputtering chamber [48]. A strong DC current (typically 600V cathode voltage and 30mA sputtering current) is established between the sample plate sections and strands of twisted titanium, zirconium and vanadium wires in a low pressure argon

atmosphere ( $\sim 2 \cdot 10^{-3}$  Torr). This leads to an arc discharge that ionises the argon (the discharge is kept under control by a control system that varies the voltage to keep the discharge steady). A solenoid magnetic field of approximately 200G increases the collisions in of the system. The bombardment of argon ions onto the surface of the wires releases atoms from the wire surface and coat everything in the chamber with a homogenous layer of TiZrV with a thickness in the order of a micron.



*Figure 96: TiZrV coated sample plate insert. The insert was made of three strips in order to fit into the deposition chamber.*

When we tried it, the NEG coated sample plate did not, by itself, suppress multipacting. One of the reasons for this is simple; the sample plate only covered a small fraction of one surface of the waveguide and whatever effect it might have would not prevent multipactor from occurring in the rest of the waveguide.

To measure the effectiveness of the sample plate, the best method available was to compare the difference between the signals coming from probes P2 and P3. P3 was opposite the sample plate insert, while P2 was opposite the stainless steel sample plate body. EEA1 was also opposite the insert, and electron energies from the sample plate could be measured. These are shown in Figure 67 (page 86; 'TiZrV warm' refers to sample plate temperatures slightly exceeding 200°C, 'TiZrV cold' refers to room temperature measurements). There does not appear to be any difference between the

electron energies measured by the EEA in the presence or absence of the sample plate. This is to be expected as the electrons picked up by the probe have crossed the waveguide due to the influence of the RF; any small variation of emission energy would be drowned out by the much greater energy the RF gives the electrons.

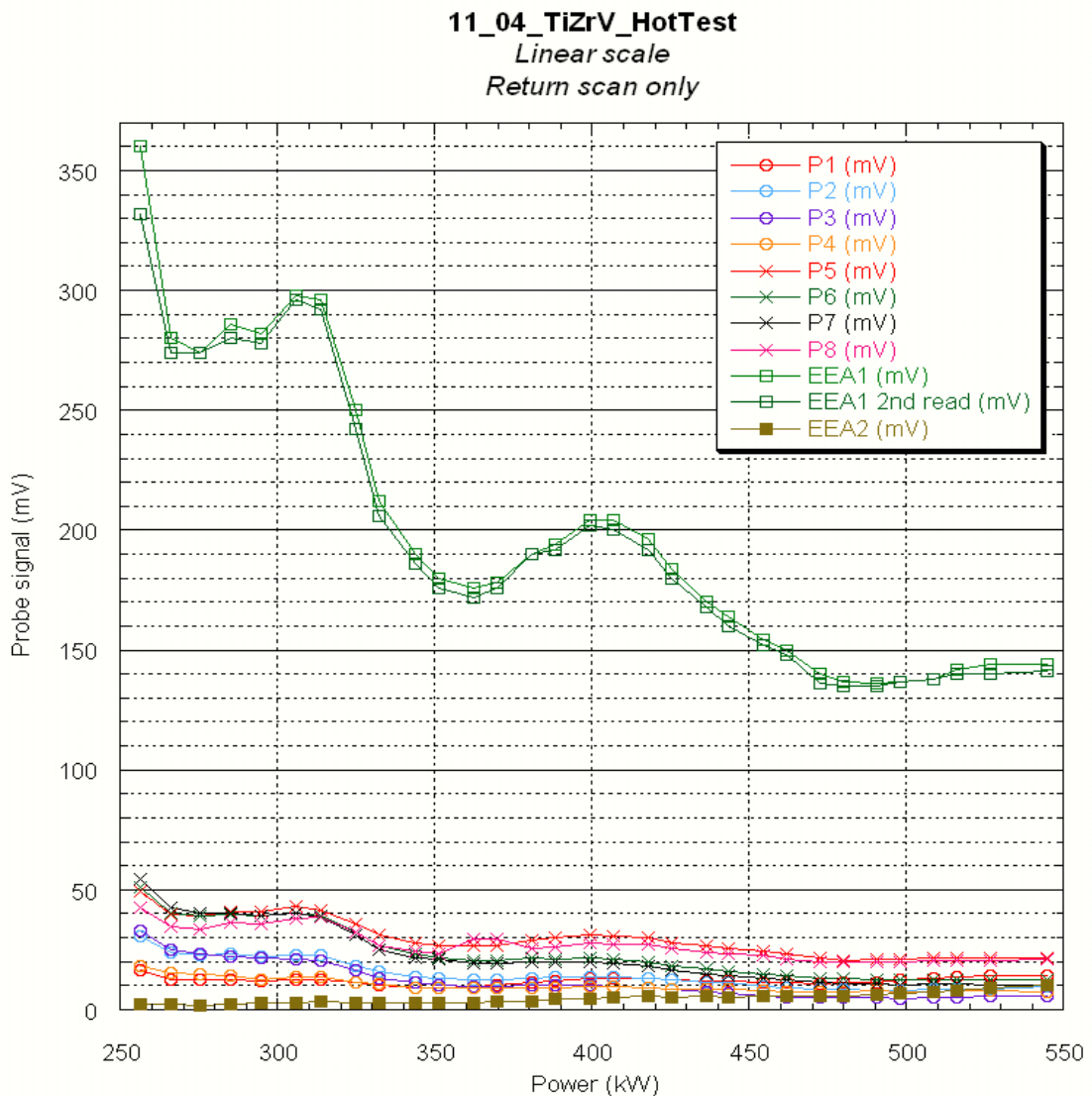


Figure 97: Multipacting current measured with a TiZrV sample plate after heating to ~190 °C for 2h40min.

Measurements using the TiZrV sample plate insert are given in Figure 97 and Figure 98 (only showing the second, 'return' scan through the power range where the processing of the surfaces is the best that could be reached). These are also the clearest measurements taken during the WG3 experiments.

### 11\_04\_TiZrV\_HotTest

Linear scale

Return scan only

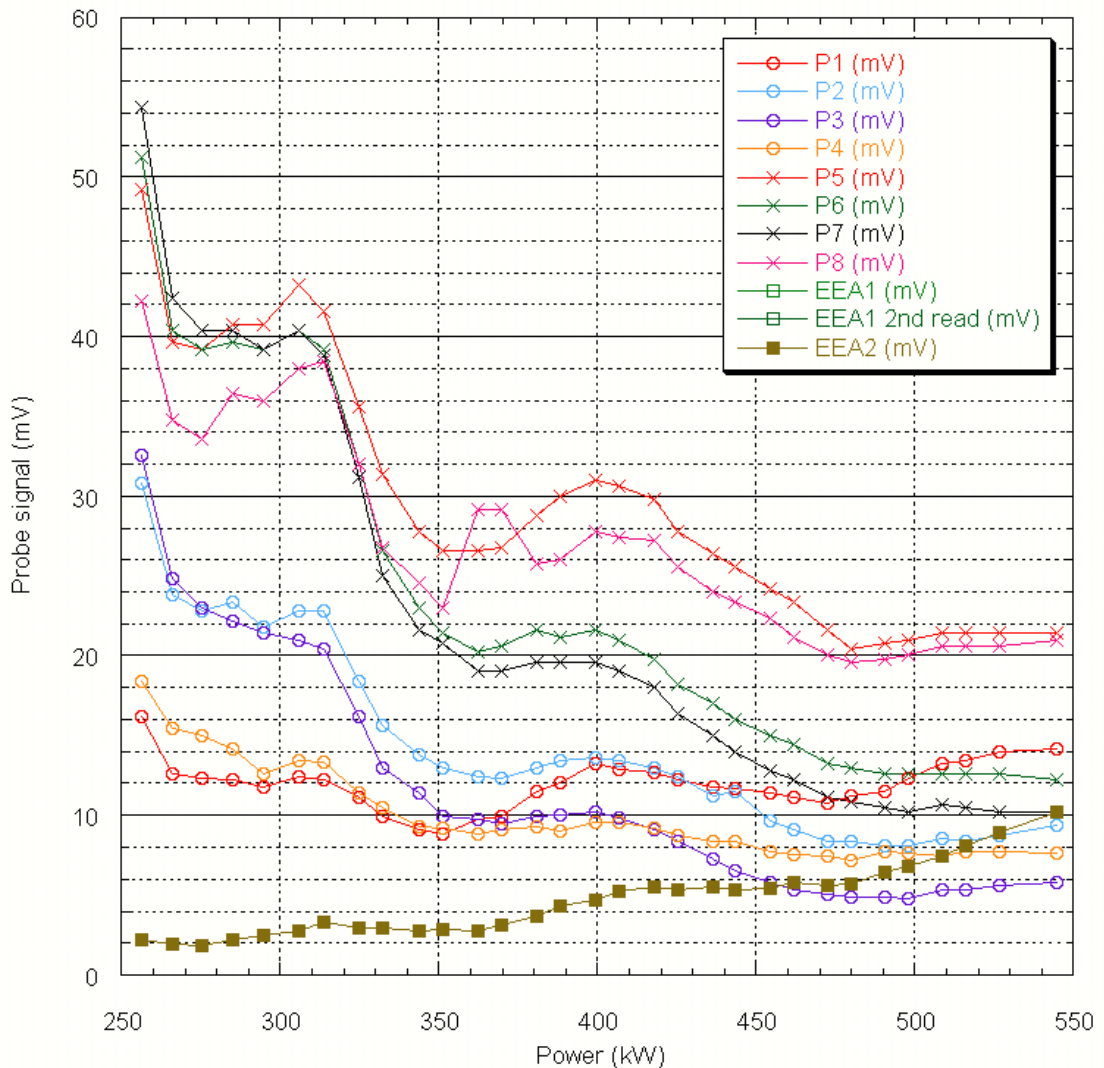


Figure 98: Zoom onto the lower part of Figure 97.

Figure 98 shows that the difference between the current from measured opposite coated (P3) and uncoated (P2) sections of the sample plate. The difference is most marked at high power levels. The currents only differ by a factor of 1.6 at most; the best explanation would once again be the small size of the coated area, which means that much of the current picked up by the probes may have come from uncoated areas. Another major problem was contamination of the NEG surface by gas desorbed by the rest of the waveguide. The residual vacuum level in the waveguide (from  $5 \cdot 10^{-5}$  Torr to  $10^{-4}$  Torr) was such that the coating would soon have been covered by gas as well, rendering it ineffective as a pump. In the real CESR waveguide or any other accelerator waveguide

section, should such a coating be applied, the entire surface would be covered, and the vacuum system would be more effective.

A comparison of the performance of the coated sample plate insert with a plain stainless steel insert in otherwise identical conditions is given in Figure 99. The difference between P2 and P3 on the stainless insert at low power levels is likely to be due to the different processing and baking time that the sample plate holder (used to secure all of the coated inserts into place, and therefore baked repeatedly) and the stainless steel insert (used only for this experiment). This would explain why the signal from P3 is greater than that from P2 in that instance. At the higher power levels, the difference is less marked because of the improved conditioning of the stainless steel insert (as with all 'return' scans through the power range, the measurement was taken from low to high power levels). The signal from P3 on the NEG coated insert is seen to be lower than that of P2 at the higher power ranges. The increased difference at the higher energy ranges could perhaps be explained by the fact that according to Figure 8 and Figure 36, both stainless steel and TiZrV have peak yield at primary electron energies around 300eV. The difference between the maximum secondary electron yields of stainless steel and that of the NEG coated plate would therefore be at its highest around those primary electron energies.

What these tests show is that even in less than optimal conditions, the coating has a beneficial effect on multipactor intensity. Unfortunately, they do not show multipactor suppression with only a small NEG-coated surface. It is possible that a more complete coverage would allow complete suppression. A more complete coverage could also only be beneficial as far as vacuum levels are concerned, if the waveguide is operated in the UHV vacuum range.

The signal from the probe opposite the TiN-coated stainless steel sample plate insert plate (P2 in this instance) showed little difference to the similar probe P3 that was opposite the stainless steel body of the sample plate. At low power levels (~200kW), it does appear that the signal from P2 is lower by up to a factor of 2 than the signal from P3, but as the power was raised, that difference vanished. Beyond 400kW, it can be said that P2 and P3 picked up identical signals. No clear explanation for that can be provided.

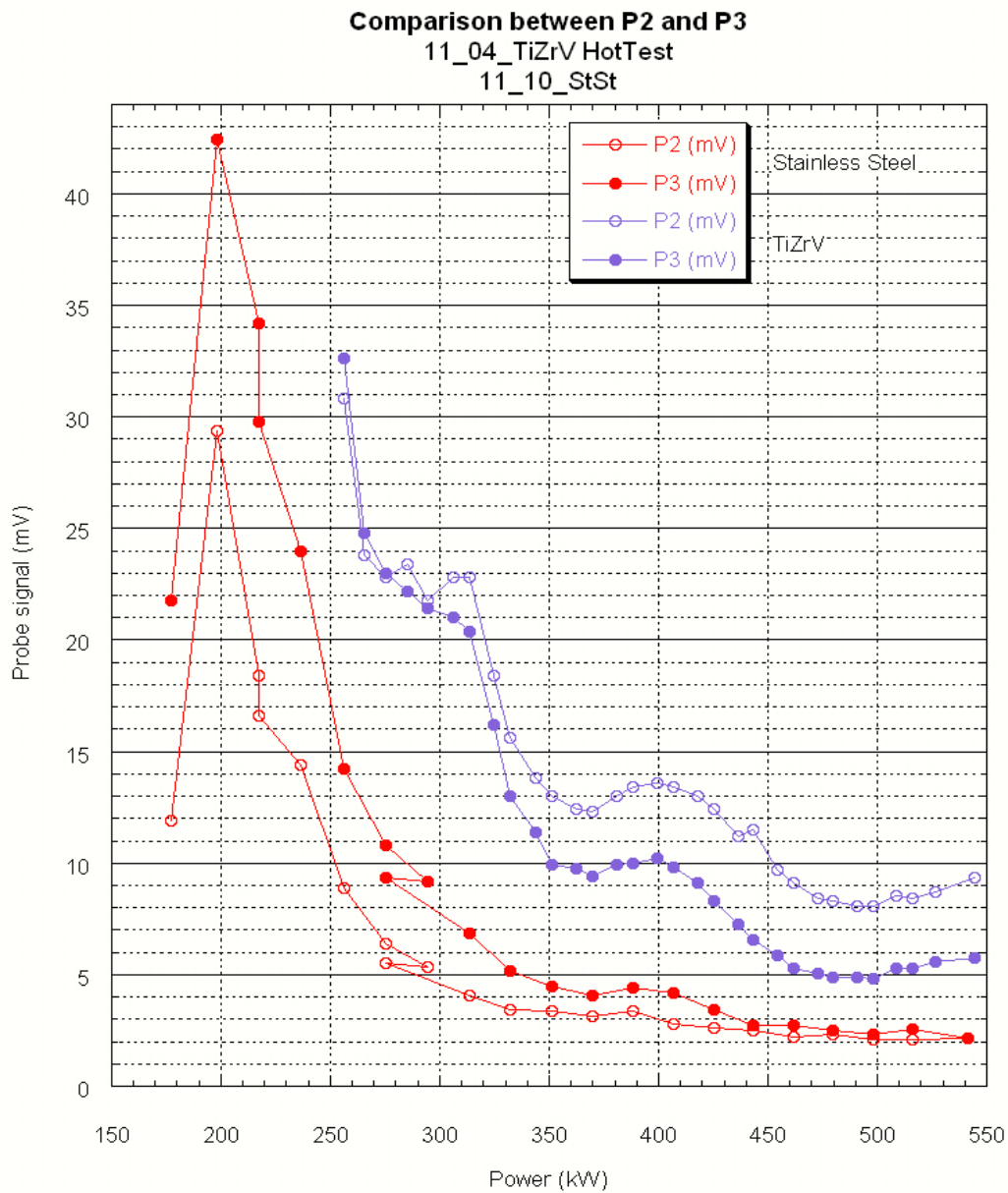


Figure 99: Comparison of the effect of a TiZrV sample plate compared to a plain Stainless Steel plate on P2 and P3 (the TiZrV plate is opposite P3).

The reasons for the lack of effectiveness of the TiN may be numerous. One probable reason was that the surface covered by TiN was very small (one 15cm diameter sample plate insert) in a large waveguide, therefore contamination from the rest of the waveguide could soon cover the sample plate with various gases and other contaminants, reducing its efficiency.

**Titanium Nitride Results**  
(Before and after activation 6h/250C)  
11\_11\_TiN

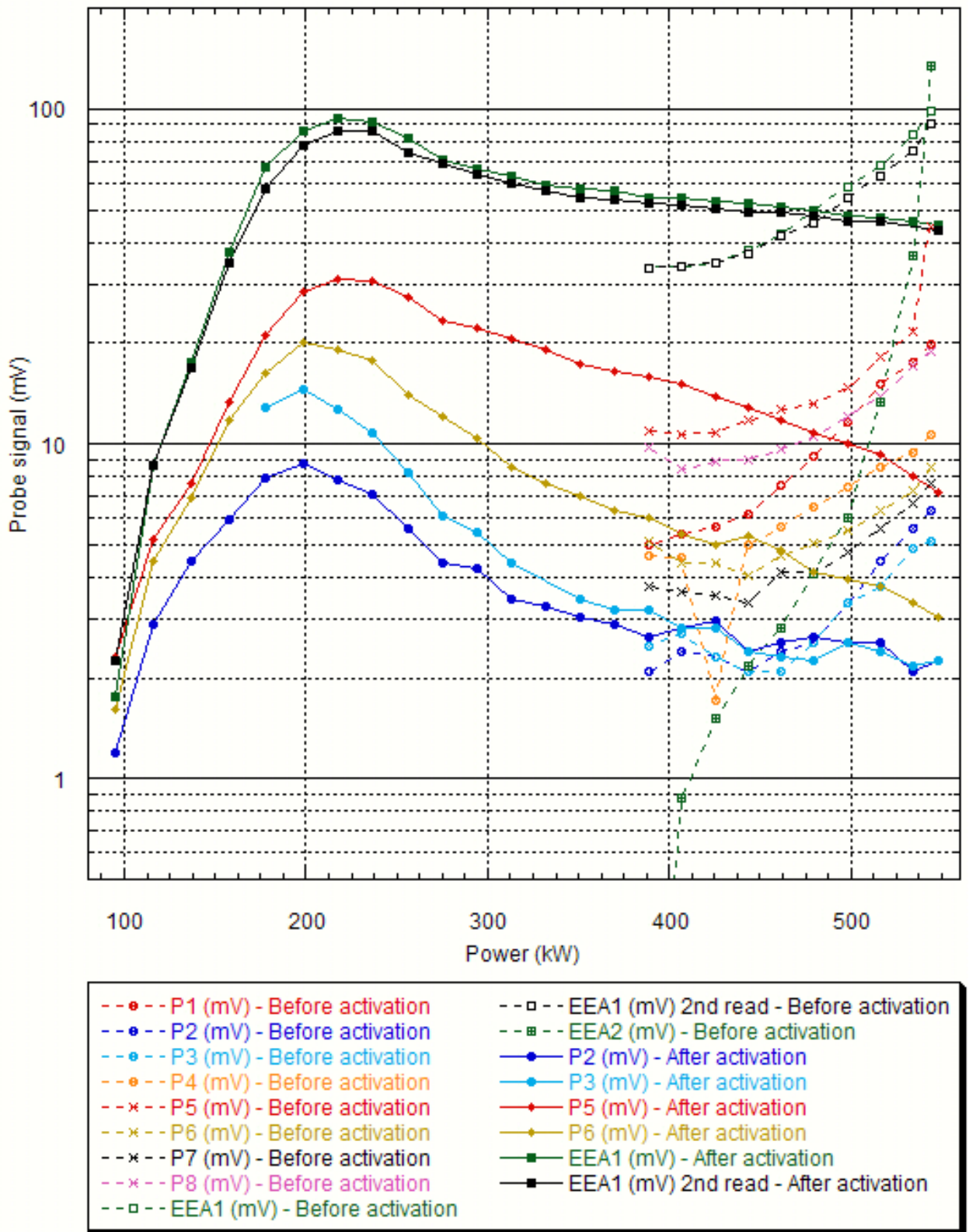


Figure 100: TiN results showing effect of activation (in this case, the insert was opposite P2)

It is also interesting to note (on Figure 100) that even before activation, the P2 signal begins to creep below the signal from P3 (going down from higher power levels). It was unfortunate that we could not go any lower in power with the TiN sample plate before activation since multipactor spontaneously extinguished. The reasons for that may include the fact that this was one of the last experiments carried out and the waveguide was quite well processed by that point, and despite frequent exposure to air, the secondary electron yield of the waveguide body was certainly going down as the measured current intensities and frequent extinctions of multipactor showed.

Another coating that was tested by RL. Geng using WG3 was anodised niobium in a solution of ammonium hydroxide (15%). The sample plate was made of niobium, as was the cathode. The composition of the layer is mainly  $\text{Nb}_2\text{O}_5$ . The tests tended to indicate that different layer thicknesses and deposition voltages affected the onset level of multipactor. The multipacting current in the waveguide also reached levels approximately half those that would be expected in an uncoated waveguide.

## 6.2.2 Conditioning

As was already mentioned in section 5.2.4, surface conditioning also reduces the secondary electron yield of the surface. It is therefore an important tool in the challenge to suppress multipactor.

A test was carried out with  $\text{LN}_2$  running through the cooling channel to cool the waveguide. This was an attempt to approach the real operating temperatures of the CESR input coupler (varying from room temperature near the window to 2K in the niobium coupler region). It is known at those temperatures that many gas molecules would condense onto the waveguide surface, as was measured at CESR in [8]. This gas deposition tends to increase the secondary electron yield of the surface.

The lowest temperature that could be reached was 147K (see Figure 101), allowing the condensation of water (at pressures of  $10^{-6}$ Torr), but few other gases. This was enough however to make any measurement of the multipactor current impossible due to constant RF trips. This verified what was already expected, that condensed gases on the surface are very detrimental to the performance of the waveguide. This agrees quite well with the observations made in Section 5.2.4 regarding the conditioning of surfaces. Our vacuum quality in the experiment was in this case insufficient to allow us to process the gas off

the surfaces faster than it could condense back onto them, preventing us from reaching any stable multipacting conditions.

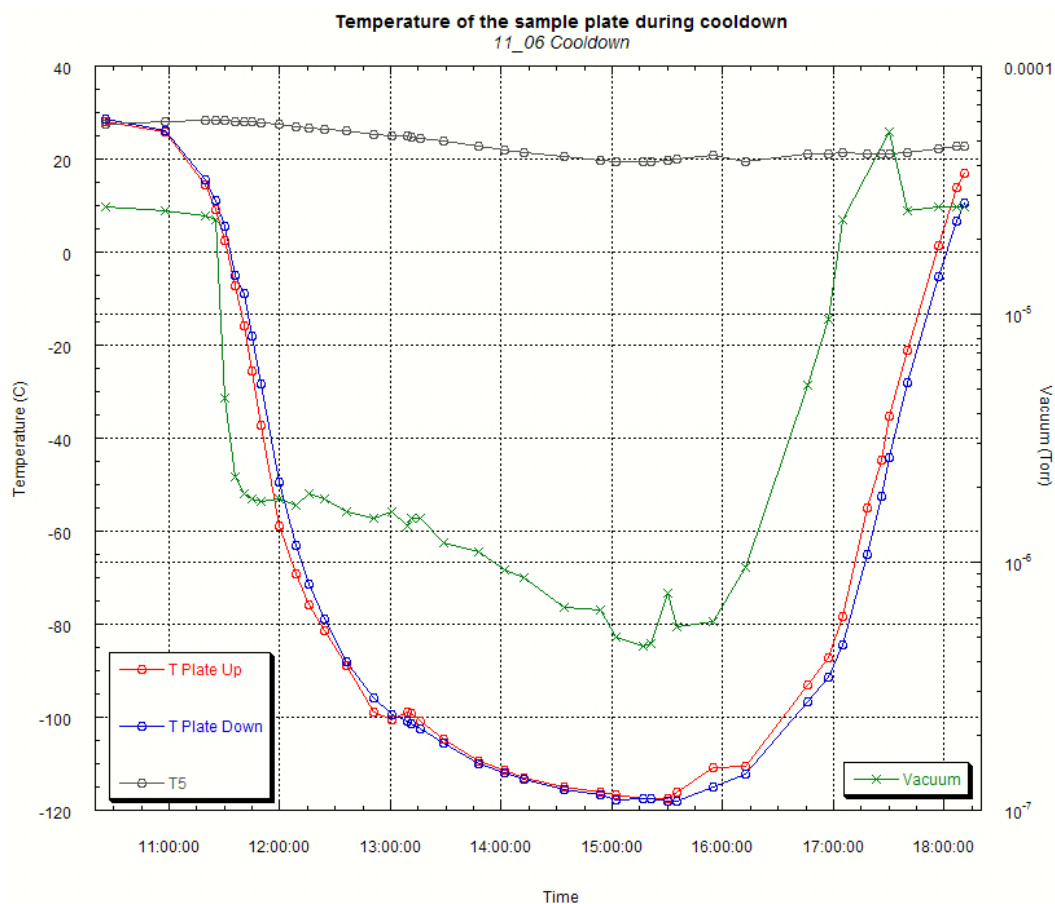


Figure 101: Temperature of the sample plate during cool-down ( $T_{Plate\ Up}$  and  $T_{Plate\ Down}$  were situated on an upstream and downstream corner of the sample plate respectively).  $T_5$  was situated on the outer surface of the waveguide near the large flange box.

Every laboratory has methods of conditioning RF systems, but it might be worth noting that extra conditioning can be achieved by artificially enhancing multipactor in the waveguide using static magnetic fields. If the field in the waveguide is set to the critical field  $B_z^*$  (described in section 6.1.1.2), the multipactor current is considerably enhanced and can be used to quickly process the surfaces of the waveguide. By sweeping the waveguide walls with the multipactor current, areas that do not see high energy electron impacts in normal conditions may also be cleaned. This can be added to the local electric field enhancement that can be obtained by using standing waves. This can be achieved by using a sliding short to sweep the surfaces with the antinodes of the standing wave.

## 7 Multipactor in other components

### 7.1 Waveguide E-plane bend

The CESR-type cavities have three E-plane bends. Two of these are in the LN<sub>2</sub>-cooled coupler waveguide and the other is in the niobium input coupler section of the cavity itself. Geometrically, they are all similar, being 17" by 4" in section and having a radius (in the centre of the waveguide) of 14.8cm.

Simulations have been carried out using MAGIC on waveguide bends to examine their effect on multipactor. Given the good correlation between the simulated and actual behaviour of the straight sections of the waveguide, it is reasonable to assume that other geometries can be studied with a reasonable degree of confidence. The waveguide bend was modelled using a cylindrical system of coordinates, the model was very similar to the coaxial waveguide geometry detailed in section 3.5.2. The waveguide ports were however moved to the ends of the waveguide, and the width was set to 17" as in the CESR system.

While the simulations show multipactor can occur in the waveguide, electron dispersion towards the edges of the waveguide was observed to occur much more quickly (visible in the videos in the CD-ROM annex). Because of this, multipactor only remains in the centre-plane of the waveguide (more so than the standard rectangular waveguide). This hints at the possibility of using a groove or ridge in the waveguide bends to reduce or suppress multipactor in such a system. Simulations carried out with a ridge on the inner waveguide wall have led to a disappearance of multipactor after about 100ns of simulation time with 150kW (Figure 102) as well as 350kW of forward RF power.

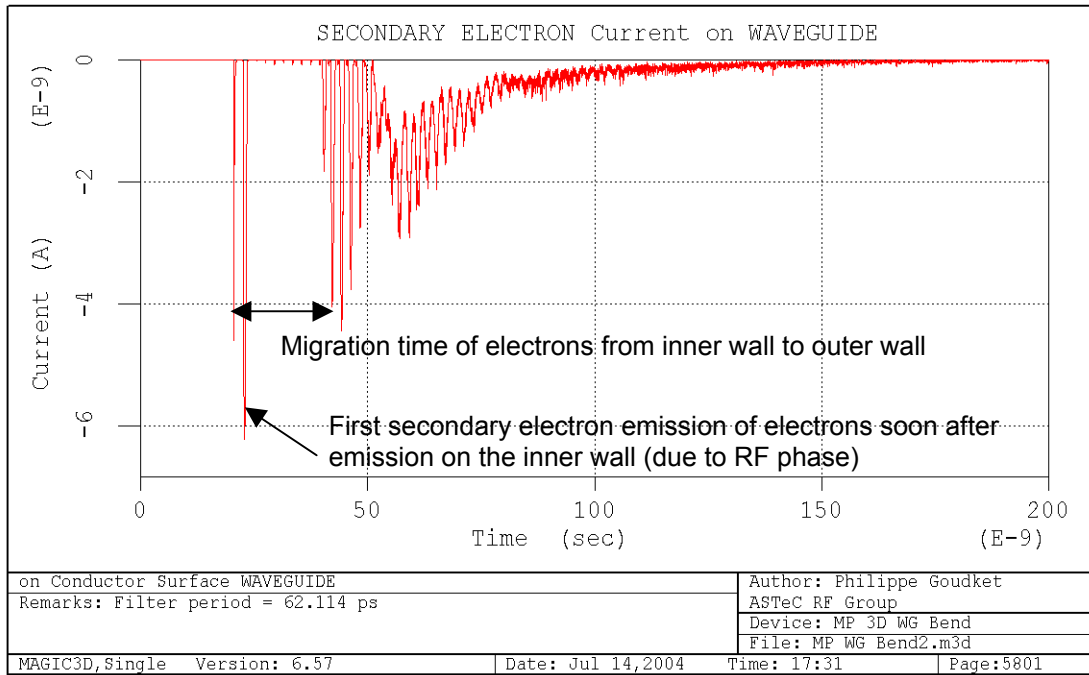


Figure 102: Simulation of the secondary electron current picked up on all waveguide surfaces in a waveguide bend with a 5mm wide x 4mm high ridge, with 150kW forward power, showing the disappearance of the electron current soon after the first electrons are emitted.

The simulation from which Figure 103 came showed that the dominant multipactor mode is asymmetric. When coming from the inner wall, the electrons cross the waveguide in 3.5 periods, making it 4<sup>th</sup> order multipactor. The return crossing takes 7.5 periods, making it 8<sup>th</sup> order multipactor. This can be explained by the difference in strength of the electric field at the inner and outer surfaces that affects the maximum momentum that can be gained by newly emitted electrons.

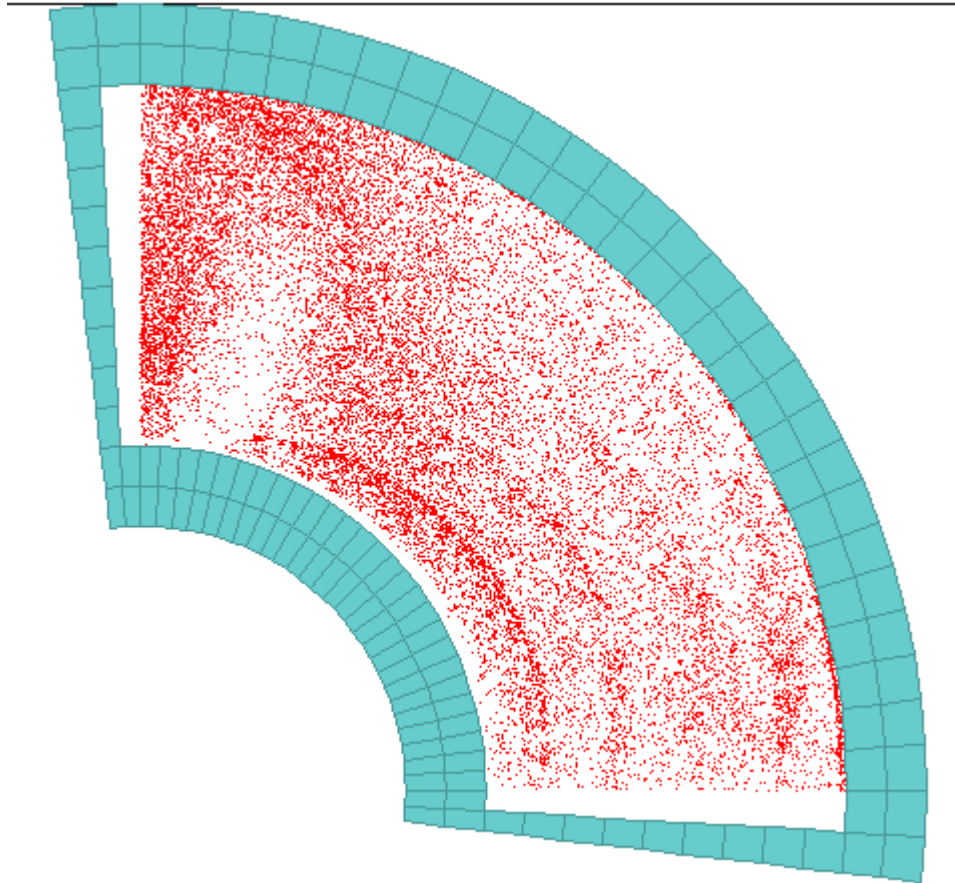


Figure 103: Waveguide bend simulation after 79.5ns at 150kW power.

## 7.2 Other components

### 7.2.1 Input coupler

The waveguide is coupled to the cavity by a tongue coupler and niobium waveguide bend. Since the waveguide is at its coldest in that area, it is the most likely location for adsorbed gas concentration. However, tests and operational experience with the solenoid coils wrapped around the heat exchanger and double E-bend sections of CESR waveguides in operation at Cornell have shown that the coil wrapped around the double E-bend alone sufficed to greatly reduce the occurrence of breakdown in the input coupler. This would tend to show that most multipactor events occur away from the niobium sections of the coupler.

The size of the MAGIC simulation required to realistically model multipactor in the tongue coupler (including the cavity beam tube behind) would be prohibitive and no MAGIC simulation was possible. Operational experience indicating no particular tendency for this

area of the waveguide coupler to show any multipactor, the benefits of further investigation would be of limited interest.

### **7.2.2 RF Window**

The RF window and pumping section beyond are also potential sources of multipactor. The window itself is, as is the coupler, monitored by a trip detector. As for the tongue coupler, no trips were detected near the window during cavity operation. The pumping section, however, is a waveguide with several step transitions from 162mm on the window side to 4" (=101.6mm) on the E-bend side. The same simulations as the general waveguide coupler can be conducted using MAGIC using the general geometry of the section (details such as the pumping ports themselves would however be very difficult to model using MAGIC).

As the vacuum pressure should be lower in the pumping section than other sections of the waveguide, and the waveguide height increases before opening to the full 9" height at the window, multipactor is less likely to occur in that section than the 4" high double E-bend and heat exchanger sections studied in the previous chapters.

## **7.3 Conclusion**

Both operational experience and the simulations (where they were possible) point to the straight sections of the input coupler as the main sources of multipactor breakdown. The addition of a ridge to the input coupler bends does not appear to have any drawback and the simulations indicate that it would help improve multipactor suppression. As far as the other warm sections of the coupler are concerned, the use of a magnetic field should suffice to suppress any multipactor should it prove to be a problem. It is not thought advisable to modify the geometry of the input coupler itself, and the use of magnetic bias in that region requires consideration of the risk of trapping magnetic flux in the event of a quench of the superconducting cavity.

## **8 Conclusion**

### ***8.1 Multipactor simulations***

Many models of multipactor have been devised over the years. As more realistic conditions are included in the model, it generally becomes necessary to resort to 3D numerical models such as the PIC code MAGIC.

The MAGIC code was found to be able to model the initial stages of a multipactor discharge realistically in simple 3D geometries. The mesh density the code requires to achieve realistic results may be a hindrance for more complex PIC simulations where the simulation time might become prohibitive, but it was otherwise found to be a good aid in understanding multipactor evolution. Its trustworthiness was found to be satisfactory after comparison of the results with a comprehensive multipactor study carried out on coaxial waveguides.

A factor in achieving realistic simulations was the inclusion, in the secondary electron yield model, of low energy backscattered electrons. This component of the effective electron yield has recently been quantified by teams at CERN and at SLAC [19, 20] and the persistent presence of low energy electrons is also deemed to be a determining factor in electron cloud situations.

The code proved useful in predicting and matching the experimental results, such as the presence of the low energy cloud of electrons near the sidewalls, the lack of distinct multipactor bands and the effectiveness of grooves and ridges in achieving multipactor suppression.

### ***8.2 Multipactor suppression methods***

Several multipactor suppressing methods were examined during the course of this work.

The application of a static longitudinal magnetic bias to the waveguide bends the electron trajectories away from the opposite wall of the waveguide, and with a rectangular waveguide of given dimensions, a simple formula can predict a field strength that will be sufficient to ensure that multipactor will not build up across the waveguide. In the case of the CESR cavities, a 10G bias is sufficient to prevent multipactor from forming in the

straight sections of the input coupler. A major advantage of this method is that its effectiveness does not depend on the cleanliness of the waveguide surfaces.

Single grooves have been examined here with the objective of trapping primary electrons in a low field area at the centreline of the waveguide. They were experimentally found to be effective at reducing the multipactor saturation current and to slow down the build-up time, but insufficient to stop all multipacting in the waveguide as the multipactor develops across a broad region.

Multiple grooves have not led to improved multipactor suppression as the tangential electric field that develops across the off-axis grooves modifies the multipacting trajectories and degrades the performance of the coupler. Nonetheless, it may be possible to avoid creating excessive tangential fields through the use of shorter and/or carefully placed grooves on the waveguide surface. A numerical study of the effectiveness of grooves as a way of reducing the secondary electron yield of surfaces was also recently carried out by G. Stupakov and M. Pivi [49]. One of their early conclusions was that the depth of the grooves was the most important factor determining their effectiveness.

Placing a ridge along the waveguide centreline is another attractive option that gives similar performances to a single groove. Its main advantage compared to the groove is that it generally is much easier to install in a rectangular waveguide. A ridge was also verified to successfully prevent multipactor build-up in areas of the waveguide such as the bends.

Several surface coatings were examined in order to evaluate their effectiveness at suppressing multipactor. Titanium nitride is widely used in accelerators to lower the electron yield of surfaces. A titanium-zirconium-vanadium getter is a more recent development that has been developed at CERN as a passive vacuum pump. Its low secondary electron yield, when activated, make it an attractive possible substitute for TiN in input couplers. While the experimental vacuum conditions were insufficient to fully validate these coatings as multipactor suppressing methods in a rectangular waveguide coupler, the experimental trends show that they have a positive effect.

### **8.3 Further experiments and developments**

The experiments carried out during the course of this work allowed the observation of multipactor behaviour as well as the evaluation of the effectiveness of several multipactor suppression methods. The experiments were successful in:

- Observing multipactor-induced discharge and measuring electron currents and electron energies at various power levels, wave propagation modes and locations in the waveguide.
- Verifying the effectiveness of a static longitudinal magnetic field bias for multipactor suppression.
- Evaluating the effectiveness of slots and ridges on the waveguide wall for multipactor suppression.
- Partially validating the use of coatings on the waveguide wall to lower the secondary electron yield of the surface.

The experiments, and WG3 in particular, could still be improved, most notably with regard to surface coatings. The waveguide was designed with a large sample plate to be able to test surface conditions across the width of the waveguide and over a significant length, but in the experiments carried out the coated areas were limited by the size of the sample on which a coating could be applied. To completely validate the use of coatings in the CESR input coupler as a means of multipactor suppression, a test with a more complete coverage should be carried out. The test would also be more reliable if the vacuum quality was improved, perhaps through the use of ceramic vacuum windows rather than the Mylar windows used in the WG1-3 experiments.

Further studies could be carried out to understand the effects of electron stimulated desorption and the interaction between multipacting electrons and the resulting gaseous breakdown. The saturation mechanism that limits multipactor in a fully processed waveguide is also not fully understood and it might be interesting to investigate it further. MAGIC simulations may be of some use due to the possibility of including ionisation of neutral gas into the modelling. Early trials however showed that the time required to run a representative simulation might, however, be excessive.

Numerical simulations of the effect of an applied magnetic bias were also carried out in coaxial waveguides, and it was shown that it could also be an effective method to

achieve multipactor suppression. This could be helpful in cases where it is impractical to design a coupler with the static voltage bias necessary to prevent multipactor build-up.

As far as the CESR-type input coupler waveguides are concerned, the best solution to achieve multipactor-free operation suggested by this work is the use of a static longitudinal magnetic bias, first suggested by R.L. Geng. While passive methods such as grooves, ridges or surface coatings were shown to have a positive influence, they did not achieve complete multipactor suppression either experimentally or when using the MAGIC simulations. The use of coatings would additionally be hindered by the likely cryosorption of gas due to the coupler being an interface between a warm and a cold region of the accelerator. The main drawback of using a static magnetic field is the possibility of trapping magnetic flux in the superconducting cavity in the event of a quench. This may make it preferable to use a groove or ridge in the niobium bend section of the coupler to reduce that particular risk.

## **Appendix**

## A - Supporting CD-ROM

A CD-ROM is attached to this thesis and contains a number of MAGIC videos, films of the multipactor breakdown taken during the WG1 experiment and all of the measured experimental data for WG3.

*Magic simulation videos:*

- **Video of multipactor in waveguide bend showing electron drift to sidewall**

Views of multipactor in a waveguide bend of the same dimensions as the CESR bends at different power levels projecting onto the X1X2 (longitudinal) and X2X3 (side view) planes.

- WGBend\_150kW\_longitudinal.avi
- WGBend\_150kW\_sideview.avi
- WGBend\_200kW\_sideview.avi
- WGBend\_300kW\_longitudinal.avi
- WGBend\_300kW\_sideview.avi

- **Video of multipactor in a rectangular waveguide**

Views in the X1X2 and X2X3 planes of multipactor in a rectangular waveguide with 200kW forward RF power.

- RectWG\_200kW\_Longitudinal\_Side\_Views.avi

Multipactor in a rectangular waveguide with a 3G magnetic bias along the X3 axis

- RectWG\_3G\_200kW.avi

Video of multipactor in SW mode in a rectangular waveguide (210kW RF power)

- RectWG\_210kW\_SW.avi

Video in the X1X2 plane showing multipactor with a bar, 1 slot and 5 slots along the waveguide centreline (250kW RF power)

- WGBar\_250kW.avi
- WGGrooves\_1Groove\_250kW.avi
- WGGrooves\_5Slots\_250kW.avi

- **Videos of multipactor in a coaxial waveguide**

Simulation of multipactor in a 50 $\Omega$  coaxial waveguide at 1.3MW and 2.5MW RF power levels, showing 2<sup>nd</sup> order and 1<sup>st</sup> order multipacting.

- Coax1300kW.avi
- Coax2500kW.avi

Some of the contents of the CD-ROM are available for download at:

[http://www.astec.ac.uk/rf/rf\\_preprints.htm](http://www.astec.ac.uk/rf/rf_preprints.htm)

## B – Analytical description of multipactor (by V. Shemelin)

The analytical description of multipactor is quite simple in the first approach. It starts with the equation of motion applied to the Lorentz force, which is all that affects the electron in the vacuum waveguide.

$$\vec{F} = q(\vec{E} + \vec{v} \times \vec{B}) \quad (1)$$

The following formulations are inspired by those developed by V. Shemelin [32]. By integrating the equation of motion for an electron across the gap, we can write

$$\ddot{y} = \frac{eU}{md} \sin \omega t \quad (2)$$

where  $y$  is the coordinate measured normally to an electrode,  $e/m$  is the specific charge of the electron, considered to be positive for ease of writing,  $U$  is the voltage amplitude across the gap  $d$ ;  $\omega = 2\pi f$  where  $f$  is the RF frequency;  $t$  is the time. It is useful to rewrite this equation in a normalised form:

$$\lambda'' = \xi \sin \theta \quad (3)$$

where  $\lambda = y/d$ ,  $\xi = U/U_0$ ,  $U_0 = m\omega^2 d^2/e$ , and  $\theta = \omega t$ ; primes denote derivatives with respect to  $\theta$ , while dots denote derivatives with respect to  $t$ .

Integrating Eq.(2) we obtain

$$\lambda' = \xi(\cos \theta_1 - \cos \theta) + \beta_1 \quad (4)$$

$$\lambda = \xi(\theta - \theta_1) \cos \theta_1 + \xi(\sin \theta_1 - \sin \theta) + \beta_1(\theta - \theta_1) \quad (5)$$

Here,  $\theta_1$  is the phase at which the electron enters the gap, and  $\beta_1 = \bar{v}/\omega d$  is the dimensionless normal component of the initial velocity of the secondary electron.

A stable phase motion of the discharge particles is possible in the definite interval of initial phases, i.e. of phases when electrons enter the gap. These phases are calculated in an earlier publication by V. Shemelin [33].

The condition for the electron to resonantly cross the gap is that the transit time be equal to an odd multiple of half-periods of the RF field; this ensures that newly generated secondary electrons see the same relative phases as their predecessors. Eq.(5) implies that

$$1 = \xi(\theta_2 - \theta_1) \cos \theta_1 + \xi(\sin \theta_1 - \sin \theta_2) + \beta_1(\theta_2 - \theta_1) \quad (6)$$

where  $\theta_2$  is the phase at which the electron reaches the second electrode at  $\lambda=1$ . Since  $\theta_2 - \theta_1 = (2n-1)\pi$ , meaning that the electron crosses the gap in an odd number of half periods. Eq.(6) gives

$$\xi = \frac{1 - (2n-1)\pi\beta_1}{(2n-1)\pi \cos \theta_1 + 2 \sin \theta_1} \quad (7)$$

The value of  $\beta_1$  in Eq.(7) is given by

$$\beta_1 = \frac{\bar{v}_\perp}{\omega d} = \frac{2}{3} \frac{\bar{v}}{\omega d} = \frac{2}{3} \sqrt{\frac{2\bar{U}_s}{U_0}} \quad (8)$$

Here, the bars denote average values.  $\bar{U}_s$  is the voltage (in volts) corresponding to the mean velocity of the secondary electrons.

The condition for stable electron motion in a multipactor discharge requires that the electron enter the gap at a definite phase. We can use Eq.(7) to calculate the normalized voltage  $\xi$  at which the discharge becomes unstable in terms of this phase.

The change in the phase at the exit from the gap is determined by the fluctuations in the initial velocity and by the change of phase for a secondary electron at the entrance of the gap.

$$d\theta_2 = ad\theta_1 + bd\beta_1 \quad (9)$$

Here the differentials represent physical derivations and are not strictly speaking infinitesimal.

We take  $a$  and  $b$  to be the derivatives

$$a = \left. \frac{\partial \theta_2}{\partial \theta_1} \right|_{\theta_2 - \theta_1 = (2n-1)\pi} = \frac{(2n-1)\pi \xi \sin \theta_1 + \beta_1}{2\xi \cos \theta_1 + \beta_1} \quad (10)$$

$$b = \left. \frac{\partial \theta_2}{\partial \beta_1} \right|_{\theta_2 - \theta_1 = (2n-1)\pi} = -\frac{(2n-1)\pi_1}{2\xi \cos \theta_1 + \beta_1} \quad (11)$$

which are calculated using Eq.(6).

After the gap has been crossed  $N$  times, the change in phase at the entrance is given by

$$d\theta_{N+1} = a^N d\theta_1 + b(a^{N-1}d\beta_1 + a^{N-2}d\beta_2 + \dots + d\beta_N) \quad (12)$$

Here the differentials  $d\beta_1, d\beta_2, \dots$  are independent and correspond to fluctuations in the initial velocities. We write  $d\beta_j = \alpha_j d\beta_0$  for  $j = 1, 2, \dots, N$ , and we choose  $\alpha_j$  and  $\beta_0$  such that  $|\alpha_j| < 1$ .

$$d\theta_{N+1} = a^N d\theta_1 + b(a^{N-1}\alpha_1 + a^{N-2}\alpha_2 + \dots + \alpha_N)d\beta_0 \quad (13)$$

In order for the factor in front of  $d\theta_N$  not to increase with  $N$ , the coefficients for multiplying  $d\theta_1$  and  $d\beta_0$  must not increase. The first requirement leads to

$$|a| = \left| \frac{(2n-1)\pi \sin \theta_1 + \beta_1 / \xi}{2 \cos \theta_1 + \beta_1 / \xi} \right| < 1 \quad (14)$$

In order for the factor in front of  $d\beta_0$  to remain small, the variance of the sum in parentheses must not increase with  $N$ , denoting the variance of  $\alpha_j$  by  $\sigma\alpha^2$ , we find that the variance of the sum is

$$\sigma_s^2 = \sigma_\alpha^2 (a^{2N-2} + a^{2N-4} + \dots + 1) \quad (15)$$

Since Eq.(14) bounds  $\sigma_s$ , the second term in Eq.(13) is also bounded when  $|a| < 1$ .

Since  $\xi$  in Eq.(7) increases as  $\theta_1$  decreases, for positive values of  $\theta_1$  in Eq.(14) we get the stability condition

$$\tan \theta_1 < \frac{2}{(2n-1)\pi} \quad (16)$$

for the lower bound. Substituting Eq.(16) and Eq.(8) into Eq.(7) and expressing  $\xi$  in terms of  $U$  and  $U_0$ , we get the lower boundary of the multipactor discharge zone.

$$U_l = \frac{U_0 - (2n-1)\pi \frac{2}{3} \sqrt{2\bar{U}_s U_0}}{\sqrt{(2n-1)^2 \pi^2 + 4}} \quad (17)$$

On the upper boundary of the existence zone,  $a = -1$ , Solving this equation [with  $a$  taken from Eq.(14)]

$$\theta_1 = -\arctan \frac{2}{(2n-1)\pi + \beta_1 (4 - (2n-1)^2 \pi^2)} \quad (18)$$

Likewise, substitution of Eq.(18) into Eq.(7) yields an upper boundary for the voltage.

$$U_u = (1 - (2n-1)\pi\beta_1) \frac{U_0 \sqrt{1 + \varphi^2}}{(2n-1)\pi - 2\varphi} \quad (19)$$

$$\text{where } \varphi = \frac{2}{(2n-1)\pi + \beta_1 (4 - (2n-1)^2 \pi^2)}$$

We have thus found bounds on the voltage for a multipactor discharge to be stable against fluctuations in the initial velocity.

Due to the initial velocity the electrons start out with, it is possible for even some electrons that start in a retarding field to get clear of the electrode they were emitted from. The condition for this is derived from Eq.(4)

$$0 = \xi(\cos\theta_1 - \cos\theta_{ST}) + \beta_1 \quad (20)$$

where  $\theta_{ST}$  is the phase at which the electron stops. We must have  $\lambda = 0$  when  $\theta = \theta_{ST}$ .

Eq.(5) yields

$$0 = \xi(\theta_{ST} - \theta_1)\cos\theta_1 + \xi(\sin\theta_1 - \sin\theta_{ST}) + \beta_1(\theta_{ST} - \theta_1) \quad (21)$$

Eq.(20) and Eq.(21) form a system from which  $\theta_{ST}$  can be eliminated to find the critical value  $(\beta_1/\xi)_{cr}$  such that for  $\beta_1/\xi < (\beta_1/\xi)_{cr}$  the electrons return to the electrode from which they were emitted.

For a fixed value of  $fd$  (frequency\*gap), the bounds imposed by the return of electrons with a negative initial phase can be found by solving Eq.(20), Eq.(21) and Eq.(7) simultaneously and by setting  $\beta_1/\xi < (\beta_1/\xi)_{cr}$ . The actual boundary of the multipactor zones depends on  $fd$ . At higher  $fd$ , the retarding potential around the boundary is high and the electrons are therefore more easily thrown back to the electrode. The boundary in this case is defined by the equation that can be derived using the process described above. At lower  $fd$  values, the boundary is defined by the stability condition given in Eq.(17).

The formulation given above is only valid for small variations of  $\beta_1$ , as if higher variations are considered, the initial energy of some electrons might not be enough to counteract the effects of the retarding potential, resulting in an overall reduction of the effective secondary emission coefficient.

In order for the discharge to grow, the energy of the incident electrons must be such that the secondary electron coefficient is greater than 1. For typical materials, the secondary electron coefficient is greater than 1 in a range of a few tens or hundred eV to a few keV. The maximum is typically a few hundred eV.

The energy bounds can be found from the equation

$$\beta_f = \sqrt{2U_f/U_0} \quad (22)$$

where  $\beta_f$  is the normalized electron velocity at the end of the trajectory ( $\lambda = 1$ );  $U_f$  is the energy with which the electron reaches the electrode. Eq.(4) gives

$$\beta_f = 2\xi \cos \theta_1 + \beta_1 \quad (23)$$

The bounds determined by the final energy of the electron can be found by solving Equations (7), (22), (23) simultaneously with  $U_f$  chosen as the limits at which the secondary electron coefficient stays above 1.

This description can be expanded to take into account other factors such as tangential velocities of electrons as in [32].

## C - MAGIC mesh requirements

A brief study of the effects of the mesh density was carried out on a simple rectangular waveguide test-case. For the following graphs, two MAGIC code results were recorded for various mesh densities. They were fitted using a hyperbolic function that shows good agreement with the data points. It is apparent that the solutions converge towards an asymptotic value as the mesh density is increased. Increasing it too far would in theory lead to numerical rounding errors, but the time taken for such simulations would be prohibitive in any case.

The following test cases were measured in a standard rectangular waveguide situation, using a waveguide length of one guided wavelength (i.e.  $\lambda_g=0.794\text{m}$  in a 4"x18" waveguide operated at 500MHz). The measured values were the secondary electron charge and the collected electron charge (as measured by the code), representing the charge of secondary electrons created and the charge of all collected electrons.

Looking at the figures, it becomes apparent that the most critical factor is the number of cells in the X2 (height of the waveguide) direction. X1 (waveguide width) and X3 (waveguide propagation direction) have a much lesser effect on the result.

X1 mesh cells	X2 mesh cells	X3 mesh cells	Sec. e- charge	Col. e- charge
24.000	6.0000	24.000	2.7100e-17	1.8400e-17
24.000	8.0000	24.000	2.0000e-17	1.4400e-17
24.000	9.0000	24.000	1.8200e-17	1.3600e-17
25.000	9.0000	25.000	1.8900e-17	1.3900e-17
36.000	9.0000	24.000	1.7100e-17	1.3000e-17
24.000	9.0000	36.000	1.8100e-17	1.3400e-17
24.000	12.000	24.000	1.5100e-17	1.1800e-17
24.000	15.000	24.000	1.3900e-17	1.1100e-17
24.000	18.000	24.000	1.2300e-17	1.0200e-17
24.000	24.000	24.000	1.1700e-17	9.8000e-18
24.000	36.000	24.000	1.0700e-17	9.1800e-18
36.000	36.000	36.000	1.1300e-17	9.3400e-18
36.000	12.000	36.000	1.4700e-17	1.1600e-17
48.000	16.000	48.000	1.3400e-17	1.0600e-17
30.000	9.0000	30.000	1.8060e-17	1.3340e-17
40.000	12.000	40.000	1.4950e-17	1.1700e-17

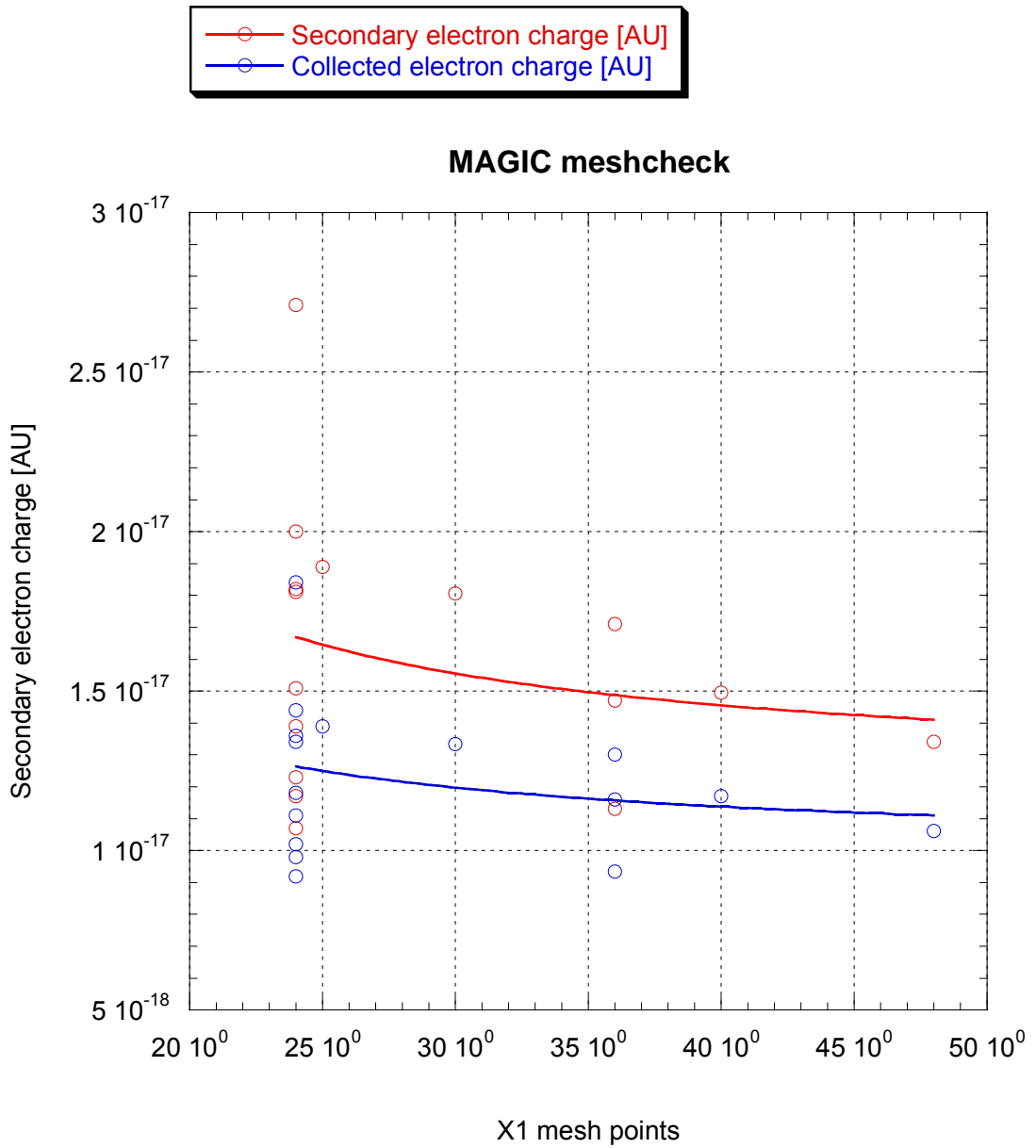


Figure 104: Evolution of the simulation result with respect to changes in X1

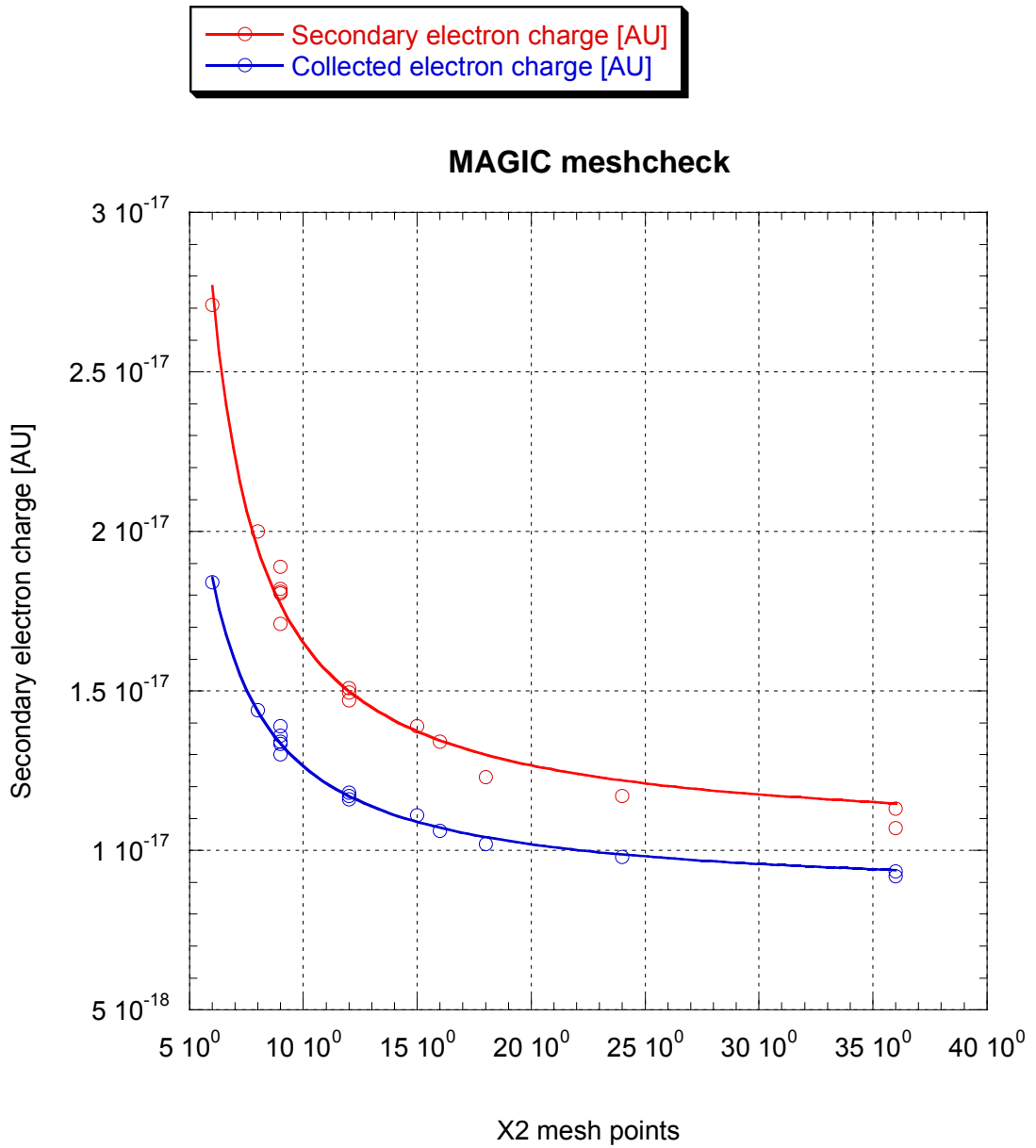


Figure 105: Evolution of the simulation result with respect to changes in X2

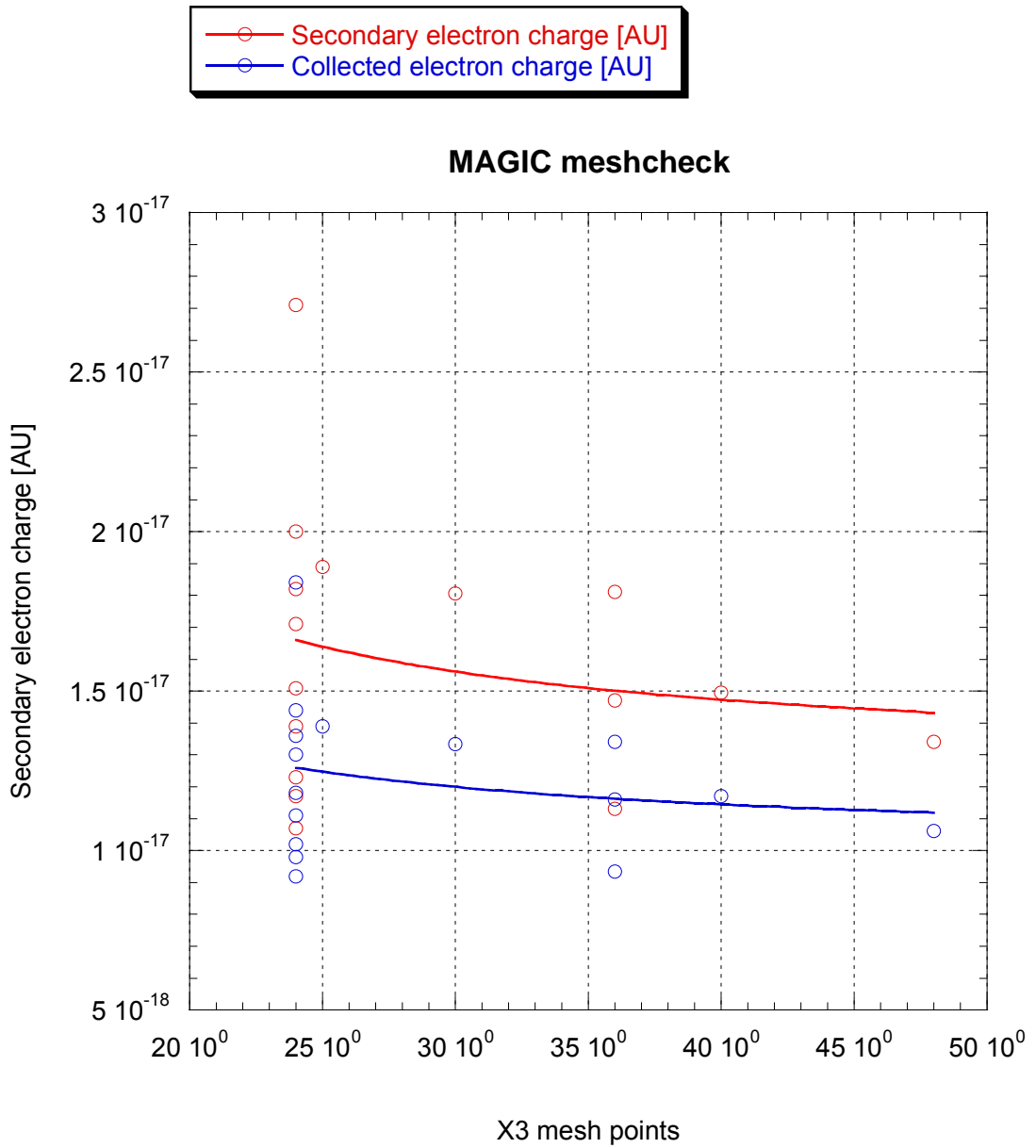


Figure 106: Evolution of the simulation result with respect to changes in X3

## Annex

### List of figures

Figure 1:View of a rectangular waveguide showing the electric field direction and strength of the TE <sub>10</sub> mode through a transverse cross-section.....	2
Figure 2: General layout of an RF cavity (from [1]).....	4
Figure 3: Comparison of typical re-entrant, normal conducting and elliptical, superconducting cavity layouts for high current applications (from [3]) .....	6
Figure 4: Schematic of the CESR cryomodule.....	7
Figure 5: Schematic energy spectrum for secondary electrons (from Schou[16]) .....	13
Figure 6: Measurement of the electron energy distribution curves from a scrubbed Cu surface at 10K at various primary electron energies (from [19]) .....	14
Figure 7: Contribution of true secondary and backscattered primary electrons to the electron yield of a scrubbed Cu surface (10K) (from [19]) .....	15
Figure 8: Secondary electron yield of typical metals in function of primary electron energy [25].....	15
Figure 9: Interaction regions for an electron beam impacting a solid. The penetration depths shown are for a 40keV beam. (1) Primary electron beam; (2) Auger electron region; (3) secondary electron region; (4) backscattered electron region; (5) characteristic X-ray region; (6) background X-ray region; (7) fluorescence X-ray region (from [1]).....	16
Figure 10: Azimuthal distribution of true secondary electrons (from [23]).....	17
Figure 11: Effect of the incident electron angle on secondary electron yield .....	18
Figure 12: Variation of the secondary emission yield with the incidence angle of a primary electron for typical metals (from [23]).....	18
Figure 13: Variation of the secondary electron yield of copper with the accumulated electron dose (from [25]).....	19
Figure 14: Illustration of simple types of multipactor in a simple two surface geometry...21	
Figure 15: Diagram from [11] showing areas corresponding to 1 <sup>st</sup> , 2 <sup>nd</sup> and 3 <sup>rd</sup> to 5 <sup>th</sup> order multipactor as a function of V over frequency and gap distance for a two-plate system.....	23
Figure 16: Multipacting bands expressed in terms of the phase range allowing electron return plotted against a function of the electric field (from [31]) .....	23
Figure 17: Typical secondary electron emission curves for various materials [25]. .....	25
Figure 18: Existence zones of multipactor in a CESR-type coupler (17"x4") allowing for normal components only of initial electron velocities (from [32]).....	28

Figure 19: Cross section of the simulated waveguide looking down the RF propagation axis.....	31
Figure 20: Schematic of a grooved waveguide as can be modelled in MAGIC .....	32
Figure 21: Yield curve used for MAGIC simulations with $E_{\text{peak}}=300\text{eV}$ , $\delta_{\text{peak}}=1.2$ , $\delta_{\text{low energy}}=1$ and $E_{\text{step}}=5\text{eV}$ .....	33
Figure 22: Photograph of breakdown in a slotted waveguide (left) and simulation of a slotted waveguide using MAGIC (right). The picture from the simulation shows the position of the macro-particles (electrons) 200ns after the start of the simulation. ...	36
Figure 23: Accumulated secondary electron charge on waveguide walls with $\delta_{\text{max}} = 1$ and varying values of $\delta_{\text{low energy}}$ (low energy band from 0 to 5eV).....	38
Figure 24: Results from MultiPac (from [39]) and markers showing simulations carried out in MAGIC. MultiPac simulation shows the relative counter function after 30 impacts. The simulated waveguide is a 1.3MHz, 50 $\Omega$ coaxial line of 40mm outer diameter...39	39
Figure 25: Status of the simulation with a power of 1.3MW 15ns after its beginning, showing both groups of electrons. ....	40
Figure 26: Multipacting waveguide.....	42
Figure 27: Experimental waveguide section (WG1).....	43
Figure 28: Grooved waveguide section (WG2).....	44
Figure 29: Vapour pressure of various gases. With WG3 temperatures and pressures, we can only expect to condensed gases as shown in the top left quadrant. ....	47
Figure 30: Basic waveguide characteristics .....	48
Figure 31: View of the initially planned sample plate mounted on the flange. No electron probes or EEAs remain in the real sample plate.....	50
Figure 32: View of the cooling channels on the cooling plate. Also visible are the holes (that were planned but not implemented) for the electron probes and EEA as well as the holes for the thermocouple wires. The second view shows the mounting of the cooling plate on the flange plate. ....	51
Figure 33: Detail of the sample plate fixation and RF contact with the waveguide walls .52	52
Figure 34: Picture of the waveguide being prepared in the workshop .....	52
Figure 35: Secondary electron yield of TiN coated surfaces [25].....	54
Figure 36: Secondary electron yield of a getter layer [25].....	55
Figure 37: Layout of the experimental set-up in the processing area at Cornell .....	56
Figure 38: View of the processing area.....	56
Figure 39: Heater coil connected to the waveguide blowing hot air through the cooling plate channel.....	57

Figure 40: Phil Barnes inspecting the heater wire clamped onto the sample plate support. .....	58
Figure 41: Electron probe schematic and engineering diagram (WG3) .....	59
Figure 42: Circuit diagram for the electron probes used with WG3.....	59
Figure 43: Electron probes and energy analyser (waveguides 1 and 2).....	60
Figure 44: Picture of the inside wall of WG3 showing 7 out of 8 probes as well as EEA1. .....	60
Figure 45: Picture and schematic of an electron energy analyser (the flange is a 2 <sup>3/4</sup> " flange) .....	61
Figure 46: Photomultiplier tube .....	62
Figure 47: Photodiode on WG3.....	62
Figure 48: Convectron gauge and pump-out ports on waveguides 1 and 2.....	63
Figure 49: Pumping system on waveguide 3 .....	64
Figure 50: Type T thermocouple on the waveguide wall.....	64
Figure 51: O-ring damage (detail) .....	67
Figure 52: Mylar window and flange showing the Technit mesh.....	68
Figure 53: Schematic of the Mylar window flange set-up.....	69
Figure 54: Discolouration in the upstream window after downstream window failure .....	69
Figure 55: Electron current (channel 2, top) and PMT signal (channel 1, bottom). Bottom graph shows greater time detail than the top graph.....	73
Figure 56: Electron current at different power levels (TW mode), before and after processing.....	74
Figure 57: Accumulated secondary electron charge from a 120ns long MAGIC simulation for two values of the maximum secondary electron yield.....	75
Figure 58: EEA current (top) and forward power (bottom) showing a 'tickle' on the power and its effect on the multipacting current. ....	76
Figure 59: Signal from probes P3 (top) and P4 (bottom) (on centreline of broad wall) as a function of time (WG1/2) .....	78
Figure 60: Intensity of multipactor current at different power levels (Cu plate, WG3)).....	79
Figure 61: Temperature map of waveguide interior taken from view-port.....	79
Figure 62: Electron current (top) and PMT signal (bottom) evolution with time (5s/div)...	80
Figure 63: Evolution of (post-processing) multipactor current during a measurement.....	82
Figure 64: Normalised integrated electron energy distribution at various power levels for WG 1 and 2. All plots normalised at 0V retarding potential.....	83
Figure 65: Differentiated energy spectra for a forward RF power of 118kW (blue), 297kW (green) and 437kW (red).....	84

Figure 66: Bias voltage for given fractions of the electron distribution at different power levels (from data in Figure 64) .....	85
Figure 67: Normalised integrated electron energy distribution at various power levels for EEA1 of WG3. The voltage given in the legend refers to the power as measured by the meter. The power calibration gives 2.5V=498kW, 2V=407kW and 1.4V=295kW. ....	86
Figure 68: Normalised integrated electron energy distribution at various power levels for EEA2 of WG3. The voltage given in the legend refers to the power as measured by the meter. The power calibration gives 2.5V=498kW, 2V=407kW and 1.4V=295kW. ....	87
Figure 69: Electron energy distribution for EEA1 (blue) and EEA2 (red) at 498kW with a copper plate (from EEA1_2.5V and EEA2_2.5V). The fit is the result of an interpolation and can be disregarded, particularly in the area around 20eV.....	88
Figure 70: MAGIC simulation of multipactor with only a 3.04cm strip on the centreline having a non-zero secondary electron yield, compared to a measurement from P2 (located on the centreline) on a plain copper waveguide.....	90
Figure 71: Trajectories of multipacting electrons after 105ns of simulation time (~5 impacts of the main multipactor mode) .....	91
Figure 72: MAGIC simulation measuring the accumulated charge at the location of P1-P8 after 100ns of simulation run-time.....	92
Figure 73: Measurement of P1-P8 from a plain copper plate.....	93
Figure 74: Effect of a solenoid field on the multipactor current measured at 250kW and 297kW by the EEA.....	96
Figure 75: Electron current measured on broad (P2) and sidewall (P1) with varying magnetic fields, showing a strong +/-4G spike as measured by the two different e <sup>-</sup> probes. ....	96
Figure 76: Effect of the bias field (as measured by the EEA at a retarding potential of 100V).....	98
Figure 77: Critical bias magnetic field for a CESR type coupler waveguide. In red solid circles are experimental points, the blue solid squares denote numerical calculation from Xing; the black lines show the theory for two waveguide gaps.....	100
Figure 78: MAGIC simulation at B <sub>z</sub> =3G and 250kW power. This frame is 23ns after the electron emission from the bottom wall.....	101
Figure 79: Multipactor current measurement (P2) measurement in SW mode at various bias field levels.....	102
Figure 80: Copper groove for WG2 (with the profile of the slot in the bar).....	103

Figure 81: Picture of a breakdown event in the grooved waveguide, also showing the waveguide interior from the same viewpoint (with a schematic representation of what is seen in the pictures). .....	104
Figure 82: Picture of a breakdown event with the aluminium bar insert.....	105
Figure 83: Copper sample plate with bar. ....	106
Figure 84: Picture of a discharge with a Cu bar (speckles are the result of noise in the camera).....	106
Figure 85: Layout of the probes on the waveguide .....	107
Figure 86: Measurement results with copper plate and bar (in mV across a 10kΩ resistor) .....	108
Figure 87: Comparison between measurements of the on-axis probe signal with and without the bar. This plot is plotted as a logarithmic plot to highlight the differences in signal picked up by the same probes in the two cases. ....	109
Figure 88: Comparison between measurements of P5-P8 and the sidewall EEA with and without the bar.....	110
Figure 89: Status of the MAGIC simulation after 120ns (a photograph of the experimentally observed situation can be seen in Figure 84).....	111
Figure 90: Close up of the single groove. Bridges were left across the groove so as to minimise the impact of the groove on RF and structural strength. The groove was cut through the sample plate, opening onto the cooling plate behind it.....	112
Figure 91: Copper plate with five slots, mounted on the flange .....	113
Figure 92: Copper plate with 13 slots.....	113
Figure 93: Summary of the grooved waveguide results. P2 and P3 are on the centre-line of the waveguide, P8 is near the sidewall.....	114
Figure 94: CST Microwave Studio simulation of a 13 groove waveguide with a gap under the sample plate, showing the E <sub>x</sub> component of the electric field .....	115
Figure 95: Warm-up temperatures of the sample plate (T <sub>su</sub> and T <sub>sd</sub> being the upstream and downstream thermocouples respectively on the corners of the sample plate) .....	116
Figure 96: TiZrV coated sample plate insert. The insert was made of three strips in order to fit into the deposition chamber. ....	117
Figure 97: Multipacting current measured with a TiZrV sample plate after heating to ~190°C for 2h40min.....	118
Figure 98: Zoom onto the lower part of Figure 97.....	119
Figure 99: Comparison of the effect of a TiZrV sample plate compared to a plain Stainless Steel plate on P2 and P3 (the TiZrV plate is opposite P3). ....	121
Figure 100: TiN results showing effect of activation (in this case, the insert was opposite P2).....	122

Figure 101: Temperature of the sample plate during cool-down ( $T_{\text{Plate Up}}$  and  $T_{\text{Plate Down}}$  were situated on an upstream and downstream corner of the sample plate respectively). T5 was situated on the outer surface of the waveguide near the large flange box.....124

Figure 102: Simulation of the secondary electron current picked up on all waveguide surfaces in a waveguide bend with a 5mm wide x 4mm high ridge, with 150kW forward power, showing the disappearance of the electron current soon after the first electrons are emitted.....126

Figure 103: Waveguide bend simulation after 79.5ns at 150kW power. ....127

Figure 104: Evolution of the simulation result with respect to changes in X1 .....142

Figure 105: Evolution of the simulation result with respect to changes in X2 .....143

Figure 106: Evolution of the simulation result with respect to changes in X3 .....144

- 
- <sup>1</sup> R.P. Walker, *Synchrotron Radiation*, CAS CERN 94-01, p437, 26 Jan. 1994
- <sup>2</sup> S. Belomestnykh, *The High Luminosity Performance of CESR with the New Generation Superconducting Cavity*, Proc. PAC 1999, p.272 (1999)
- <sup>3</sup> H. Padamsee, J. Knobloch, T. Hays, *RF Superconductivity for Accelerators*, Wiley Series in Beam Physics and Accelerator Technology, New York (1998)
- <sup>4</sup> M. Pisharody et al, *High Power Window Tests on a 500MHz Planar Waveguide Window for the CESR Upgrade*, Proceedings PAC 95
- <sup>5</sup> S. Belomestnykh, et al., *Running CESR at High Luminosity and Beam Current with Superconducting RF System*, Proceedings of EPAC2000, Vienna (2000)
- <sup>6</sup> E. Chojnacki, S. Belomestnykh; *RF Power Coupler Performance at CESR and Study of a Multipactor Inhibited Coupler*, Proceedings of 9<sup>th</sup> Workshop on RF Superconductivity, Santa Fe, 1999
- <sup>7</sup> Personal experience from a vertical test carried out on a CESR-type cavity with M. Pekeler (Accel) at Cornell University
- <sup>8</sup> R.L. Geng, H. Padamsee, *Condensation/Adsorption and Evacuation of Residual Gases in the SRF System for the CESR Luminosity Upgrade*, Proc. PAC 1999, New York (1999)
- <sup>9</sup> P. T. Farnsworth, *Television by Electron Image Scattering*, J. Franklin Institute, vol. **218**, pp. 411-444 (1934)
- <sup>10</sup> E. W. B. Gill and A. von Engel, *Starting Potentials of High Frequency Gas Discharges at Low Pressures*, Proc. Roy. Soc. (London) **A192**, 446 (1948)
- <sup>11</sup> A.J Hatch and H.B. Williams, *Multipacting Modes of a High Frequency Gaseous Breakdown*, Phys. Rev. vol. **112**, n.3, p. 681 (1958)
- <sup>12</sup> W.J. Gallagher, *The Multipactor Effect*, IEEE Trans. Nuclear Science, vol. **NS-26**, No. 3, June 1979
- <sup>13</sup> J. Rodney M. Vaughan, *Multipactor*, IEEE Trans. Electron Devices, vol. **35**, No. 7, July 1988
- <sup>14</sup> See conferences such as the 4<sup>th</sup> *International Workshop on Multipactor, Corona and Passive Intermodulation in Space Hardware*, ESTEC, Noordwijk, 2003, The Netherlands, <http://www.estec.esa.nl/conferences/03C26/>
- <sup>15</sup> F.L. Krawczyk, *Status of Multipacting Simulation Capabilities for SCRF Applications*, Proc. 10<sup>th</sup> *Workshop on RF Superconductivity*, Tsukuba, Japan (2001)
- <sup>16</sup> J. Schou, *Secondary Electron Emission from Solids by Electron and Proton Bombardment*, *Scanning Microscopy*, Vol.2, No. 2, pp. 607-632, Chicago (1988)
- <sup>17</sup> H. Seiler, *Secondary Electron Emission in the Scanning Electron Microscope*, J. Applied Physics 54 (11), Nov. 1983
- <sup>18</sup> R. Cimino, I. Collins, *A Surface Science Approach to the Study of Electron Cloud Phenomena*, Damping Ring Workshop 2003, Daresbury Laboratory, Jan. 2003
- <sup>19</sup> R. Cimino et al., *Can Low-Energy Electrons Affect High-Energy Physics Accelerators?*, Phys. Rev. Letters, Vol. **93**, No. 1, July 2004

- 
- <sup>20</sup> M. Furman, M. Pivi, *Probabilistic Model for the Simulation of Secondary Electron Emission*, Phys. Rev. S.T. vol. **5**, 124404 (2002)
- <sup>21</sup> J. Rodney M. Vaughan, *A New Formula for Secondary Electron Yield*, IEEE Trans. Electron Devices, Vol. 36, No. 9, Sept. 1989
- <sup>22</sup> J. Rodney M. Vaughan, *Secondary Electron Formulae*, IEEE Trans. Electron Devices, Vol. 40, No. 4, April 1993
- <sup>23</sup> J. Arianer, *Les Sources de Particules Chargées*, JUAS&CAS-CERN Lecture notes, 2000
- <sup>24</sup> Walter H. Kohl, *Handbook of Materials and Techniques for Vacuum Devices*, Springer-Verlag Berlin and Heidelberg GmbH & Co. KG, ISBN: 1563963876, (1995)
- <sup>25</sup> N. Hilleret et al, *The secondary electron yield of technical materials and its variation with surface treatments*, Proc. EPAC 2000, pp.217-221 (2000)
- <sup>26</sup> R.Kishek, Y.Y. Lau, *Multipactor Discharge on a Dielectric*, Proc. PAC 97, pp.3198-3201, Vancouver (1997)
- <sup>27</sup> L.K. Ang, Y.Y. Lau, R.A. Kishek, et. Al, *Power Deposited on a Dielectric by Multipactor*, IEEE Trans. Plasma Sc., **26**, 290 (1998)
- <sup>28</sup> R.B. Anderson, *Multipactor Experiment on a Dielectric Surface*, PhD Dissertation, University of Michigan (2001)
- <sup>29</sup> J. Lorkiewicz et al., *Anti-multipactor TiN coating of RF power coupler components for TESLA at DESY*, TESLA Design Report 2004-02
- <sup>30</sup> CRC Engineering Handbook, p.565
- <sup>31</sup> A. Dexter, R. Seviour, P. Goudket, *Elastic Scattering and Higher Order Multipactor*, Proc. 4<sup>th</sup> International Workshop on Multipactor, Corona and Passive Intermodulation in Space RF Hardware, ESTEC, September 2003
- <sup>32</sup> V.D. Shemelin, *Multipactor Discharge in a Rectangular Waveguide with Regard to Normal and Tangential Velocity Components of Secondary Electrons*, Cornell SRF note, SRF010322-03, <http://www.lns.cornell.edu/public/SRF/2001/>
- <sup>33</sup> V.D. Shemelin, *Existence Zones for Multipactor Discharges*, Sov. Phys. Tech. Phys. **31** (9), September 1986
- <sup>34</sup> R. Seviour, MRG/04/01 (Annual Report, Dept. Engineering, Lancaster University)
- <sup>35</sup> P. Ylä-Oijala, *Multipacting Analysis and Electromagnetic Field Computation by the Boundary Integral Equation Method in RF Cavities and Waveguides*, Ph.D. Dissertation at the Rolf Nevanlinna Institute, University of Helsinki, Finland, 1999
- <sup>36</sup> R.L. Geng, *Multipacting Simulations for Superconducting Cavities and RF Coupler Waveguides*, Proc. PAC 2003, Portland, Oregon (2003).
- <sup>37</sup> R.L. Geng, H.S. Padamsee; *Exploring Multipacting Characteristics of a Rectangular Waveguide*; pp 429-431, Proc. PAC 1999
- <sup>38</sup> B. Henrist, N. Hilleret, M. Jimenez, C. Scheuerlein, M. Taborelli, G. Vorlauffer, *Secondary Electron Emission Data for the Simulation of Electron Cloud*, Proc. Ecloud'02, CERN, April 2002

- 
- <sup>39</sup> P Ylä-Oijala, *Analysis of Electron Multipacting in Coaxial Lines*, TESLA Collaboration Report 97-21 (Nov. 1997)
- <sup>40</sup> R.A. Rosenberg, K.C. Harkay, *Nuclear Instruments and Methods in Physics Research A*, 453 pp.507-513 (2000)
- <sup>41</sup> R.L. Geng, P. Goudket, R.G. Carter, H. Padamsee, S. Belomestnykh, D.M. Dykes, *Dynamical Aspects of Multipacting Induced Discharge in a Rectangular Waveguide*, to be published (2004)
- <sup>42</sup> B. Henrist, N. Hilleret, C. Scheuerlein, M. Taborelli, G. Vorlauffer, *The Variation of the Secondary Electron Yield and of the Desorption Yield of Copper under Electron Bombardment: Origin and Impact on the Conditioning of the LHC*, EPAC'02, Paris, June 2002, pp. 2553-2555
- <sup>43</sup> G. Arduini, M. Jimenez, K. Weiss, *SPS Vacuum Observations and Electron Scrubbing with LHC Beam*, Proc. Chamonix XI, Chamonix, 2001
- <sup>44</sup> Y. Kijima et al., *The Secondary Electron Yield of the Material for the KEKB Superconducting Cavity Input Coupler*, Proc. SRF2001, Tsukuba (2001)
- <sup>45</sup> S.Y. Zhang et al. *Beam Scrubbing Strategy for Electron Cloud Suppression in the Spallation Neutron Source Ring*, Proc. PAC'03, Portland, Oregon (2003)
- <sup>46</sup> R. Losito, *LEP Couplers, a Troubled History of a Success*, Proc. High Power Coupler Workshop, Jefferson Lab, Newport News, VA, Oct. 30-Nov. 1 2002.
- <sup>47</sup> R.L. Geng, P. Goudket, R.G. Carter, H. Padamsee, S. Belomestnykh, D.M. Dykes, *Suppression of multipacting in a rectangular waveguides*, *Nuclear Instruments and Methods in Physics Research A*, 508 (2003) 227-238
- <sup>48</sup> Y. Li, S. Ho, *Vacuum Pumping Study of Titanium-Zirconium-Vanadium Thin Films*, ERL Reports – ERL03-8, [http://lns.cornell.edu/public/ERL/2003/ERL03-8/ERL\\_03\\_8.pdf](http://lns.cornell.edu/public/ERL/2003/ERL03-8/ERL_03_8.pdf) (2003)
- <sup>49</sup> G. Stupakov, M. Pivi, *Suppression of the Effective SEY for a Grooved Metal Surface*, Linear Collider Collaboration Tech Notes, LCC-0145 SLAC-TN-04-045, June 2004